Stony Brook University

OFFICIAL COPY

The official electronic file of this thesis or dissertation is maintained by the University Libraries on behalf of The Graduate School at Stony Brook University.

© All Rights Reserved by Author.

High-Precision Nucleon-Nucleon Interactions with Brown-Rho Scaling Medium Modifications

A Dissertation Presented

by

Jeremy William Holt

to

The Graduate School

in Partial Fulfillment of the Requirements

for the Degree of

Doctor of Philosophy

in

Physics

Stony Brook University

August 2008

Stony Brook University

The Graduate School

Jeremy William Holt

We, the dissertation committee for the above candidate for the Doctor of Philosophy degree, hereby recommend acceptance of this dissertation.

Gerald E. Brown – Dissertation Advisor
Distinguished Professor, Department of Physics and Astronomy

Thomas T. S. Kuo – Chairperson of Defense
Professor, Department of Physics and Astronomy

Clark McGrew
Associate Professor, Department of Physics and Astronomy

Larry Zamick
Professor, Department of Physics and Astronomy
Rutgers University

This dissertation is accepted by the Graduate School.

Lawrence Martin
Dean of the Graduate School

Abstract of the Dissertation

High-Precision Nucleon-Nucleon Interactions with Brown-Rho Scaling Medium Modifications

by

Jeremy William Holt

Doctor of Philosophy

in

Physics

Stony Brook University

2008

Today, the foundation for most theoretical calculations of nuclear properties across the periodic table is one of the several high-precision nonrelativistic nucleon-nucleon potential models based on meson exchange. Although these interactions fit with near perfection all experimental data available for two interacting nucleons, it is well known that such interactions alone are insufficient to describe very accurately the properties of many-nucleon systems close to nuclear matter density. In this thesis we suggest that density-dependent nuclear interactions based on the notion of Brown-Rho scaling can provide one avenue to extend the nuclear interaction to these density regions.

We first study symmetric nuclear matter based on both the Goldstone linked diagram expansion and Landau Fermi liquid theory. In the former we sum to all orders the particle-particle hole-hole ring diagrams to obtain the ground state energy as a function of

density. We find that the main effect of including Brown-Rho scaling is a reduction in both the saturation density and energy. In the Fermi liquid description of nuclear matter, we show that free-space nucleon-nucleon interactions are unable to describe the quasiparticle effective mass, compression modulus, symmetry energy, and anomalous orbital gyromagnetic ratio at nuclear matter density. By including the effects of Brown-Rho scaling, we show that these observables are in general better reproduced theoretically. Next, we explore the anomalously long lifetime of carbon-14, which has been a persistent puzzle to nuclear structure theorists for decades. We demonstrate that the dropping rho meson mass decreases the nuclear tensor force to such an extent that carbon-14 achieves its archaeologically long lifetime at a density of $\sim$ 85% that of saturated nuclear matter. We discuss future applications as well as the connection between medium-modified two-nucleon interactions and many-body forces.

Dedicated to my father, my brother, and the memory of my mother

Contents

List of Figures

List of Tables

Acknowledgements

I am deeply grateful to have worked under the guidance of Gerry Brown, my thesis advisor, during the course of this research. His keen intuition and insight inspired much of the work presented in this dissertation. Equally admirable is Gerry's constant good humor and supportive nature, which helped ease the transition into full-time research. Maybe most important, though, is that Gerry instilled a sense of joy and excitement in doing research, something that I hope remains with me for the rest of my scientific career.

I am fortunate to have had an unofficial "co-advisor", Tom Kuo, who helped build a rigorous foundation for many of the ideas presented in this dissertation and who was also the inspiration behind several others. It is easy to see why Gerry and Tom have collaborated for so long, as their stengths complement each other so well. It was a pleasure to have learned from them both.

I wish to thank a number of scientific collaborators who have helped in various aspects of this research. These include Jason Holt, Mannque Rho, Chang-Hwan Lee, Ruprecht Machleidt, Masa Harada, Chihiro Sasaki, and Nico Orce. I am also grateful to Achim Schwenk for fruitful discussions and critical comments on many parts of my research.

I owe many thanks to the staff of the Stony Brook physics department and nuclear theory group, particularly Pat Peiliker, Ellen Popenoe, and Diane Aveni, whose administrative expertise allowed me to spend time on physics rather than bureaucracy. Also, I am grateful to Edward Shuryak and the rest of the nuclear theory group faculty and graduate students who have created such a stimulating atmosphere in which to work and think.

Of course, my family has always been a constant source of support, especially my father and grandparents. I may not have even begun to study physics were it not for my older brother Jason. To have studied and worked in physics together already for so long has been a unique experience. Being the younger sibling has had its advantages, and I hope that in our future collaborations I can repay some of the debt I owe.

Finally, I am grateful to a number of close friends I met while at Stony Brook who helped distract me now and then from physics.

Chapter 1

Introduction

1.1 Realistic nuclear interactions

Ever since the modern theory of the nucleus was developed following the discovery of the neutron by Chadwick in 1932, perhaps the most important challenge in low-energy nuclear physics has been to understand the force responsible for binding together a nucleus and determining its properties. Today we know that nucleons are not fundamental particles nor is the nuclear interaction a fundamental force of nature. Rather, there is little doubt that all hadrons are composed of quarks and gluons interacting according to the Lagrangian for quantum chromodynamics (QCD)

$$\mathcal{L} = \bar{\psi}_i \left(i\gamma^\mu (D_\mu)_{ij} - m\delta_{ij} \right) \psi_j - \frac{1}{4} G^a_{\mu\nu} G^{\mu\nu}_a, \tag{1.1}$$

where ψ and G are the quark and gluon fields respectively, and D_μ is the covariant derivative defined by

$$D_\mu = \partial_\mu - igA^a_\mu t_a, \tag{1.2}$$

where t_a are eight SU(3) matrices. All precision tests of QCD come from high-energy scattering experiments, which probe a region in which the QCD coupling constant is small and which therefore is amenable to perturbation theory techniques. However, in the low-energy regime appropriate for the description of interacting baryons and mesons, QCD has a large coupling constant and can only be tested accurately by lattice gauge simulations [1, 2]. Presently, lattice gauge theory is unable to accurately describe the interaction between two nucleons in free space, though the preliminary efforts along these lines are encouraging [3]. Therefore, one has to rely on models to describe the

interaction between two nucleons, and one model that has proven to be highly successful since the earliest studies of the nuclear interaction is that of meson exchange, shown schematically in Fig. 1.1.

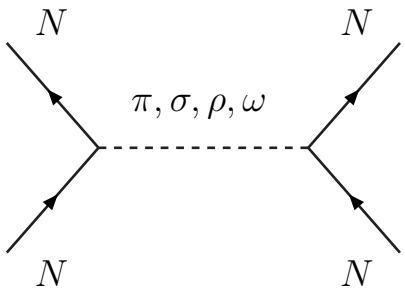

Figure 1.1: The nucleon-nucleon interaction arising from the exchange of various light mesons, such as the π, σ, ρ, and ω.

In the mid-1930's Yukawa predicted that the strong, short-ranged nuclear force resulted from the exchange of a massive scalar meson [4, 5], and since that time the description of the nucleon-nucleon (NN) interaction in terms of meson exchange has become increasingly complex as the number of mesons experimentally observed and needed to account for the fine details of the nuclear interaction has increased. Today, it is well-known that the nucleon-nucleon interaction arises mainly from the exchange of the pseudoscalar, isovector π meson; the scalar, isoscalar σ; the vector, isovector ρ; and the vector, isoscalar ω. These mesons couple to nucleon fields through the following Lagrangian densities

$$\mathcal{L}_{\pi^0 NN} = -g_{\pi^0}\bar{\psi}i\gamma^5\tau_3\psi\phi^{\pi^0}, \tag{1.3}$$

$$\mathcal{L}_{\pi^\pm NN} = -\sqrt{2}g_{\pi^\pm}\bar{\psi}i\gamma^5\tau_\pm\psi\phi^{\pi^\pm}, \tag{1.4}$$

$$\mathcal{L}_{\sigma NN} = -g_\sigma\bar{\psi}\psi\phi^\sigma, \tag{1.5}$$

$$\mathcal{L}_{\omega NN} = -g_\omega\bar{\psi}\gamma^\mu\psi\phi^\omega_\mu, \tag{1.6}$$

$$\mathcal{L}_{\rho NN} = -g_\rho\bar{\psi}\gamma^\mu\boldsymbol{\tau}\psi\cdot\boldsymbol{\phi}^\rho_\mu - \frac{f_\rho}{4M_\rho}\bar{\psi}\sigma^{\mu\nu}\boldsymbol{\tau}\psi\cdot\left(\partial_\mu\boldsymbol{\phi}^\rho_\nu - \partial_\nu\boldsymbol{\phi}^\rho_\mu\right). \tag{1.7}$$

To account for the finite size of baryons and to regulate divergent integrals arising in perturbation theory, the vertices are modified by a vertex form

factor typically of the form

$$\left(\frac{\Lambda_i^2 - m_i^2}{\Lambda_i^2 + \boldsymbol{k}^2}\right)^{n_i}, \tag{1.8}$$

where Λ_i is the form factor cutoff for meson species i, m_i is its mass, $\mathbf{k}$ is the three-momentum transfer, and n_i is typically 2. The parameters of the theory (e.g. the meson masses, coupling constants, and form factor cutoffs) in principle have a physical meaning and therefore can be confirmed by experiments beyond NN collisions. Thus, meson exchange provides us with a very economical and convenient description of the interaction between two nucleons.

The qualitative form of the nucleon-nucleon interaction in relative S-states is shown in Fig. 1.2, where as an illustrative example we have plotted the $^1S_0$ partial wave interaction for the Argonne v_{18} potential [6]. The NN interaction consists of three distinct regions which are dominated by the exchange of different types of mesons. The long-range attraction is mediated by the lightest meson, the pion. The strong intermediate attraction arises from the exchange of the scalar σ meson (or alternatively, correlated two-pion exchange in the $I = J = 0$ channel). At short distances the strong repulsion is due to the exchange of vector mesons, the ρ and ω being the most significant. This picture has formed the foundation for models of the NN interaction for the past fifty years, and it was hoped that with additional two-nucleon scattering experiments it would be possible to constrain more tightly the parameters entering into the theory.

In the early 1990's the Nijmegen phase shift analysis [7] led to the construction of a new generation of *high-precision* nucleon-nucleon potential models [6, 8–10]. These interactions all fit the nearly 4000 data for *np* and *pp* scattering phase shifts up to a laboratory energy of 350 MeV with a χ^2/DOF ~ 1. In order to achieve this accuracy, the simple one-boson-exchange potentials with constant masses and coupling constants were replaced by partial-wave-dependent parameters, particularly for σ meson exchange. Among the numerous high-precision NN interactions constructed to-date, the CD-Bonn potential and the Nijmegen group of potentials are based completely on meson exchange. In Table 1.1 we show the exchanged mesons, as well as their masses, used in these two potentials. Given this next generation of nucleon-nucleon interaction models in free space, the next step is to apply these potentials to nuclear many-body problems.

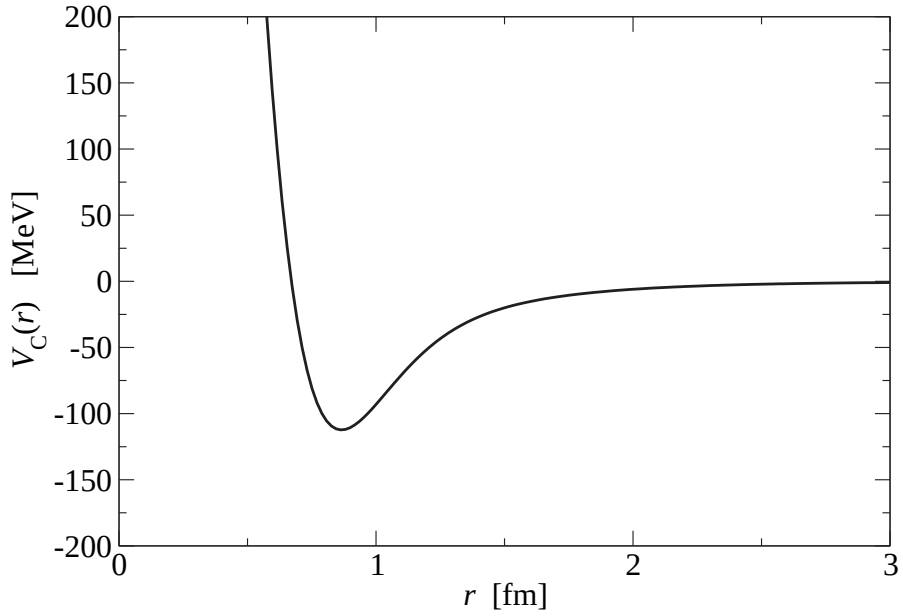

Figure 1.2: The Argonne v_{18} r-space nucleon-nucleon interaction in the $^1S_0$ partial wave. The interaction can be divided into three relatively distinct regions: the long-range one-pion-exchange part, the intermediate range attraction, and the short-distance repulsion.

	CD-Bonn			
Pseudoscalars	$\pi^0(135)$	$\pi^{\pm}(140)$		
Scalars	$\sigma_1(\sim 500)$	$\sigma_2(\sim 900)$		
Vectors	$\rho^0(770)$	$\rho^{\pm}(770)$	$\omega(782)$	
	Nijmegen 93			
Pseudoscalars	$\pi^0(135)$	$\pi^{\pm}(140)$	$\eta(549)$	$\eta'(958)$
Scalars	$\sigma(760^*)$	$a_0^0(983)$	$a_0^{\pm}(983)$	$f_0(976)$
Vectors	$\rho^0(769^*)$	$\rho^{\pm}(768^*)$	$\omega(782)$	$\phi(1020)$

Table 1.1: Mesons contributing to the CD-Bonn and Nijmegen 93 one-boson-exchange interactions. The masses of the σ_1 and σ_2 particles in the CD-Bonn potential are varied in different partial waves. We indicate with a superscript $*$ that the large widths of the σ and ρ mesons are accounted for in the Nijmegen 93 potential by replacing the propagator of a stable meson with a dispersion integral [8]. The masses are in units of MeV/c^2.

1.2 Low momentum nucleon-nucleon interactions

Before one can apply high-precision nucleon-nucleon interaction models to problems in finite nuclei and nuclear matter, one must first develop a strategy for dealing with the strong short-distance repulsion that arises from the exchange of the vector mesons. From the form of the S-wave interaction shown in Fig. 1.2, it is clear that describing the behavior of many interacting nucleons is a strong-coupling problem and that one must be careful when applying perturbation theory methods. In the past the traditional method to tame the strong short-distance repulsion was to construct the reaction matrix, or G-matrix [11–13]. Starting from the full Hamiltonian

$$H = H_0 + H_1, \tag{1.9}$$

where the unperturbed and perturbed Hamiltonians are respectively given by

$$\begin{aligned} H_0 &= \sum_{i=1}^{A} (T_i + U_i) \\ H_1 &= \sum_{i<j}^{A} V_{ij} - \sum_{i=1}^{A} U_i, \end{aligned} \tag{1.10}$$

one defines the G-matrix for nuclear matter at some given density as

$$G(\omega) = V + V\frac{Q}{\omega - H_0}G(\omega), \tag{1.11}$$

where Q is the Pauli operator which projects onto states outside of the filled Fermi sea (determined by the nuclear density), and ω is the starting energy defined below. The single-particle potential U is introduced for convenience, though it is arbitrary. It defines the single-particle energies

$$e(m) = T(m) + U(m) \tag{1.12}$$

as well as the starting energy

$$\omega = e(m) + e(n). \tag{1.13}$$

Typically, the single-particle potential is defined in Brueckner theory by

$$U(m) = \begin{cases} \sum\limits_{n \leq k_F} \langle mn|G(w)|mn - nm\rangle & , \quad m < k_F \\ 0 & , \quad m > k_F \end{cases} \tag{1.14}$$

Clearly the G-matrix is energy dependent, where the starting energy ω is determined self-consistently from equations (1.11)-(1.14). Diagrammatically the G-matrix is obtained by summing the ladder diagrams with intermediate states blocked by the Pauli exclusion principle, as shown in Fig. 1.3. One can show that the resulting effective interaction is well-behaved at short distances.

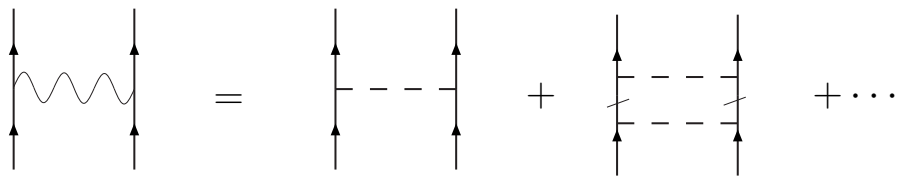

Figure 1.3: Diagrammatic representation of the G-matrix effective interaction. Hashed lines represent Pauli-blocked intermediate states.

The modern approach to dealing with the strong short-distance repulsion is to integrate out the high momentum components of the nucleon-nucleon interaction. This is performed in such a way, however, that the low energy physics encoded in the scattering phase shifts is preserved. The method for constructing such low-momentum interactions is described in detail in [14].

Starting from the half-on-shell T-matrix for free space scattering

$$T(k', k, k^2) = V_{NN}(k', k) + \frac{2}{\pi}\mathcal{P}\int_0^\infty \frac{V_{NN}(k', q)T(q, k, k^2)}{k^2 - q^2}q^2 dq, \tag{1.15}$$

we define a low-momentum half-on-shell T-matrix by

$$T_{\rm low-k}(p', p, p^2) = V_{\rm low-k}(p', p) + \frac{2}{\pi}\mathcal{P}\int_0^\Lambda \frac{V_{\rm low-k}(p', q)T_{\rm low-k}(q, p, p^2)}{p^2 - q^2}q^2 dq, \tag{1.16}$$

where $\mathcal{P}$ denotes the principal value and the cutoff Λ is in general arbitrary. These two T-matrices are required to be identical for momenta $p < \Lambda$, and it can be shown [15] that a $V_{\rm low-k}$ defined by

$$V_{\rm low-k} = \hat{Q} - \hat{Q}'\int \hat{Q} + \hat{Q}'\int \hat{Q}\int \hat{Q} - \hat{Q}'\int \hat{Q}\int \hat{Q}\int \hat{Q} + \cdots \tag{1.17}$$

will satisfy this requirement. This is just the Kuo-Lee-Ratcliff folded diagram effective interaction [16, 17]. In the above equation, $\hat{Q}$ is an irreducible vertex function and $\hat{Q}'$ is obtained by removing from $\hat{Q}$ all terms first order in the interaction V_{NN}. There are several schemes [18, 19] available for accurately computing $V_{\rm low-k}$, and each scheme preserves the deuteron binding energy. Under this renormalization group procedure, all of the high precision V_{NN} flow, as $\Lambda \to 2.0$ fm^{-1}, to a nearly unique interaction $V_{\rm low-k}$, as shown in Figs. 1.4 and 1.5 reproduced from [14]. The resulting $V_{{\rm low}-k}$ is well-behaved at short distances and moreover it is energy-independent (in contrast to the traditional G-matrix). Therefore, low momentum interactions are very convenient for perturbative calculations of many-body nuclear systems.

The momentum cutoff of $\Lambda = 2.0$ fm^{-1} is the CM momentum corresponding to a laboratory energy of ~ 350 MeV, which is precisely the energy beyond which no information from the Nijmegen phase shift analysis is incorporated into realistic NN interactions. Thus, one can view the construction of low-momentum interactions as integrating out the experimentally unconstrained components of the NN interaction.

Eliminating the large-momentum components of the NN interaction in a way that preserves the phase shifts is reminiscent of the Moszkowski-Scott separation method [20]. This procedure was employed in the 1960's to tame the strong short-distance repulsion in relative S-states by balancing it against part of the mid-range attraction. The part of the NN interaction that remains is used as an effective interaction that approximates the G-matrix. In Chapter 2 we compare the momentum-space decimation procedure used to construct the low momentum nucleon-nucleon interaction $V_{\rm low-k}$ with the configuration-

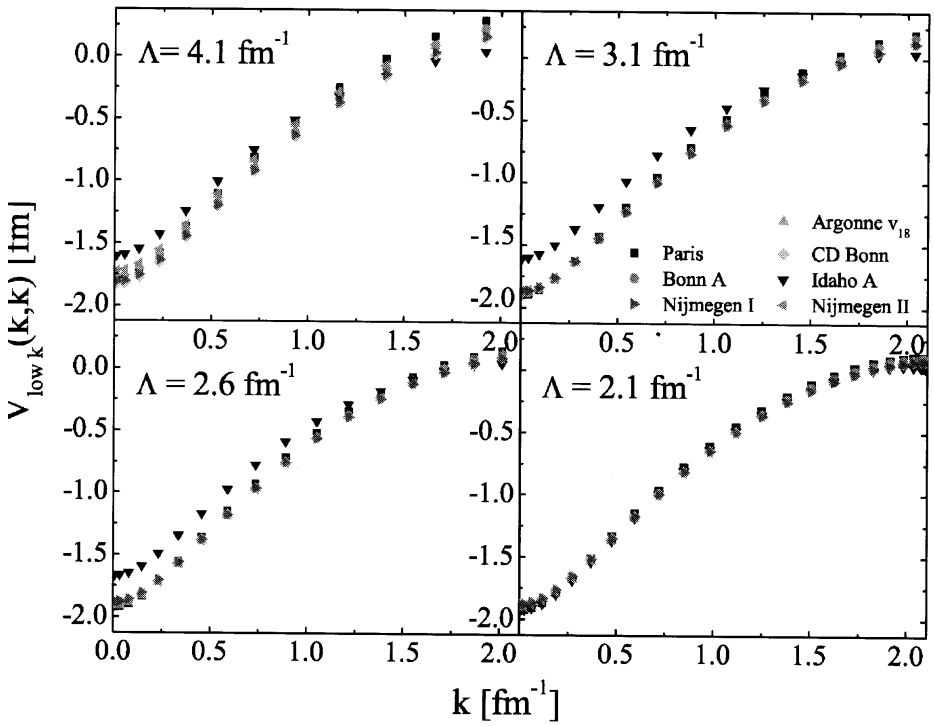

Figure 1.4: Diagonal matrix elements of $V_{\mathrm{low}-k}$ for different high-precision potentials in the $^1S_0$ partial wave with various cutoffs Λ. Reproduced from reference [14].

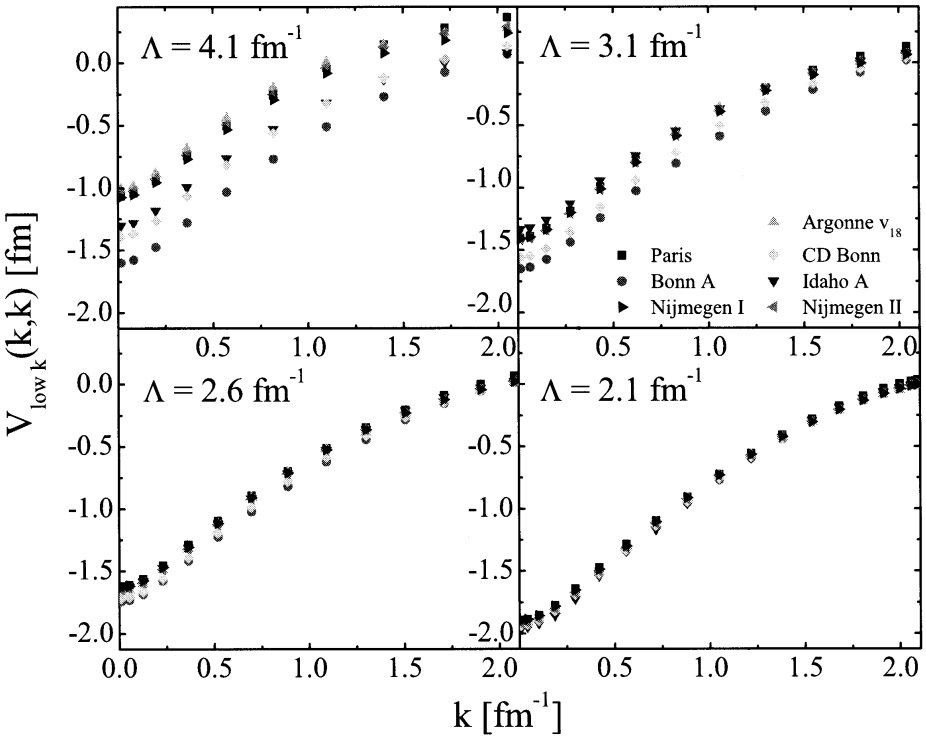

Figure 1.5: Diagonal matrix elements of $V_{\mathrm{low}-k}$ for different high-precision potentials in the $^3S_1$ partial wave with various cutoffs Λ. Reproduced from reference [14].

space separation method of Moszkowski and Scott. Each procedure defines a separation of scales in the nucleon-nucleon interaction, and the extent to which these two scales coincide is studied. By studying the effects of the separation method on the relative S-state Kallio-Kolltveit potential, it is found that close agreement with $V_{\mathrm{low-k}}$ is obtained as the configuration-space cutoff is lowered to ~ 1.0 fm. This study helps to illuminate the $V_{\mathrm{low}-k}$ decimation procedure and to justify the use of low momentum interactions in nuclear structure calculations.

1.3 Beyond free-space nuclear interactions

Despite the improved precision of both nuclear interaction models and quantum many-body methods, there remain experimental observables which cannot be reproduced with two-body interactions alone. The most persistent is the saturation of nuclear matter. Ever since it was discovered how to tame the strong short distance repulsion in relative S-states through the construction of the G-matrix, the main problem for nuclear interaction models has been to reproduce the saturation energy and density of symmetric nuclear matter. Since different many-body methods, such as the Goldstone linked-diagram expansion [13] and variational calculations [21], give very similar results for the binding energy as a function of density for a given nuclear interaction, it is widely believed that any deviations from the empirical saturation point must be due to deficiencies in the nuclear interaction model. From the semi-emipirical mass formula, which describes the nuclear energy as a function of proton and neutron number,

$$E_B(Z,N) = \alpha_1 A - \alpha_2 A^{2/3} - \alpha_3 \frac{Z(Z-1)}{A^{1/3}} - \alpha_4 \frac{(N-Z)^2}{A} \tag{1.18}$$

one can extract the parameter α_1 to be -16 MeV by fitting across a wide range of nuclei. This volume term describes the energy of a single nucleon added to an infinite system of protons and neutrons at a density of $n_0 = 0.16$ nucleons/fm^3, the density at which symmetric nuclear matter saturates. Although different models of the NN interaction give different results for the binding energy and density at the saturation point, they all lie along the Coester band which does not pass through the empirical saturation energy and density [22–25]. Typically, either the saturation density is correct and the binding is too weak or the binding energy is correct and the saturation density is too large. In finite nuclei, the analogous problem is that one cannot simultaneously fit both the binding energy of the nucleus and its rms charge radius. The fact that no two-nucleon potential that is fit to scattering phase

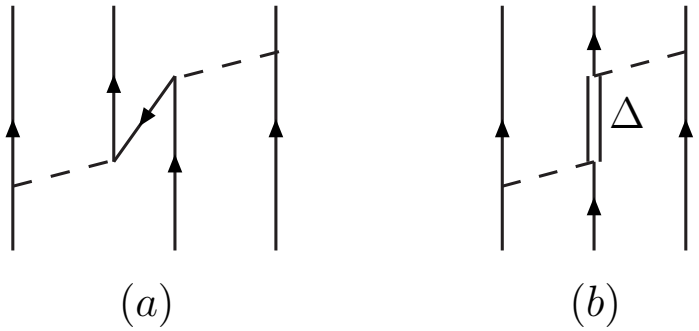

Figure 1.6: Some processes that form the microscopic origin of three-nucleon forces. Shown are (a) nucleon-antinucleon excitations and (b) resonance-hole excitations (in this case with an intermediate Δ isobar).

shift data and deuteron properties can reproduce these properties suggests that something fundamental is missing in this description of the nuclear interaction.

The failure of two-body interactions alone to describe the fine details of nuclear structure was never really a surprise. In fact, as early as 1939 [26] it was suggested that three-body forces should be rather significant for nuclear structure in contrast to atomic structure. Today three-body forces form the foundation for most studies of dense nuclear matter [27–31]. As shown in Fig. 1.6, three-body forces commonly result from relativistic effects, such as intermediate nucleon-antinucleon states, or from effects due to the intrinsic structure of nucleons.

An alternative approach toward developing a formalism for nuclear structure calculations at finite density is to consider changes to the properties of nucleons and mesons inside of a nucleus. Since hadrons are composed of quarks, one ought to expect that inside of a nucleus the individual nucleons, as well as the exchanged mesons, may have very different properties than in free space. In fact, the European Muon Collaboration (EMC) [32] made the surprising discovery that nucleon structure functions are modified inside of a nucleus. Furthermore, polarization transfer experiments at Jlab [33] have shown that the electromagnetic form factors of a proton are altered in a dense medium compared to free space. In fact, the properties of hadrons in-medium is currently one of the most widely studied topics in nuclear physics.

Modifications to meson properties inside a nuclear medium give rise to density-dependent two-body interactions, as shown in Fig. 1.7. We have already emphasized that when a free-space two-body interaction is applied to a dense nuclear system, certain excitations that are present in the many-body

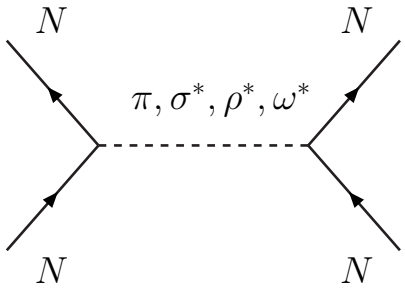

Figure 1.7: The medium-modified nucleon-nucleon interaction arising from the exchange of light mesons whose in-medium masses are expected to differ from their free-space values.

system are left out. In the language of hadronic medium modifications, these degrees of freedom give rise to a density-dependent meson mass and width through many-body self-energy corrections to the meson propagator

$$D(\omega, \boldsymbol{q}) = \frac{1}{\omega^2 - \boldsymbol{q}^2 - m^2 - \Sigma_{\rm vac}(q) - \Sigma_{\rm med}(\omega, \boldsymbol{q})}, \tag{1.19}$$

where contributions to $\Sigma_{\rm med}$ are shown graphically in Fig. 1.8. In general, both s-channel and t-channel processes can contribute, which give rise to an in-medium spectral function defined as the imaginary part of the propagator

$$A(\omega, \boldsymbol{q}) = \frac{1}{\pi} \frac{\mathrm{Im}\Sigma(\omega, \boldsymbol{q})}{\left(\omega^2 - \boldsymbol{q}^2 - m^2 + \mathrm{Re}\Sigma(\omega, \boldsymbol{q})\right)^2 + \mathrm{Im}\Sigma(\omega, \boldsymbol{q})^2}. \tag{1.20}$$

The real part of the self-energy contributes to the effective mass of the particle while the imaginary part leads to collisional broadening of the width. In the low-density limit [34], the in-medium self-energy depends only on the forward meson-nucleon scattering amplitude f_{mN} and the nuclear density n

$$\Sigma_{\rm med}(\omega, \mathbf{q}; n) = n f_{mN}(\omega, \boldsymbol{q}). \tag{1.21}$$

Such effects have been studied by various groups [35–37], though the results are not all in agreement. In particular, most studies agree that there is a significant broadening of the spectral functions for the vector mesons, but the calculated mass shifts can be significant or negligible. Such phenomena can also be seen in high-pressure atomic gases, where collisions with background particles cause both a shift and broadening of the spectral lines.

An alternative motivation for considering in-medium hadronic masses is

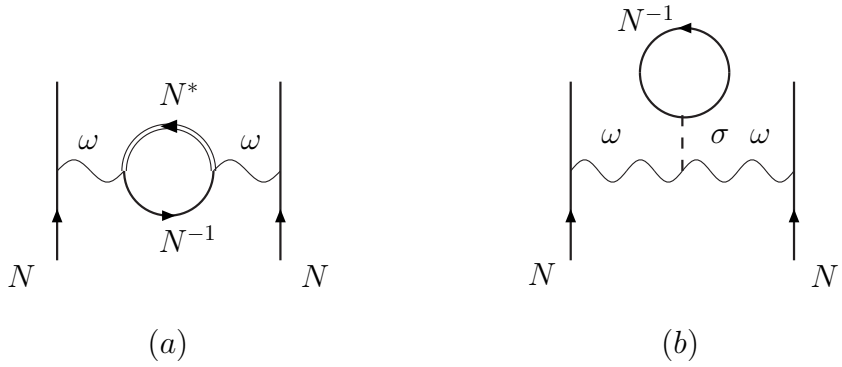

Figure 1.8: Modifications to meson masses (in this case the ω meson mass) in medium due to hadronic many-body effects. Shown are both s-channel (a) and t-channel (b) contributions.

based on the notion of chiral symmetry restoration in dense matter. Given the fact that light quarks have masses on the order of 5-10 MeV, while typical hadron masses are nearly 1 GeV, it is believed that most hadronic mass is generated dynamically from the nontrivial QCD vacuum. But as the density increases, the interaction strength among quarks and gluons decreases due to the running of the QCD coupling constant, which to lowest order in perturbation theory is

$$\alpha_s(k^2) \simeq \frac{1}{\beta_0 \ln(k^2/\Lambda^2)}, \tag{1.22}$$

where β_0 is a constant and Λ is the QCD scale of ~ 220 MeV. Eventually, at some critical density n_c there exists a phase transition to a state of deconfined hadronic matter, which is expected to coincide with chiral symmetry restoration, but along the way it is expected that the dynamically generated mass will shed. The order parameter associated with this phase transition is the scalar quark condensate (chiral condensate) $\langle \bar{q}q \rangle$ or alternatively the pion decay constant f_π, which goes as $\left(f_\pi^*/f_\pi\right)^2 \sim \langle \bar{q}q \rangle^* / \langle \bar{q}q \rangle$, where * denotes an in-medium quantity.

There are a number of models that connect the order parameter for chiral symmetry restoration with dynamical mass generation. Unfortunately, lattice gauge theory is presently unable to solve QCD at finite density, so one must rely on these models to describe the behavior of hadronic matter in this region of the phase diagram. In the Nambu-Jona-Lasinio (NJL) model, which models QCD as a system of quarks interacting through zero-range contact interactions, the dynamical hadron mass results from the nonzero scalar quark condensate.

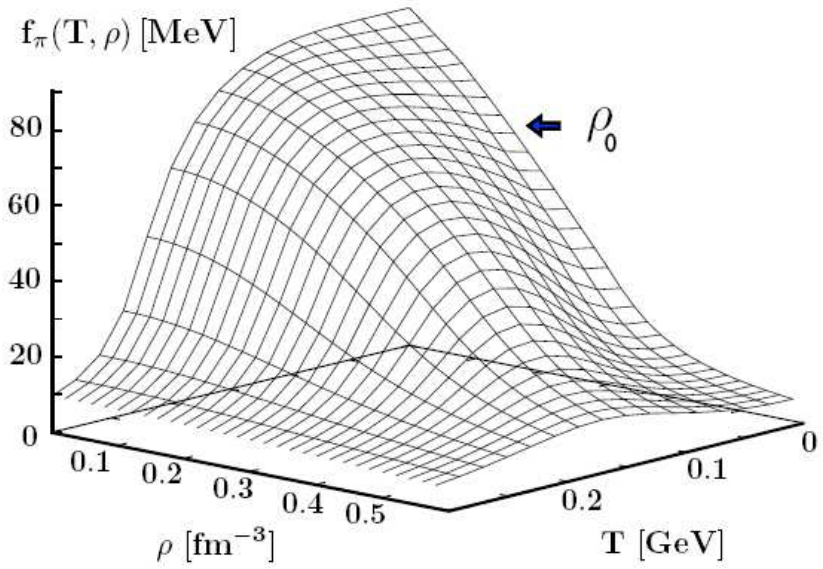

Figure 1.9: The pion decay constant f_π as a function of temperature and density in the NJL model. Figure taken from [40].

In vacuum, where the quark condensate is nonzero, bare quarks evolve into constituent quarks with masses approximately 300 MeV. In the NJL model the constituent quark mass is directly proportional to the scalar quark condensate

$$\frac{m^*}{m} \sim \frac{\langle \bar{q}q \rangle^*}{\langle \bar{q}q \rangle} \sim \left(\frac{f_\pi^*}{f_\pi} \right)^2 , \tag{1.23}$$

which is known as "Nambu scaling". This scaling seems to come out in QCD sum rule calculations [38] also. It holds in the Harada and Yamawaki renormalization group theory [39] for high temperatures or densities approaching chiral restoration which takes place at the fixed point where $m_V^\star$ and $g_V^\star$ go to zero. In Fig. 1.9 we show the order parameter for chiral symmetry restoration as a function of temperature and density [40] calculated within the NJL model. We see that even at nuclear matter density, ρ_0, the pion decay constant decreases by approximately 20-30%.

Another way to see that dynamically generated masses scale was introduced by Lutz *et al.* [41] through the Gell-Mann, Oakes, Renner relation

$$f_\pi^2 m_\pi^2 = 2\bar{m}\langle \bar{q}q \rangle, \tag{1.24}$$

where $\bar{m}$ is the bare quark mass. Both $\bar{m}$ and m_π, which is protected against

scaling to the extent that it is a Goldstone boson, do not scale. This relation would then produce

$$\frac{f_\pi^\star}{f_\pi} = \frac{\sqrt{\langle\bar{q}q\rangle^\star}}{\sqrt{\langle\bar{q}q\rangle}}, \tag{1.25}$$

which holds quite well for low densities[1]. In fact, for low densities one has the relation [42–44]

$$\frac{\langle\bar{q}q\rangle^\star}{\langle\bar{q}q\rangle} = 1 - \frac{\sigma_{\pi N}}{f_\pi^2 m_\pi^2} n \tag{1.26}$$

where n is the vector density and $\sigma_{\pi N}$ is the pion-nucleon sigma term known experimentally to be ~ 45 MeV. Eq. (1.26) holds to linear approximation.

In Brown-Rho scaling (BRS) [45], which was motivated by the attempt to build scale invariance into chiral effective Lagrangians, one associates hadronic masses with the breaking of chiral symmetry according to

$$\sqrt{\frac{g_A}{g_A^*}}\frac{m_N^*}{m_N} = \frac{m_\sigma^*}{m_\sigma} = \frac{m_\rho^*}{m_\rho} = \frac{m_\omega^*}{m_\omega} = \frac{f_\pi^*}{f_\pi} = \Phi(n), \tag{1.27}$$

where g_A is the axial coupling constant, Φ is a function of the nuclear density n with $\Phi(n_0) \simeq 0.8$ from Eq. (1.26). This linear dependence on the pion decay constant, rather than its square, is different from that obtained by QCD sum rules and low density theorems, though at higher densities Koch and Brown [46] showed that the entropy from reduced mass hadrons fit the entropy from lattice gauge simulations if one had Nambu scaling (1.23) i.e., the hadron *in-medium* mass scaled linearly with the quark scalar density. Today, Brown-Rho scaling has a firm foundation in the Hidden Local Symmetry (HLS) field theory. Since the particular details will not be of immediate importance to the rest of our discussion, we provide in Appendix A a short summary of HLS and how it relates to BRS at finite temperature and density.

Experimental efforts to determine the properties of hadrons in medium can be classified into two categories: heavy ion collisions and energetic probes of cold nuclear matter. The advantage of the former is that the temperature and density of the matter created at the instant of such collisions are large enough that chiral symmetry is expected to be restored, if only very briefly. It has been suggested [47–50] that as the hot/dense matter evolves from the chirally restored phase to the normal hadronic phase, the dileptons emitted during all stages of the fireball evolution should be able to probe the restoration of chiral symmetry through their decays from the vector mesons, the most

[1]To be precise, this relation in medium is a relation for the space component of the pion decay constant which is different from the time component since Lorentz invariance is broken.

important of which is the short-lived ρ meson. Although relativistic heavy ion collisions are promising as a source of information regarding chiral symmetry breaking/restoration in hot and dense matter, they are only indirectly relevant for understanding nuclei under normal conditions.

Experiments involving energetic probes of cold nuclear matter are more important for the purposes we are pursuing in the present work. In principle they can provide information about the spectral properties of mesons propagating through nuclear matter and thereby help to understand the medium-dependent nuclear interaction. Such experiments have, in fact, been performed for all of the light mesons important in nuclear structure physics. Studies of deeply-bound pionic atoms [51] find only a small increase in the π^- mass at nuclear matter density and a related decrease in the π^+ mass. Experimental information on the scalar and vector particles comes from mass distribution measurements of in-medium decay processes. Recent photoproduction experiments [52] of correlated pions in the $I = J = 0$ channel (σ meson) have found that the distribution is shifted to lower masses in medium. The vector mesons have been the most widely studied. Whereas the situation is clear with the ω meson, the mass of which drops by $\sim 14\%$ at nuclear matter density [53], with the ρ meson it is still unclear [54, 55].

BRS was one of the first attempts in nuclear physics to formulate medium dependent effects associated with the approach to chiral restoration as the scale, either with temperature or density or with both, was increased. Although 3NF play a large role in many modern discussions of in-medium nuclear interactions, relatively little emphasis has been devoted to the study of medium-modified two-body interactions. Indeed, it is one of the aims of this thesis to encourage the application of hadronic medium modifications to problems in nuclear structure and to better understand the connection between this approach and the more traditional use of three-body forces. Our ultimate goal is to apply these in-medium interactions to studies of both finite nuclei and nuclear matter to test whether the hypothesis of dropping masses is consistent with what we know experimentally from nuclear structure.

In Chapter 3 we begin our discussion with a study of nuclear matter, one of the simplest nuclear many-body systems. We revisit the problem of the saturation of symmetric nuclear matter by way of an all-order ring diagram summation. We find that low-momentum interactions succumb to the same problem that has traditionally plagued realistic models of the NN interaction, namely, that the saturation density is much too high. We consider the effect of introducing modified meson masses in the Nijmegen I potential and the Bonn-B potential. We find that in both cases the saturation density is in much better agreement with experiment, though the binding is slightly weak. By

generalizing the ring diagram summation for asymmetric nuclear matter, we turn our attention to the neutron star equation of state. From the medium-modified Bonn-B potential we extract the neutron excess as a function of the neutron star density. We suggest that such calculations might be important for the understanding of kaon condensation in neutron stars.

In Chapter 4 we discuss symmetric nuclear matter within the framework of Landau Fermi liquid theory. The low momentum nucleon-nucleon interaction $V_{\mathrm{low}-k}$ is used to calculate the effective interaction between quasiparticles on the Fermi surface, from which we extract the quasiparticle effective mass, the nuclear compression modulus, the symmetry energy, and the anomalous orbital gyromagnetic ratio. The exchange of density, spin, and isospin collective excitations is included through the Babu-Brown induced interaction, and it is found that in the absence of three-body forces the self-consistent solution to the Babu-Brown equations is in poor agreement with the empirical values for the nuclear observables. This is improved by lowering the nucleon and meson masses according to Brown-Rho scaling, essentially by including a scalar tadpole contribution to the meson and nucleon masses, as well as by scaling the axial coupling constant g_A. We suggest that modifying the masses of the exchanged mesons is equivalent to introducing a short-range three-body force, and the net result is that the Brown-Rho double decimation [56] is accomplished all at once.

Our study of finite nuclei begins in Chapter 5 by revisiting the old problem of Kuo-Brown shell model effective interactions. Previous G-matrix calculations showed that when core polarization diagrams are included to all orders in perturbation theory, the final effective interaction very close to the original bare G-matrix alone. We discuss a new method for summing an infinite number of core polarization diagrams using the low-momentum nucleon-nucleon interaction $V_{\mathrm{low-k}}$. The summation is based on the Kirson-Babu-Brown (KBB) induced interaction approach in which the vertex functions are obtained self consistently by solving a set of non-linear coupled equations. It is found that the solution of these equations is simplified by using $V_{\mathrm{low-k}}$, which is energy independent, and by employing Green functions in the particle-particle and particle-hole channels. We have applied this approach to the *sd*-shell effective interactions and find that the results calculated to all orders using the KBB summation technique are remarkably similar to those of second-order perturbation theory, average differences being less than 10%. Thus, in our future calculations we can be confident that a second-order calculation should be sufficient to capture the essentials of an all-order calculation.

In Chapter 6 we present shell model calculations for the β-decay of the ^{14}C ground state to the ^{14}N ground state, treating the states of the $A =$

14 multiplet as two $0p$ holes in an ^{16}O core. This decay has long been a puzzle for nuclear structure theorists because the decay is an allowed Gamow-Teller transition, and therefore its half-life should be on the order of tens of minutes instead of the observed half-life of 5730 years. Our calculation employs low-momentum nucleon-nucleon interactions derived from the realistic Bonn-B potential, and we find that the Gamow-Teller (GT) matrix element is too large to describe the known lifetime. By using a modified version of this potential that incorporates the effects of Brown-Rho scaling medium modifications, we find that the GT matrix element vanishes for a nuclear density around 85% that of nuclear matter. We find that the splitting between the $(J^\pi, T) = (1^+, 0)$ and $(J^\pi, T) = (0^+, 1)$ states in ^{14}N is improved using the medium-modified Bonn-B potential and that the transition strengths from excited states of ^{14}C to the ^{14}N ground state are compatible with recent experiments. Our findings present compelling evidence that the anomalously long lifetime of ^{14}C results from medium effects on nuclear interactions.

Taken as a whole, these initial studies suggest that the use of medium-modified nuclear interactions can provide a convenient formalism for extending the model of the nuclear interaction into regions close to nuclear matter density.

Chapter 2

$V_{\mathrm{low}-k}$ and the Moszkowski-Scott Separation Method

2.1 Introduction

The central idea in the effective field theory (EFT)-renormalization group (RG) approach to constructing low momentum NN interactions is that the fine short-distance details of the nuclear interaction are unconstrained by low energy physical observables. As evidenced by the large number of high-precision NN potential models [6, 8–10], which all reproduce the nearly 4000 experimental phase shift data with a χ^2/DOF$\sim$ 1, one might expect there to be infinitely many interactions which differ in their short-distance dynamics but which yield the same low energy nuclear observables. These ideas are based on the notion of the separation of scales, whereby the degrees of freedom beyond some scale λ are integrated out and incorporated into the low-energy theory through counterterms [57]. The main idea is that there exists a separation of scales that facilitates this division, and in the case of standard chiral effective field theory, one uses the chiral symmetry breaking scale $\Lambda_{\chi SB} \sim 1$ GeV. In low energy nuclear physics there is another scale of importance: the pion production threshold in two-nucleon scattering, which becomes important near a laboratory energy of 350 MeV. In fact, beyond this lab energy, no experimental phase shift data is incorporated into realistic NN potential models. It has been shown [14, 58] that by introducing a momentum space cutoff Λ, all high precision NN potentials that reproduce the experimental phase shift data up to $E_{\mathrm{lab}} \simeq 350$ MeV flow to a nearly unique interaction $V_{\mathrm{low-k}}$ as the cutoff is lowered to $\Lambda \simeq 2$ fm^{-1}. Removing the large momentum modes of an interaction corresponds to removing the short distance details, but the exact extent to which the momentum space decimation procedure removes these

short distance details is not well understood. In particular, it would be useful to understand whether the momentum space cutoff of ~ 2 fm^{-1} corresponds to an approximate cutoff in position space. The purpose of the present paper is to investigate this question.

The *more effective* effective field theory approach, which introduces this second decimation scale, is reviewed in [56]. It is *more effective* in the sense that the cutoff Λ is chosen so as to include all experimental data that have been converted into precision NN potentials. Since the maximum momentum in the data corresponds to a cms momentum $\Lambda \simeq 2$ fm^{-1}, it makes no sense to increase Λ, which would then include contested inner parts of the potentials, or to decrease Λ, which would mean cutting out some of the experimental data. With Λ chosen as it is, all well measured and well analyzed data are included in the nearly unique $V_{\rm low-k}$.

Removing the large momentum or short distance details of an interaction in order to construct an effective interaction is not, however, a new tool in nuclear physics. The separation method of Moszkowski and Scott [20] provided 40 years ago a means by which the nuclear interaction can be uniquely divided into a short distance and long distance part. This separation is made in such a way that the short distance potential gives no phase shift for free particle scattering; the long distance part then gives the same phase shift as the full interaction and is used as a first approximation to the effective interaction in nuclear matter. Both the separation method and $V_{{\rm low}-k}$ decimation establish a separation of scales in the nuclear interaction, the former in configuration space and the latter in momentum space. The extent to which these two scales coincide will be a further investigation of this paper.

We have chosen to compare the RG/EFT approach and the separation method by way of the Kallio-Kolltveit potential [59, 60], a relative S-state potential that has been chosen primarily for its simplicity. By comparing the resulting long-distance interactions, it is hoped that semi-quantitative connections can be established between the two methods.

2.2 Low momentum nucleon-nucleon interactions

Because the nuclear force cannot at present be derived from the underlying theory of QCD, a number of phenomenological meson-exchange models have been developed to describe the NN interaction. At large distances all of these potentials have the one-pion-exchange character, but at intermediate and short distances they differ significantly. Despite these differences, all of the high

precision potentials correctly reproduce the experimentally observed deuteron binding energy and low energy nucleon phase shift data. To remove the model dependence in the NN interaction, the renormalization group is used to construct a unique low momentum effective interaction $V_{\rm low-k}$ according to the procedure described below.

A principal requirement of any RG procedure is that low energy observables–in this case the deuteron binding energy and low energy T-matrix–be preserved under the RG transformation. So, beginning with the full-space half-on-shell T-matrix

$$T(k', k, k^2) = V_{NN}(k', k) + \frac{2}{\pi}\mathcal{P}\int_0^\infty \frac{V_{NN}(k', q)T(q, k, k^2)}{k^2 - q^2}q^2 dq, \tag{2.1}$$

we define a low-momentum half-on-shell T-matrix by

$$T_{\rm low-k}(p', p, p^2) = V_{\rm low-k}(p', p) + \frac{2}{\pi}\mathcal{P}\int_0^\Lambda \frac{V_{\rm low-k}(p', q)T_{\rm low-k}(q, p, p^2)}{p^2 - q^2}q^2 dq, \tag{2.2}$$

where $\mathcal{P}$ denotes the principal value and the cutoff Λ is arbitrary for the moment. These two T-matrices are required to be identical for momenta $p < \Lambda$, and it can be shown [15] that a $V_{\rm low-k}$ defined by

$$V_{\rm low-k} = \hat{Q} - \hat{Q}'\int\hat{Q} + \hat{Q}'\int\hat{Q}\int\hat{Q} - \hat{Q}'\int\hat{Q}\int\hat{Q}\int\hat{Q} + \cdots \tag{2.3}$$

will satisfy this requirement. In the above equation, $\hat{Q}$ is an irreducible vertex function and $\hat{Q}'$ is obtained by removing from $\hat{Q}$ all terms first order in the interaction V_{NN}. Under this RG procedure, all of the high precision V_{NN} flow, as $\Lambda \to 2.0$ fm^{-1}, to a nearly unique interaction $V_{\rm low-k}$, whose relative S-states will be a subject of analysis later in the paper.

2.3 The separation method

Idealized nuclear matter, an infinite system of protons and neutrons at constant density interacting through only the strong force, represents one of the simplest nuclear many-body systems. The properties of nuclear matter around the saturation point are well-known empirically, which makes this system convenient for testing models of the NN interaction. Although many-particle correlations (that is, greater than two) could in theory be important for describing nuclear matter, it is generally assumed that they should be small [61]. This leads to the *independent pair* approximation for nuclear matter in which

the interaction between two particles is treated exactly within the model, and the effect of all remaining particles is to produce an average single-particle (s.p.) potential U. This average potential determines the s.p. unperturbed wavefunctions through

$$H_0\phi_{ab} = (T+U)\phi_{ab} = \epsilon_{ab}\phi_{ab}. \tag{2.4}$$

The unperturbed relative wavefunction ϕ_{ab} is then just the antisymmetrized product wavefunction of ϕ_a and ϕ_b. The perturbed wavefunction ψ_{ab} is defined by

$$[T(a) + T(b) + V_{NN}(a,b)]\psi_{ab} = e_{ab}\psi_{ab}. \tag{2.5}$$

Typical perturbed and unperturbed wavefunctions for a hard core potential are shown in Fig. 2.1

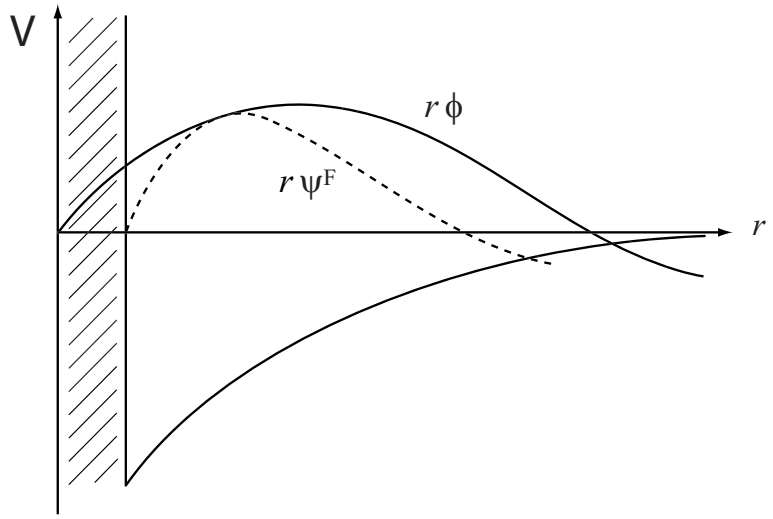

Figure 2.1: Unperturbed wavefunction ϕ and perturbed wavefunction ψ for a hard core potential.

Expanding ψ in terms of the eigenstates $\{\phi_i\}$ and imposing antisymmetry on the total N-particle wavefunction leads to the Bethe-Goldstone equation

$$\psi_{ab} = \phi_{ab} + \frac{Q_{ab}}{e_{ab} - H_0} V_{NN}\psi_{ab}, \tag{2.6}$$

where Q is the Pauli operator which projects outside of the filled Fermi sea. Defining the G-matrix (or reaction matrix) analogous to the T-matrix for free-particle scattering we obtain

$$G\phi = V\psi. \tag{2.7}$$

Rewriting Eq. (2.6) we find the operator equation

$$G(\omega) = V + V\frac{Q}{\omega - H_0}G(\omega), \tag{2.8}$$

for the G-matrix. The starting energy ω is defined by

$$\omega = \epsilon_m + \epsilon_n \tag{2.9}$$

for the scattering of states m and n. The mean field potential U defining the single-particle energies accounts for the average effect from all other nucleons

$$U(m) = \begin{cases} \sum_{n \leq k_F} \langle mn|G(w)|mn - nm\rangle & , \quad m < k_F \\ 0 & , \quad m > k_F \end{cases} \tag{2.10}$$

Thus, in the independent-pair approximation, two-particle scattering in-medium is treated with the Brueckner G-matrix while the effect of all other particles is incorporated into the s.p. potential U. The total energy is therefore just the sum of the individual kinetic energies together with the interaction energies of each pair of particles (the latter being determined by the two-particle scattering properties encoded in the reaction matrix)

$$E = \sum_m T_m + \frac{1}{2}\sum_{m,n} \langle mn|G(\omega)|mn - nm\rangle \,, \tag{2.11}$$

where the sums are performed over just the occupied states defined by the Fermi momentum k_F.

Moszkowski and Scott introduced the separation method [20] to simplify and illuminate Brueckner's approach to the nuclear many-body problem. The purpose of the G-matrix is to deal with the difficulties associated with the strong short-distance repulsion in the nuclear interaction. This repulsion makes impossible a simple treatment with perturbation theory, but the construction of the reaction matrix produces an effective interaction that is well-behaved at short distances. However, in general the G-matrix is not simple to calculate. The invention of the separation method was guided by insight into the properties of the two-particle relative wavefunction in nuclear matter, and it provides us with an elegant method for approximating the G-matrix, as we now describe in detail.

First, we note that the two-particle relative wavefunction in nuclear matter has no phase shift. In other words, as $r \to \infty$, $\psi_{ab} \to \phi_{ab}$. This follows from the Pauli principle, which allows only virtual scattering to states above the filled

Fermi sea. From the Bethe-Goldstone equation (2.6), all of the contributions to the perturbed wavefunction beyond the leading unperturbed wavefunction go to zero at large r since it is assumed that the potential V vanishes sufficiently rapidly at large distances. In free-space scattering this argument does not apply because the denominator can vanish for intermediate states with the same energy as the incident pair. But in nuclear matter there are no such states available. Therefore, the contributions from states outside of the filled Fermi sea can only deform the relative wavefunction at short distances, and a measure of this deformation is the wound integral defined by

$$\kappa_{ab} = \int |\phi_{ab} - \psi_{ab}|^2 \, d^3r_1 d^3r_2. \tag{2.12}$$

If κ_{ab} is small, we expect the independent pair approximation to be valid. Calculations [12] performed within the framework of Brueckner theory show that the two-particle relative wavefunction in nuclear matter is essentially equal to the unperturbed wavefunction beyond ~ 1 fm. Because of the Pauli exclusion principle, it must "heal" to the unperturbed wavefunction at a distance of $\sim k_F^{-1} \simeq (2m_\pi)^{-1}$.

The essential idea of the separation method is to "cancel" the problematic hard core with part of the short-distance attractive well and use the remaining long-distance part as the effective interaction. A repulsive interaction–even an infinite hard core–produces a finite negative phase shift, whereas an attractive potential produces a positive phase shift. For incident energies that are not too large, realistic models of the NN interaction give an overall positive phase shift in relative S-states. In these cases it is possible to combine the repulsive core with the attractive well up to a distance d such that the combination of the two "cancels". One way to quantify this is to require that the phase shift for the short-distance potential, $V_s(r) = V(r)\theta(d-r)$, gives zero phase shift for free particle scattering. The remaining part of the potential, called V_l, will then produce the same free particle phase shifts as the original, but without the presence of the hard core. Thus,

$$V_{NN} = V_s + V_l = V_{NN}\theta(d-r) + V_{NN}\theta(r-d) \tag{2.13}$$

Fig. 2.2 shows the separation for a general NN potential. If the free-particle phase shift is zero for V_s alone, then we obtain for the separation distance d

$$\left.\frac{1}{r\psi^F}\frac{d\left(r\psi^F\right)}{dr}\right|_d = \left.\frac{1}{r\phi}\frac{d\left(r\phi\right)}{dr}\right|_d \tag{2.14}$$

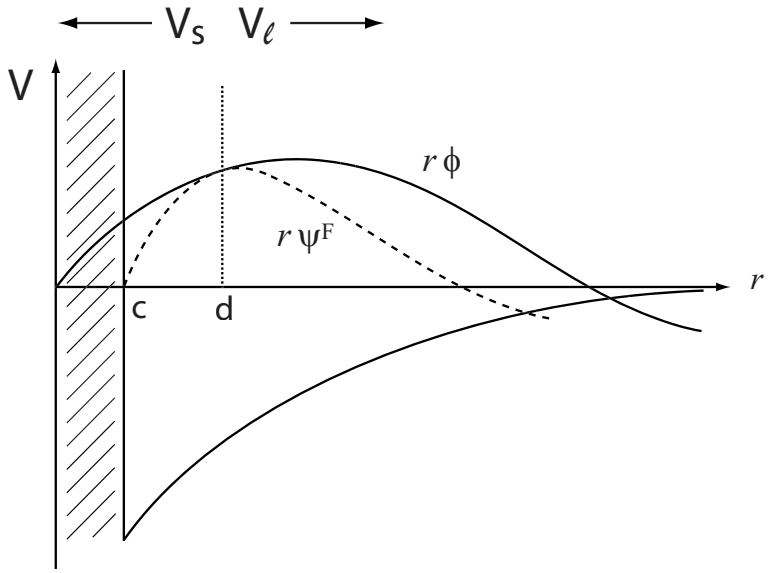

Figure 2.2: Separation of the NN potential into short and long distance parts by requiring equality of the logarithmic derivatives for the unperturbed and perturbed relative wavefunctions.

simply by solving the Schrödinger equation for $r < d$ and matching it to the unperturbed wavefunction for $r > d$. In this equation the superscript F refers to the free-space perturbed wavefunction.

Since free particle phase shifts will depend on both the relative angular momentum state of the interacting nucleons and their relative linear momentum, so too will the separation distance. In practice, one can work with a separation distance that is momentum dependent or else fix the separation distance and include corrections. Indeed, in the Kuo-Brown interaction [62] the separation method was used to construct a momentum-independent separation distance for the individual S-states, but the Reference Spectrum method [63] was convenient for states of other angular momenta.

By separating the potential into V_s and V_l in the manner described above, the in-medium relative wavefunction is approximately equal to the free-space perturbed wavefunction ψ_s due to V_s alone. For $r < d$ the two-particle relative wavefunction in free space ψ^F is equal to ψ_s, the free-space relative wavefunction due to V_s alone. At small distances, contributions to ψ^F come largely from high-momentum states. Small momentum states that would not be included in the in-medium relative wavefunction do contribute to ψ^F, but their phase space is much smaller than for the large-momentum states. In other words, effects due to nuclear matter are relatively weak below d, and $\psi^F = \psi_s (r < d)$

should be a good approximation to ψ in this region. For distances larger than d, ψ^s is just the two-particle unperturbed wavefunction ϕ, which we already argued is a good approximation to the in-medium relative wavefunction for large distances due to the Pauli principle "healing" of the wavefunction. Similarly, the free-space relative wavefunction due to V_l alone is equal to ϕ for $r < d$, and for distances larger than d, $\psi_l = \psi^F$. These observations are shown in Fig. 2.3

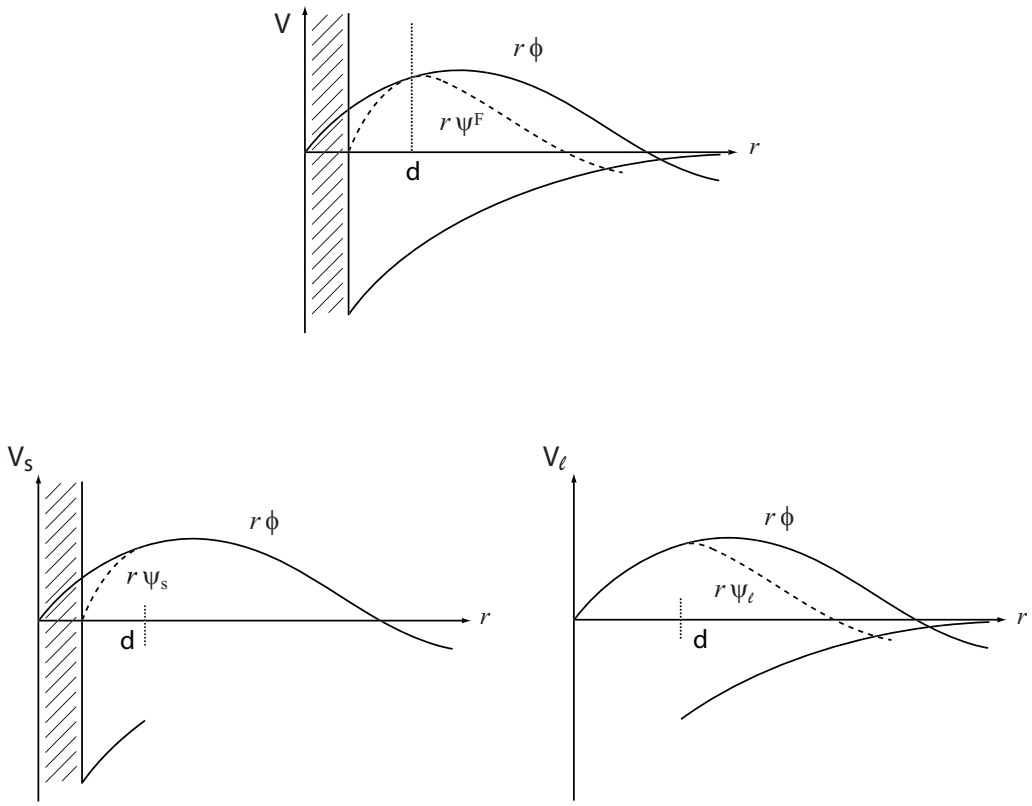

Figure 2.3: The top figure shows the comparison between the unperturbed relative wavefunction ϕ and the free-space perturbed wavefunction ψ^F, which are tangent at some distance d defining the separation of V into $V_s + V_l$. The bottom two figures show the free-space relative wavefunctions due to V_s and V_l alone and how they relate to ϕ and ψ^F.

We can approximate the full G-matrix as an expansion in V_s and V_l by performing the following mathematical manipulations. We begin by defining two scattering matrices

$$G = V + V\frac{Q}{e}G \tag{2.15}$$

and

$$T_s = V_s + V_s \frac{1}{e_0} T_s, \tag{2.16}$$

where the latter equation is the just the T-matrix equation for scattering in free space and e_0 is the free space energy. Introducing the wave operators Ω and Ω_s

$$\Omega = 1 + \frac{Q}{e} G \;\text{ and }\; \Omega_s = 1 + \frac{1}{e_0} T_s \tag{2.17}$$

one can show that

$$\begin{aligned} G &= T_s^\dagger + T_s^\dagger \left(\frac{Q}{e} - \frac{1}{e_0} \right) G + \Omega_s^\dagger \left(V - V_s \right) \Omega \\ &= T_s + V_l + T_s \frac{Q-1}{e} T_s + T_s \left(\frac{1}{e} - \frac{1}{e_0} \right) T_s \\ &\quad + T_s \frac{Q}{e} V_l + V_l \frac{Q}{e} T_s + V_l \frac{Q}{e} V_l + \cdots , \end{aligned} \tag{2.18}$$

where we have made the substitution $T_s^\dagger = T_s$. Note that if V_s is defined to give zero phase shift for free particle scattering, the corresponding T-matrix will be zero. Thus, to first-order in the above expansion we find the simple relation

$$G \simeq V_l. \tag{2.19}$$

In fact, the second-order terms are rather small compared to the first-order term as shown in [20]. Thus, it appears that under this separation of the NN interaction, to a good approximation one can model the full G-matrix with just the long distance part of the NN interaction.

2.4 Kallio-Kolltveit potential

In this section we apply the above methods to the Kallio-Kolltveit (KK) potential [59, 60] defined for relative S states as

$$V(r) = \frac{3 + \sigma_1 \cdot \sigma_2}{4} V_t(r) + \frac{1 - \sigma_1 \cdot \sigma_2}{4} V_s(r), \tag{2.20}$$

where

$$V_i(r) = \begin{cases} \infty & \text{for } r \leq 0.4 \text{ fm} \\ -A_i e^{-\alpha_i (r - 0.4)} & \text{for } r > 0.4 \text{ fm} \end{cases} \quad \text{for } i = s, t. \tag{2.21}$$

The four parameters were determined by fitting the scattering length and

effective range:

$$\begin{array}{ll} A_s = 330.8 \text{ MeV}, & \alpha_s = 2.4021 \text{ fm}^{-1} \\ A_t = 475.0 \text{ MeV}, & \alpha_t = 2.5214 \text{ fm}^{-1}. \end{array} \tag{2.22}$$

It is important to include the infinite hard core, known to schematize the vector meson exchange, in the effective potential. To compensate for this the potentials must be very attractive, as shown by A_s and A_t, so that the separation distance will change only slowly with incident energy. Applying the separation method to this potential yields singlet and triplet separation distances that vary slowly with the relative momentum [59], and for small momenta $d_s = 1.025$ fm and $d_t = 0.925$ fm.

2.5 Results and discussion

In order to directly compare the KK potential with $V_{\text{low}-\text{k}}$, it is convenient to transform the KK potential into k-space according to

$$V(k,k') = \frac{2}{\pi}\int_d^\infty r^2 j_0(kr) V_l j_0(k'r) dr, \tag{2.23}$$

Figures 2.4 and 2.5 compare the results of the Fourier transformation with $V_{\text{low}-\text{k}}$. Of course, since the KK potential fits only the scattering length and effective range, it should not be expected to agree precisely with $V_{\text{low}-\text{k}}$. Nevertheless, the agreement between the two appears generally good for the $^1S_0$ state but slightly worse for the $^3S_1$ state. It is not surprising that a local approximation is less good for the $^3S_1$ state than for the $^1S_0$ state, because a good fraction, $\sim 1/3$, of the $^3S_1$ attraction comes from the second order tensor interaction. The contributions peak quite sharply around intermediate states with momenta ~ 2 fm^{-1} [64], so a local approximation is quite good, but to be completely local the peak would have to be a δ-function.

We can gain some insight into the relationship between the low momentum decimation procedure and the separation method by examining the effects of varying the separation distance. Figure 2.6 shows how the k-space KK potential compares to $V_{\text{low}-\text{k}}$ for separation distances of 0.9 fm and 1.1 fm in the $^1S_0$ channel. It appears that for the $^1S_0$ state, a separation distance of ~ 1.0 fm produces the closest agreement with $V_{\text{low}-\text{k}}$. Figure 2.7 shows the effect of raising the separation distance of the $^3S_1$ state to 1.025 fm. The agreement with $V_{\text{low}-\text{k}}$ is notably better. We suggest that this is explained by the common scale in $V_{\text{low}-\text{k}}$.

The other question in comparison with $V_{\text{low}-\text{k}}$ is as to the momentum com-

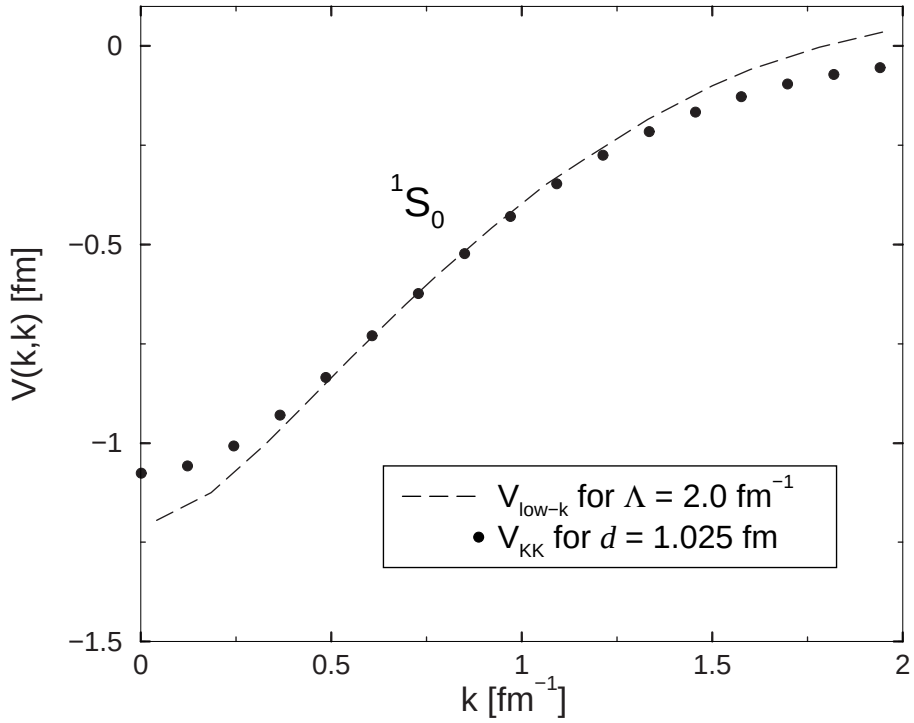

Figure 2.4: The $^1S_0$ diagonal matrix elements of $V_{\mathrm{low-k}}$ and the Kallio-Kolltveit potential for a configuration space cutoff of 1.025 fm.

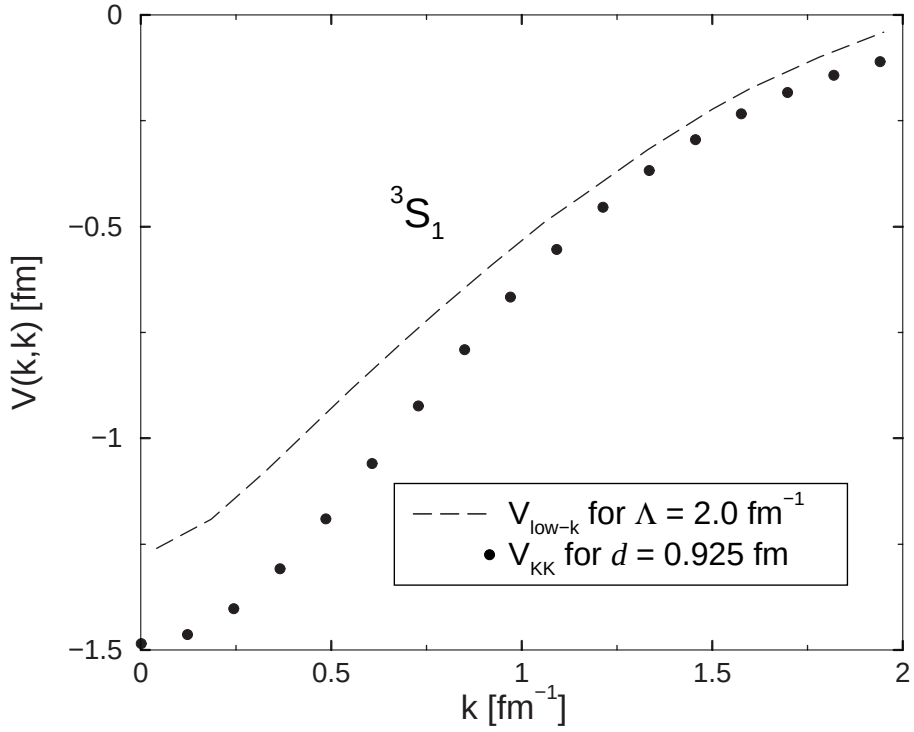

Figure 2.5: The $^3S_1$ diagonal matrix elements of $V_{\mathrm{low-k}}$ and the Kallio-Kolltveit potential for a configuration space cutoff of 0.925 fm.

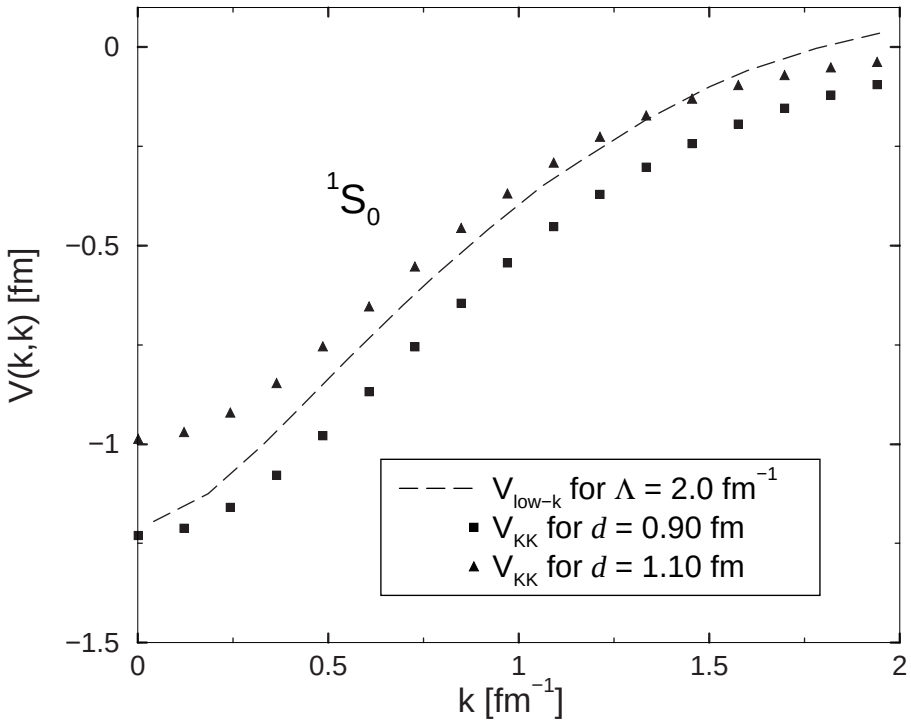

Figure 2.6: Variations of the $^1S_0$ partial wave matrix elements with the separation distance.

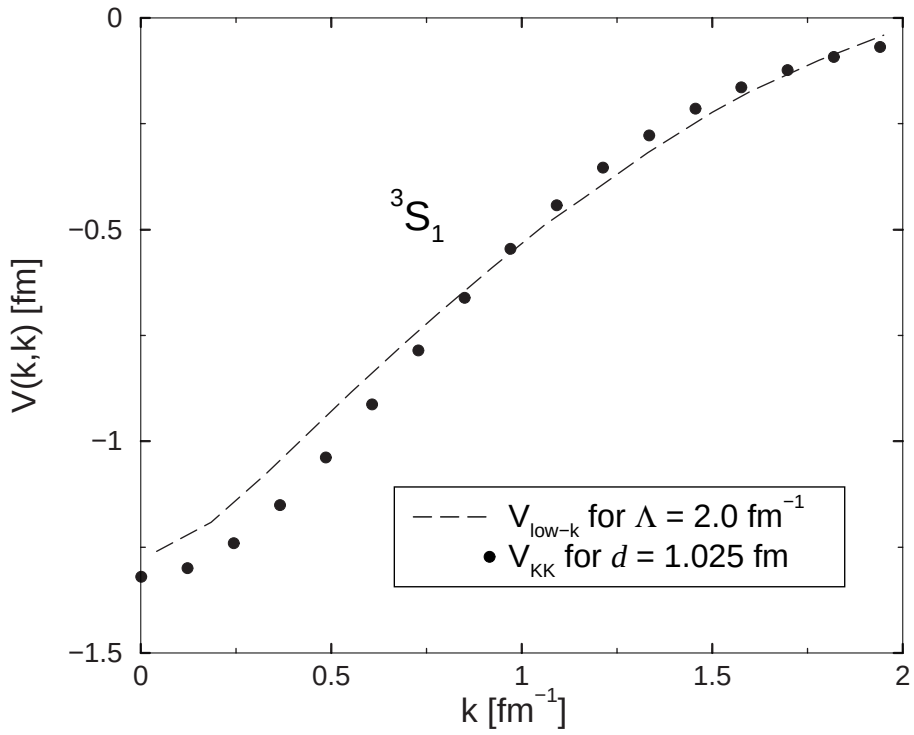

Figure 2.7: The $^3S_1$ diagonal matrix elements of $V_{\rm low-k}$ and the Kallio-Kolltveit potential for a configuration space cutoff of 1.025 fm.

ponents above $\Lambda = 2.0$ fm^{-1}, which are taken to be zero in $V_{\mathrm{low}-k}$ because they have not been measured experimentally. We show these momentum components for the KK potential in Figure 2.8. From Figure 2.8 we see that the diagonal matrix elements are very small for $k > \Lambda \sim 2$ fm^{-1}. Importantly, the sharp cutoff on the potential does not introduce appreciable artifacts.

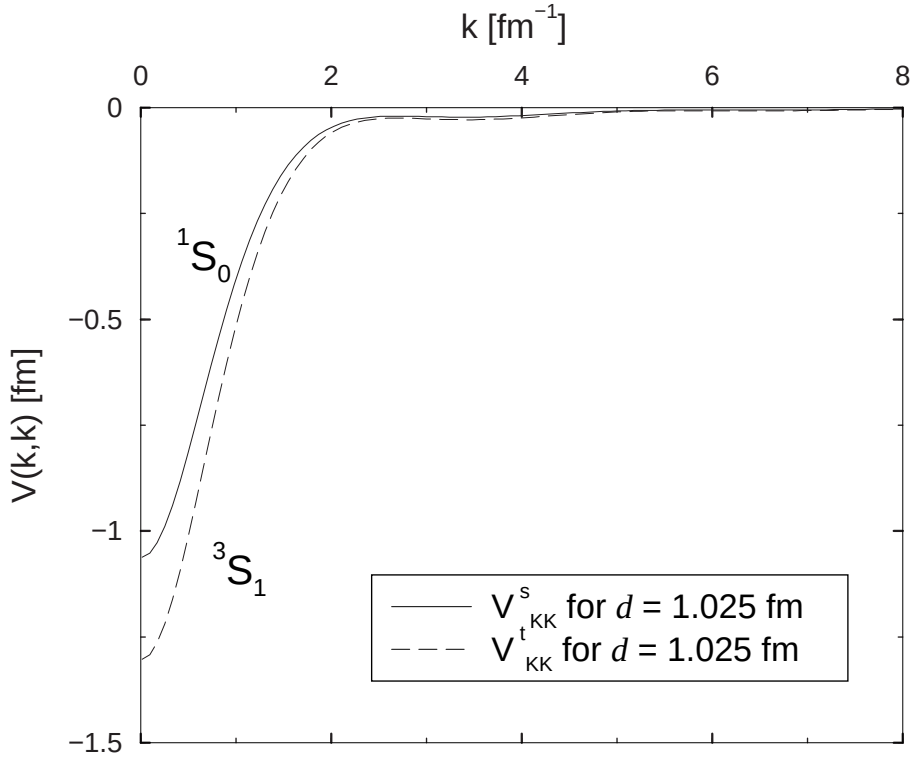

Figure 2.8: Diagonal matrix elements of the Kallio-Kolltveit potential, including momenta above the $V_{\mathrm{low-k}}$ cutoff of 2.0 fm^{-1}.

We thus note that the S-wave treatment of Kuo and Brown [62], modulo the small adjustment we made here to have equal cutoffs in singlet and triplet channels, using the MS separation method was equivalent to the low momentum decimation procedure which results in $V_{\mathrm{low-k}}$. Since model dependence in terms of high-momentum Fourier components above those accessed in the nucleon-nucleon scattering experiments will occur predominantly in the S-wave channels, this gives an answer to why the Kuo-Brown interactions have endured for 38 years; namely, to a large extent these model-dependent momenta were not present in the KB interaction.

These comparisons seem to suggest first that the low momentum decimation procedure and Moszkowski-Scott methods predict a similar separation of scales in the nuclear interaction, with closer agreement reached in the singlet

channel than in the triplet channel. However, the fact that close agreement between $V_{\mathrm{low-k}}$ and the KK potential is reached at a separation distance of 1.0 fm for both angular momentum states suggests that integrating out momenta beyond 2.0 fm^{-1} via the RG corresponds roughly to removing the short distance details below 1.0 fm in the singlet states.

We are not suggesting a replacement for $V_{\mathrm{low-k}}$, which has been astonishingly successful in nuclear structure calculations. But we do show that with S-wave potentials with the usual schematic hard core of conventional 0.4 fm radius, which fits the scattering length and effective range, we can get a good approximation, local in r, to $V_{\mathrm{low-k}}$ by choosing the separation distance correctly. It should be noted that the parameters in the KK potentials were chosen in order to get the scattering lengths and effective range correct. It thus appears that in addition to this some schematization of the short range repulsion is needed. With these minimal requirements one then has a good tool for nuclear structure physics. We suggest that these local potentials may be useful in schematic calculations where nuclear interactions have to be taken into account.

Our discussion here concerns only the G-matrix of Kuo and Brown [62], where we show the S-wave interactions to be essentially those of $V_{\mathrm{low-k}}$. The important remaining question which occupied research workers for many years was the validity of the polarization bubble that they used. We plan to show in a future publication [65] using the Babu-Brown formalism [66] which sums all planar particle-hole diagrams, that higher-order rescattering corrections reduce the strength of the bubble somewhat, especially at higher densities, but leave most of it. The higher-order corrections are only appreciable in the spin- and isospin-independent channels, affecting especially the compression modulus.

Chapter 3

Nuclear Matter Equation of State

3.1 Introduction

Understanding the equation of state (EOS) for nuclear matter is one of the most important goals in nuclear structure physics. The aim is to determine the ground state energy as a function of number density $n = A/V$ and neutron excess $\alpha = (n_n - n_p)/n$ for an infinite system of protons and neutrons interacting only through the strong force. At zero temperature this idealized system can provide a good model for both normal nuclear matter at the center of heavy nuclei as well as cold neutron stars with a large neutron excess. Empirical constraints on the EOS are available only for densities close to that of nuclear matter $n = n_0$ and proton fractions close to $x = 0.50$, though the development of new radioactive beam facilities studying neutron-rich nuclei will greatly increase our understanding of the low x region.

A great deal of effort has been devoted to computing the binding energy as a function of density starting from a microscopic many-body theory. For many years, Brueckner Hartree-Fock (BHF) theory [67–69] and variational methods [70, 71] have been the primary calculational tools for nuclear matter studies, though the BHF approach has proven to be generally more versatile in that it can accomodate any of the modern realistic NN interactions. Nevertheless, such calculations showed that it is very difficult to obtain both the saturation energy E_0/A and density n_0 satisfactorily with realistic two-body interactions alone. Plotting the saturation energy vs. density (E_0/A vs. n_0), the results of a number of such calculations actually lie on a band, often referred to as the Coester band [22, 23], all deviating significantly from the empirical values for the saturation energy and density of nuclear matter. As we shall discuss later,

the BHF method is a lowest-order G-matrix theory; it has several drawbacks which can be improved upon.

In the present work, we shall carry out calculations for symmetric and asymmetric nuclear matter using a framework based on a combination of the recently developed low-momentum NN interaction $V_{\mathrm{low}-k}$ [14, 15, 72–75] and the ring-diagram method for nuclear matter of Song *et.al.* [76]. This ring-diagram method is a model-space approach where the particle-particle hole-hole (*pphh*) ring diagrams for the potential energy of nuclear matter are summed to all orders. With a model space of size ~ 3 fm^{-1}, previous studies [76] obtained satisfactory results in both the binding energy per nucleon and the saturation momentum. Comparing with the BHF theory, the above ring-diagram approach has certain desirable features: the ground-state energy shift ΔE_0 in the BHF approach is given by the lowest-order reaction matrix (G-matrix) diagram (corresponding to diagram (b) of Fig. 3.2 with the dashed vertex representing G). It does not include diagrams corresponding to the particle-hole excitations of the Fermi sea. Such excitations represent the effect of long-range correlations. In contrast, the *pphh* ring diagrams, such as diagrams (c) and (d), are included to all orders in the ring-diagram approach. The single-particle (s.p.) spectrum used in the ring-diagram approach is also different from that traditionally used in BHF. In BHF theory one typically employs a self-consitent s.p. spectrum for momenta $k \leq k_F$ (the Fermi momentum), while for $k > k_F$ a free-particle spectrum is used. Thus the s.p. spectrum has a large artificial discontinuity at k_F. The s.p. spectrum used in the ring diagram approach is more desirable: for $k \leq \Lambda$, the boundary of the momentum model space, it employs a self-consistent s.p. spectrum while a free particle spectrum is used for $k > \Lambda$. Λ is generally considerably larger than k_F and the discontinuity of the s.p. spectrum at Λ is rather small [76].

The above ring-diagram approach [76] employed the G matrix interaction which is energy dependent. This energy dependence has largely complicated the ring diagram calculations, and it would be very helpful if this energy dependence were circumvented. In the past several years, there has been much progress in the renormalization group approach to the NN interaction, and a low-momentum NN interaction $V_{\mathrm{low}-k}$ has been developed [14, 15, 72–75]. As discussed in these references, this $V_{\mathrm{low}-k}$ interaction has a number of desirable properties, such as being nearly unique and being well behaved at short distances and thus convenient for calculations. Furthermore, $V_{\mathrm{low}-k}$ is energy independent, making it an "ideal" candidate for the interaction used in ring diagram calculations of nuclear matter.

The $V_{\mathrm{low}-k}$ interaction has been extensively used in nuclear shell-model calculations for nuclei with few valence nucleons outside a closed shell. As

reviewed recently by Coraggio *et al.* [77], the results obtained from such shell-model calculations are in very good agreement with experiments. However, applications of the $V_{\mathrm{low}-k}$ interaction to nuclear matter have been relatively few [78–81]. A main purpose of the present work is to study the suitability of describing symmetric nuclear matter using $V_{\mathrm{low}-k}$. A concern about such applications is that the use of $V_{\mathrm{low}-k}$ alone may not provide satifactory nuclear saturation. As illutrated in [78] and plotted in Fig. 3.1 below, Hartree-Fock calculations of nuclear matter using $V_{\mathrm{low}-k}$ do not yield nuclear saturation, the calculated E/A decreases monotonically with k_F up to the decimation scale Λ. Their calculations used $\Lambda \sim 2.0$ fm^{-1} for $V_{\mathrm{low}-k}$. The need for 3-body interactions for nuclear saturation has been extensively discussed in the literature (see Ref. [79] and references quoted therin). As we shall discuss, ring-diagram correlations at intermediate momentum ($k \sim 2.0$ fm^{-1}) have strong medium dependence and are important for saturation. To include their effect one needs to use a sufficiently large decimation scale Λ so that the above momentum region is not integrated out. Our results will indicate that satisfactory saturation can be attained by our present ring-diagram calculations using a decimation scale of $\Lambda \sim 3$ fm^{-1}.

3.2 Symmetric nuclear matter

In this section we describe how we calculate the properties of symmetric matter using the low-momentum ring diagram method based on a model-space approach [82]. We employ a momentum model space where all nucleons have momentum $k \leq \Lambda$. By integrating out the $k > \Lambda$ components, the low-momentum interaction $V_{\mathrm{low}-k}$ is obtained and used for calculating the *pphh* ring diagrams within the model space.

We shall calculate the all-order sum, denoted as ΔE_0^{pp}, of such diagrams. Each vertex in a ring diagram is the renormalized effective interaction $V_{\mathrm{low}-k}$ corresponding to the model space $k \simeq \Lambda$. As discussed in previous chapters, it is obtained from the following T-matrix equivalence equations

$$T(k', k, k^2) = V(k', k) + P \int_0^\infty q^2 dq \frac{V(k', q) T(q, k, k^2)}{k^2 - q^2}, \tag{3.1}$$

where V is a bare NN potential. Notice that in the above the intermediate state momentum q is integrated from 0 to ∞. We then define an effective

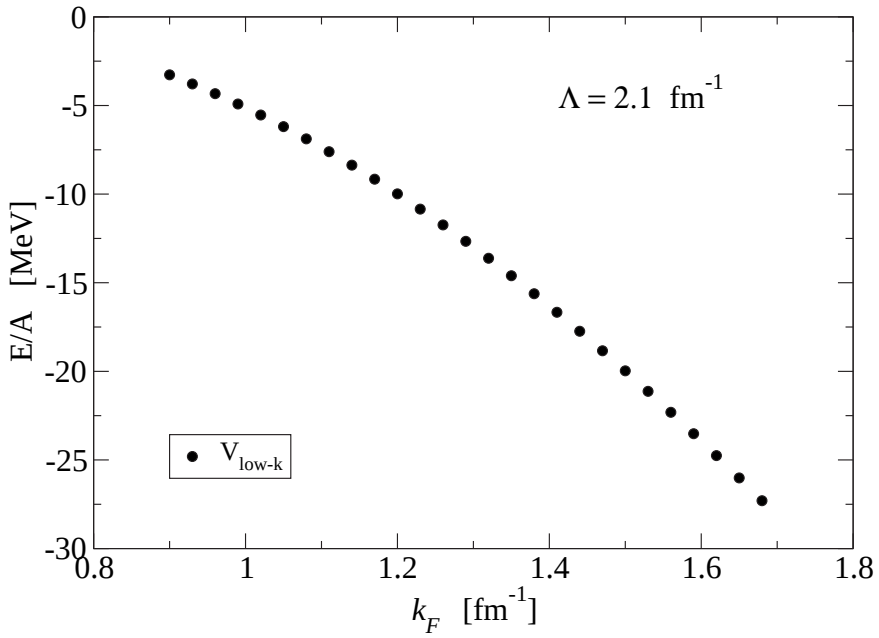

Figure 3.1: The ground state energy of symmetric nuclear matter calculated to lowest order in Hartree-Fock approximation with the low-momentum nucleon-nucleon interaction $V_{\mathrm{low}-k}$.

low-momentum T-matrix by

$$\begin{aligned} T_{\mathrm{low-k}}(p', p, p^2) &= V_{\mathrm{low-k}}(p', p) \\ &+ P \int_0^{\Lambda} q^2 dq \frac{V_{\mathrm{low-k}}(p', q) T_{\mathrm{low-k}}(q, p, p^2)}{p^2 - q^2}, \end{aligned} \tag{3.2}$$

where the intermediate state momentum is integrated from 0 to Λ, the momentum-space cut-off. $V_{\mathrm{low}-k}$ is then obtained from the above equations by requiring the the equivalence condition

$$T(p', p, p^2) = T_{\mathrm{low-k}}(p', p, p^2);\ (p', p) \leq \Lambda. \tag{3.3}$$

The iteration method of Lee-Suzuki-Andreozzi [18, 75, 83] has been used in calculating the above $V_{\mathrm{low}-k}$.

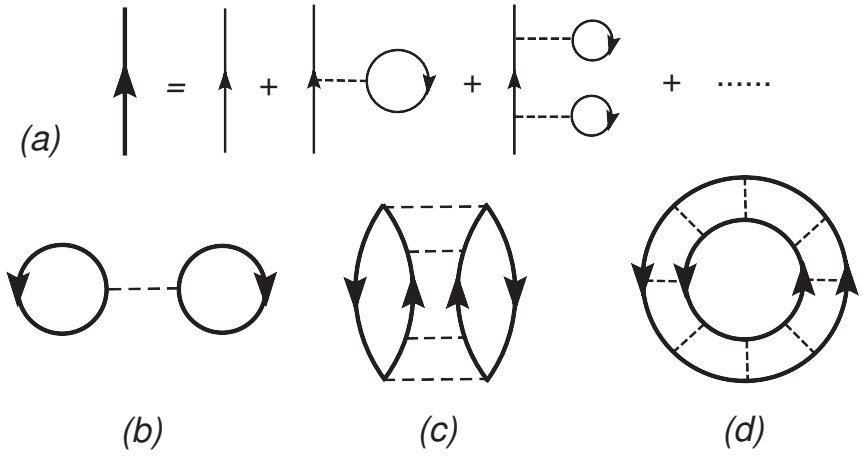

Figure 3.2: *pphh* ring-diagram summation in the calculation of the ground state energy shift.

With $V_{\mathrm{low}-k}$, our ring diagram calculations are relatively simple compared with previous studies [76] involving the G-matrix. The ground state energy shift ΔE_0 for nuclear matter, is defined as the difference $(E_0 - E_0^{free})$ where E_0 is the true ground-state energy and E_0^{free} is the corresponding quantity for the non-interacting system. In the present work, we consider ΔE_0 as given by the all-order sum of the *pphh* ring diagrams as shown by diagrams (b) to (d) of Fig. 3.2. The contribution from (b) to ΔE_0 is given by

$$\Delta E_0^{pp}(1) = \frac{-1}{2\pi i}\int_{-\infty}^{\infty} d\omega e^{i\omega 0^+} F_{ij}(\omega) V_{ijij}, \tag{3.4}$$

where F_{ij} is the unperturbed pair propagator

$$F_{ij}(\omega) = \frac{\bar{n}_i \bar{n}_j}{\omega - (\epsilon_i + \epsilon_j) + i0} - \frac{n_i n_j}{\omega - (\epsilon_i + \epsilon_j) - i0} \tag{3.5}$$

with $n_i = 1$ for $k_i < k_F$, $n_i = 0$ for $k_i > k_F$, and $\bar{n} = 1 - n$. Repeated indices are summed over and must lie within the model space, and the terms V_{inkl} are the antisymmetrized $V_{\mathrm{low}-k}$ matrix elements. Higher-order contributions to ΔE_0, such as diagrams (c) and (d) of Fig. 3.2, are defined similarly, and the total sum of *pphh* ring diagrams is given by

$$\Delta E_0^{pp} = \frac{-1}{2\pi i}\int_{-\infty}^{\infty} d\omega e^{i\omega 0^+} \mathrm{tr_P}\left(FV + \frac{1}{2}(FV)^2 + \frac{1}{3}(FV)^3 + \cdots\right), \tag{3.6}$$

where the trace $\mathrm{tr_P}$ denotes summation over repeated indices within the model space. This expression can be cast in the form of a geometric series by introducing the strength parameter λ as follows

$$\Delta E_0^{pp} = \frac{-1}{2\pi i}\int_0^1 \frac{d\lambda}{\lambda}\int_{-\infty}^{\infty} d\omega e^{i\omega 0^+}\mathrm{tr_P}\left(\lambda FV + (\lambda FV)^2 + (\lambda FV)^3 + \cdots\right). \tag{3.7}$$

For actual calculations it is convenient to define a λ-dependent Green function

$$G^{pp}_{ijkl}(\omega,\lambda) = F_{ij}(\omega)\delta_{ij,kl} + F_{ij}(\omega)\lambda V_{ijmn}G^{pp}_{mnkl}(\omega,\lambda), \tag{3.8}$$

which allows us to rewrite the ground state energy shift as

$$\Delta E_0^{pp} = \frac{-1}{2\pi i}\int_0^1 \frac{d\lambda}{\lambda}\int_{-\infty}^{\infty} d\omega e^{i\omega 0^+}\mathrm{tr_P}\left(G^{pp}(\omega,\lambda)V\lambda\right). \tag{3.9}$$

The advantage is that we can use the Lehmann representation of G^{pp}

$$G^{pp}_{ijkl}(\omega,\lambda) = \sum_n \frac{X_n(ij,\lambda)X_n^*(kl,\lambda)}{\omega - \omega_n^+(\lambda) + i0} - \sum_m \frac{Y_m(ij,\lambda)Y_m^*(kl,\lambda)}{\omega - \omega_m^-(\lambda) - i0}, \tag{3.10}$$

where

$$\begin{aligned}
\omega_n^+(\lambda) &= E_n^{A+2}(\lambda) - E_0^A(\lambda),\\
\omega_m^-(\lambda) &= E_0^A(\lambda) - E_m^{A-2}(\lambda),\\
X_n(ij,\lambda) &= \langle\Psi_0^A(\lambda)|a_j a_i|\Psi_n^{A+2}(\lambda)\rangle,\\
Y_m(ij,\lambda) &= \langle\Psi_m^{A-2}(\lambda)|a_j a_i|\Psi_0^A(\lambda)\rangle.
\end{aligned} \tag{3.11}$$

The λ-dependent eigenfunctions and eigenvalues are defined by

$$(H_0 + \lambda H_1)\Psi_0^A(\lambda) = E_0^A(\lambda)\Psi_0^A(\lambda), \text{etc.} \tag{3.12}$$

Finally, the substitution of Eq. (3.10) into Eq. (3.9) yields

$$\Delta E_0^{pp} = \int_0^1 \frac{d\lambda}{\lambda}\sum_m \sum_{ijkl<\Lambda} Y_m(ij,\lambda)Y_m^*(kl,\lambda)\lambda V_{ijkl}. \tag{3.13}$$

The amplitudes Y_m are computed from the model space RPA equation

$$\begin{aligned}
&\sum_{ef}[(\epsilon_i+\epsilon_j)\delta_{ij,ef} + \lambda(\bar{n}_i\bar{n}_j - n_i n_j)\langle ij|V_{low-k}|ef\rangle]\\
&\times Y_n(ef,\lambda) = \omega_n Y_n(ij,\lambda); \quad (i,j,e,f) \le \Lambda,
\end{aligned} \tag{3.14}$$

where the normalization condition for Y_m is $\langle Y_m|\frac{1}{Q}|Y_m\rangle = -1$ and $Q(i,j) = (\bar{n}_i\bar{n}_j - n_i n_j)$. In Eq. (3.13), Σ_m means we sum over only those solutions of the RPA equation (3.14) which are dominated by hole-hole components as indicated by the normalization condition. We use the Hartree-Fock s.p. spectrum given by $V_{\text{low}-k}$ within the model space and free particle spectrum beyond. Namely

$$\begin{aligned} \epsilon_k &= \hbar^2k^2/2m + \sum_{h<k_F}\langle kh|V_{low-k}|kh\rangle; \quad k \leq \Lambda, \\ &= \hbar^2k^2/2m; \quad k > \Lambda. \end{aligned} \tag{3.15}$$

The above s.p. spectrum is medium (k_F) dependent.

The all-order sum of the *pphh* ring diagrams as indicated by diagrams (b-d) of Fig. 3.2 is given by the above ΔE_0^{pp}. Since we use the HF s.p. spectrum, each propagator of the diagrams contains the HF insertions to all orders as indicated by part (a) of the figure. Clearly our ring diagrams are medium dependent; their s.p. propagators have all-order HF insertions which are medium dependent, and so is the occupation factor $(\bar{n}_i\bar{n}_j - n_i n_j)$ of the RPA equation.

3.2.1 Single-particle spectrum and nuclear binding energy

With this framework at hand we calculate first the single-particle spectrum of low momentum interactions for various values of the model space cutoff Λ. Within the model space approach, ϵ_k is given by the Hartree-Fock spectrum for $k \leq \Lambda$ and for $k > \Lambda$ it is taken as the free kinetic energy. As emphasized before, the single-particle spectrum defined in this way will in general have a discontinuity at the boundary of the model space. In Fig. 3.3 we plot the s.p. spectrum for various values of Λ ranging from 2.0 fm^{-1} to 4.0 fm^{-1}. For a model space cutoff of 2.0 fm^{-1} or 4.0 fm^{-1}, the resulting gap in the s.p. spectrum is rather large. However, for cutoffs between 2.5 and 3.0 fm^{-1} the s.p. spectrum is nearly continuous and therefore physically reasonable. For this reason, in our subsequent calculations we shall employ a cutoff within this desirable range.

We next consider the effect of Λ on the nuclear binding energy. Once the s.p. energies are obtained, the all-order ring diagram calculation can be performed. We choose the CD-Bonn potential to study the role of varying the cutoff around the physically reasonable cutoff range discussed above. The results are plotted in Fig. 3.4. We see that the results in general agree with calculations from the traditional hole-line expansion and variational methods,

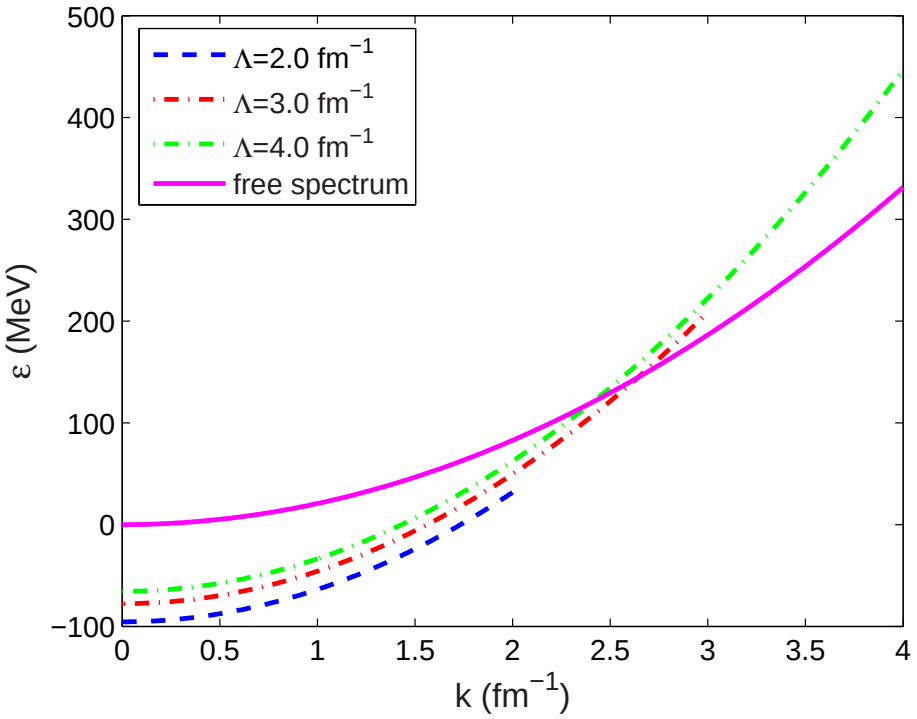

Figure 3.3: Dependence of the model-space s.p. spectrum on the decimation scale Λ. Shown are the results for low-momentum CD-Bonn potentials for different values of Λ.

which both yield saturation at too high a density for realistic NN interactions. As we have stated before, previous attempts to correct this deficiency have centered around the introduction of three-body forces. However, in this work our aim is to determine whether or not medium-modified nuclear interactions inspired by Brown-Rho scaling (BRS) can provide a suitable alternative to 3NF.

We study such density-dependent effects in two models. The first is the medium-modified Bonn-B potential of [84]. In this study dropping meson masses were incorporated into the Bonn-B potential and found to have a beneficial effect on the saturation properties of nuclear matter within the Dirac-Brueckner-Hartree-Fock formalism. This interaction treats scalar meson exchange microscopically by replacing the σ boson in the Bonn-B potential with a pair of correlated pions with $I = T = 0$. Further details can be found in Chapter 6. We also use the Brown-Rho-scaled Nijmegen I potential, which has contributions from the ρ, ω, and ϕ vector mesons as well as partial-wave-

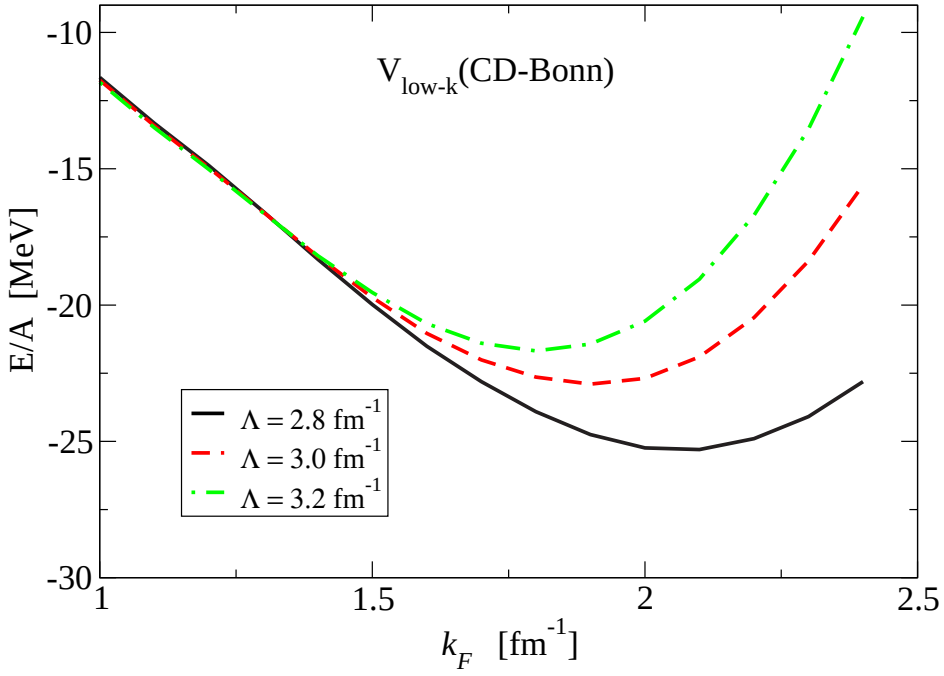

Figure 3.4: Ring diagram summation for the low momentum CD-Bonn interaction for different values of the model space cutoff Λ.

dependent σ mesons. We decrease the light vector mesons according to

$$\frac{m^*_{\rho,\omega}}{m_{\rho,\omega}} = 1 - C_{\rho,\omega}\frac{n}{n_0}, \tag{3.16}$$

where we take $C_{\rho,\omega} = 0.14$ in agreement with recent experimental results [53]. The heavy vector meson ϕ is composed of a strange quark and antiquark pair and therefore should not be scaled as the light vector mesons. In this work we choose to scale ϕ according to (3.16) except with $C_\phi = \frac{1}{2}C_{\rho,\omega}$. Similarly, the σ mesons are scaled again by half that of the vector mesons since it has been shown [84] that when the σ meson is treated microscopically as 2π exchange, the effective scaling is significantly weaker than that proposed in the original BRS scenario.

In Fig. 3.6 we plot the ground state energy for symmetric nuclear matter

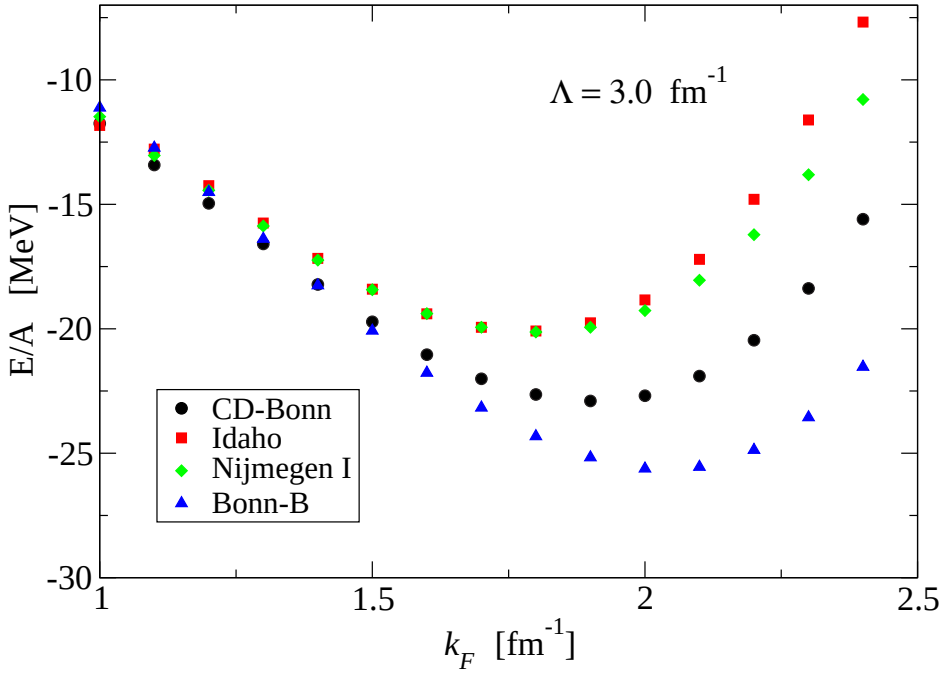

Figure 3.5: Results of the ring diagram summation for nuclear matter calculated from several realistic NN interactions with $\Lambda = 3.0$ fm^{-1}.

calculated from the two medium-modified interactions described above. The main effect is a significant lowering of the saturation density. The large decrease in the ω meson mass together with a weakening of the second-order tensor force, which plays a large role in nuclear binding, give the most important contributions to this effect. Although both interactions produce a binding that is still too weak compared to experiment, it is interesting to observe that our results compare well with those of Bogner *et al.* [79], who included the leading-order chiral 3N interaction together with $V_{\mathrm{low}-k}$. In particular, both methods lead to saturation at the correct density but with too little binding. The compression modulus, defined by

$$\mathcal{K} = \left(k_F^2 \frac{d^2 E}{dk_F^2} \right)_{k_{F_0}} \tag{3.17}$$

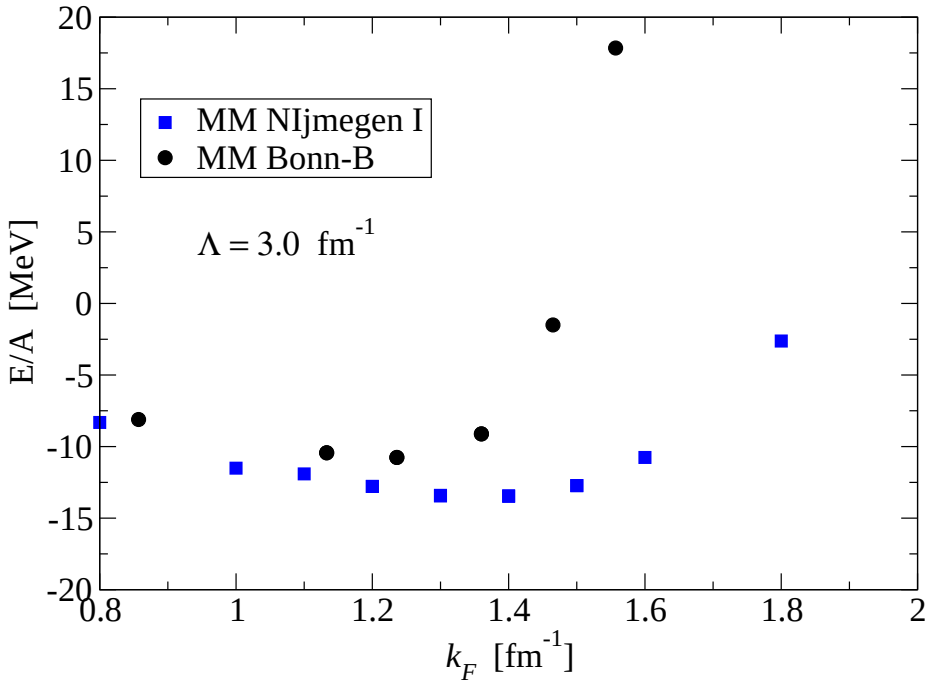

Figure 3.6: Ground state energy of symmetric nuclear matter calculated with the ring diagram partial summation for the medium-modified (MM) Nijmegen I potential and Bonn-B potential.

is known experimentally to be $200 - 300$ MeV [85, 86]. Given our two models we extract values of

$$\begin{aligned} \mathcal{K}_{\text{Nijmegen}} &= 130 \text{ MeV} \\ \mathcal{K}_{\text{Bonn}-\text{B}} &= 210 \text{ MeV}. \end{aligned} \tag{3.18}$$

3.3 Asymmetric nuclear matter

Understanding the structure of neutron stars requires the nuclear matter EOS at high densities and at various values of the proton fraction x (see Ref. [87] for detailed discussion of the neutron star equation of state). Since two-nucleon interactions alone have proven unable to produce the correct saturation energy

and density of symmetric nuclear matter, three-body forces have been used in the past to remedy this problem. However, modeling high density nuclear matter is a significant challenge, for the EOS is highly sensitive to the three-body force used. In this work we choose to study the effects of Brown-Rho scaling on the neutron star EOS. This provides a simpler approach than introducing three-body forces, but we suggest that the two methods can capture the effects of degrees of freedom that are missing in the construction the two-body part of the interaction.

For asymmetric nuclear matter we define the neutron excess as $\alpha = (n_n - n_p)/n$, where n_n, n_p, and n are the neutron, proton, and total nuclear number density respectively. There are then two Fermi surfaces for the two species of nucleons defined by

$$\begin{aligned} k_f^p &= (3\pi^2 n_p)^{1/3} \\ k_f^n &= (3\pi^2 n_n)^{1/3}. \end{aligned} \tag{3.19}$$

The binding energy as a function of density and neutron excess is given by

$$\frac{E}{A}(n,\alpha) = \frac{E}{A}(n,0) + \frac{\Delta E_{\rm kin}}{A}(n,\alpha) + \frac{\Delta E_{\rm pot}}{A}(n,\alpha), \tag{3.20}$$

where the first term is the binding energy of symmetric nuclear matter and the next two terms represent deviations due to isospin asymmetry from the kinetic energy and potential energy respectively. From Eq. (3.19) the isospin asymmetric kinetic energy term can be written

$$\frac{\Delta E_{\rm kin}}{A}(n,\alpha) = \frac{3}{5}\frac{\hbar^2}{2m}(3\pi n/2)^{2/3}\frac{1}{2}\left[(1+\alpha)^{5/3} + (1-\alpha)^{5/3} - 2\right]. \tag{3.21}$$

It is useful to expand this expression in powers of α^2

$$\frac{\Delta E_{\rm kin}}{A}(n,\alpha) = \frac{1}{3}\frac{\hbar^2}{2m}(3\pi n/2)^{2/3}\alpha^2\left(1 + \frac{\alpha^2}{27} + \cdots\right). \tag{3.22}$$

For the potential energy correction in Eq. (3.20) it turns out to be a good approximation to expand in powers of α^2 as well, which we will see from explicit calculations below. Therefore, we introduce the terms $S_2, S_4, \ldots$ and separate the energy per nucleon into density-dependent and isospin asymmetry-dependent components

$$\frac{E}{A}(n,\alpha) = \frac{E}{A}(n,0) + S_2(n)\alpha^2 + S_4(n)\alpha^4 + \cdots. \tag{3.23}$$

Note that the dependence on nuclear density and isospin asymmetry have been separated. It is usually sufficient to keep only the quadratic term in α. We will now discuss how to calculate the terms S_i in our ring diagram formalism.

For asymmetric nuclear matter one must distinguish between protons and neutrons. The model space is chosen to be independent of nucleon species, that is, $\Lambda_n = \Lambda_p = \Lambda$. Single-particle energies within the model space are defined as

$$\epsilon_i = \hbar^2 k_i^2/2m + U(k_i, \tau_i) \tag{3.24}$$

where the subscript i stands for the momentum, spin, and isospin of the i^{th} nucleon and the single particle potential $U(k_i, \tau_i)$ is given by

$$U(k_i, \tau_i) = \frac{1}{2} \sum_{\tau_j, s_i, s_j, k_j < k_F^{\tau_j}} \langle kh|V_{low-k}|kh\rangle; \quad k_i \leq \Lambda, \tag{3.25}$$

where i represents both momentum and isospin. We can derive analogous expression to Eqs. (3.13) and (3.14) above except that in the summations one must be careful to distinguish protons and neutrons since they have different single particle energies. Thus, by varying the neutron excess α to give different Fermi momenta for protons and neutrons, the above formalism can be used to determine the equation of state as a function of density and neutron excess. In Fig. 3.7 we show for comparison the equation of state for symmetric nuclear matter and pure neutron matter calculated from the medium-modified Bonn-B potential of [84].

3.4 Neutron star equation of state

Neutron stars are born with temperatures on the order of tens of MeV, but they cool very quickly by neutrino emission to a temperature of less than 1 MeV. Typically this process takes on the order of minutes. Therefore, it is a good approximation to treat neutron stars as zero temperature nuclear matter. The ground state is determined by enforcing charge neutrality and beta chemical equilibrium. We assume that the matter is composed of only protons, neutrons, and electrons, so that exotic forms of matter (such as strange particles) are neglected and neutrinos are assumed to leave the system immmediately upon production.

The two reactions which continually take place in neutron stars are

$$n \rightarrow p + e^- + \bar{\nu}_e \quad \text{and} \quad p + e^- \rightarrow n + \nu_e. \tag{3.26}$$

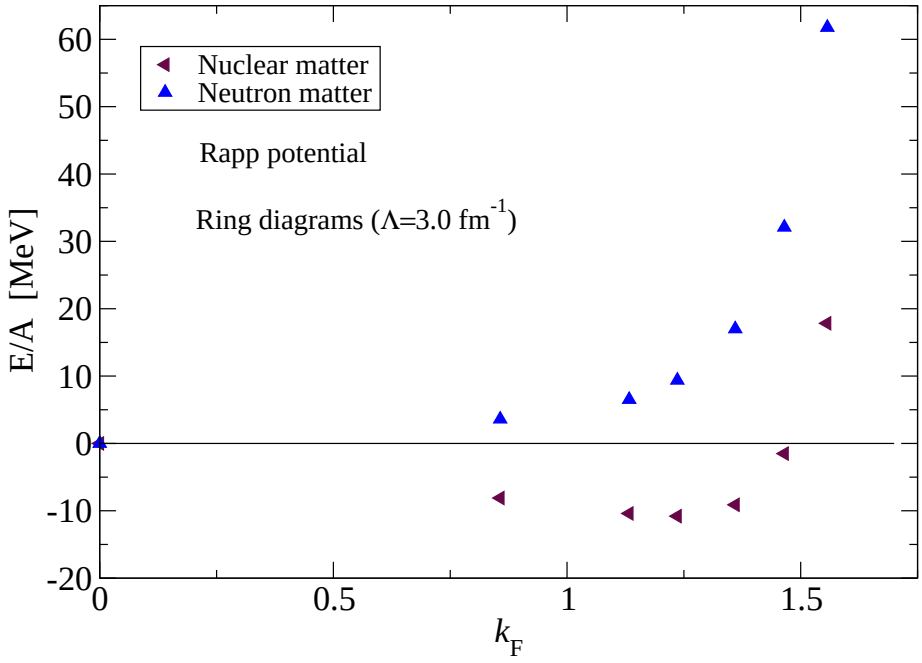

Figure 3.7: The ground state energy as a function of Fermi momentum for the medium-modified Bonn-B potential in both symmetric nuclear matter and pure neutron matter.

Then chemical equilibrium implies

$$\mu_n - \mu_p = \mu_e. \tag{3.27}$$

The proton and neutron chemical potentials are defined as

$$\mu_p = \left.\frac{\partial \epsilon}{\partial n_p}\right|_{n_n} \tag{3.28}$$

and

$$\mu_n = \left.\frac{\partial \epsilon}{\partial n_n}\right|_{n_p}, \tag{3.29}$$

where ϵ is the total energy inclusive of rest mass. The difference between the

two chemical potentials can be written in the convenient form

$$\mu_n - \mu_p = -\frac{\partial E}{\partial x}, \tag{3.30}$$

where x is the proton fraction $x = (1-\alpha)/2$. Combining Eqs. (3.23) and (3.30), we find

$$\mu_e = \mu_n - \mu_p = 4\alpha(S_2(n) + 2S_4(n)\alpha^2 + \cdots). \tag{3.31}$$

Charge neutrality implies that $k_F^e = k_F^p$, and assuming that the electrons are relativistic, one can rewrite Eq. (3.31) as

$$4\alpha(S_2(n) + 2S_4(n)\alpha^2 + \cdots) = \hbar c \left(3\pi^2 n \frac{1-\alpha}{2}\right)^{1/3}. \tag{3.32}$$

Thus, once we determine the symmetry energy terms $S_2(n)$, $S_4(n)$, etc. we can determine the neutron excess as a function of the nuclear density.

The symmetry energy is easily calculated from our ring diagram summation for asymmetric nuclear matter. We show in Fig. 3.8 the system energy as a function of neutron excess for densitites up to n_0. We have fit the calculated energies with the function

$$\frac{E}{A}(n,\alpha) = \frac{E}{A}(n,0) + S_2(n)\alpha^2. \tag{3.33}$$

from which we extract the symmetry energy term S_2 as a function of density. We note that the quadratic approximation provides a very good fit to the calculated energies. The results for S_2 are shown in Fig. 3.9. The symmetry energy at nuclear matter density is known to be $25-35$ MeV [86, 88]. Our result of 21.1 MeV is slightly below this value but in good agreement with the value obtained in the context of Fermi liquid theory in Chapter 4. Neglecting terms higher than S_2 in Eq. (3.32), we find a simple equation determining the equilibrium neutron excess as a function of the density:

$$4\alpha S_2(n) = \hbar c \left(3\pi^2 n \frac{1-\alpha}{2}\right)^{1/3}. \tag{3.34}$$

We show in Fig. 3.10 the electron chemical potential as function of density up to $1.5n_0$. The electron chemical potential is important not only for determining the equation of state for cold, catalyzed neutron star matter, but it also plays a role in determining the onset of kaon condensation [89]. We solve Eq. (3.32) to linear order in α^2 and plot the resulting proton fraction $x = (1-\alpha/2)$ in

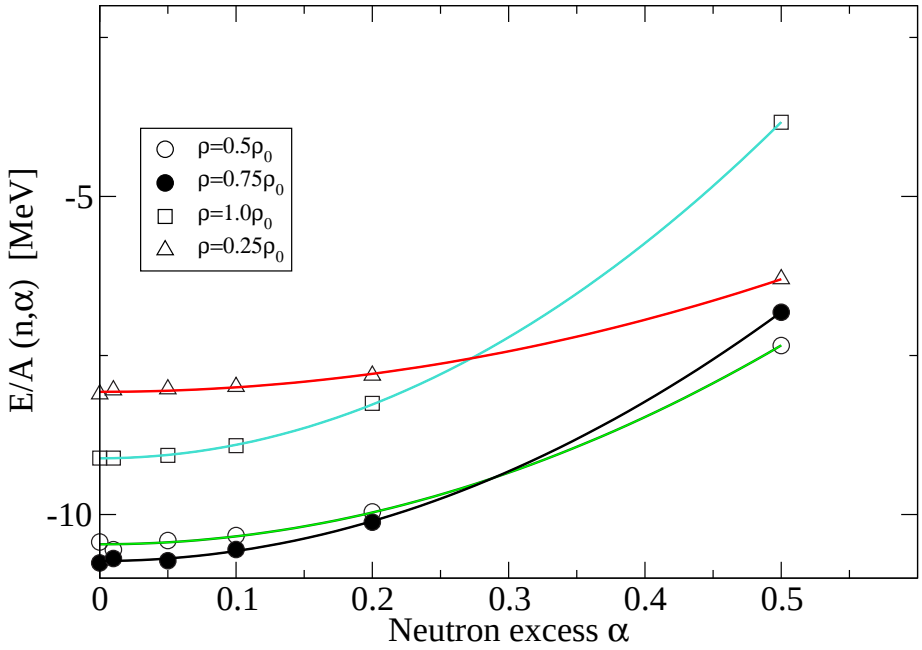

Figure 3.8: The energy per nucleon of asymmetric nuclear matter as a function of neutron excess α from which one can extract the lowest-order symmetry energy term S_2. Each curve corresponds to a different value of the nuclear density.

Fig. 3.11. Finally, we show in Fig. 3.12 the equation of state for symmetric nuclear matter, pure neutron matter, and cold catalyzed neutron star matter up to a density of $n = 1.5n_0$.

3.5 Conclusions

We have seen how Brown-Rho-scaled NN interactions, when used in the ring diagram partial summation for calculating nuclear binding energies, can significantly improve the saturation density for nuclear matter. The binding energy remains slightly weak, though this is in agreement with previous calculations using low momentum interactions supplemented with 3NF. In the Walecka model of nuclear matter, the binding energy results from a cancellation between the large attractive scalar field σ and the large repulsive vector field ω.

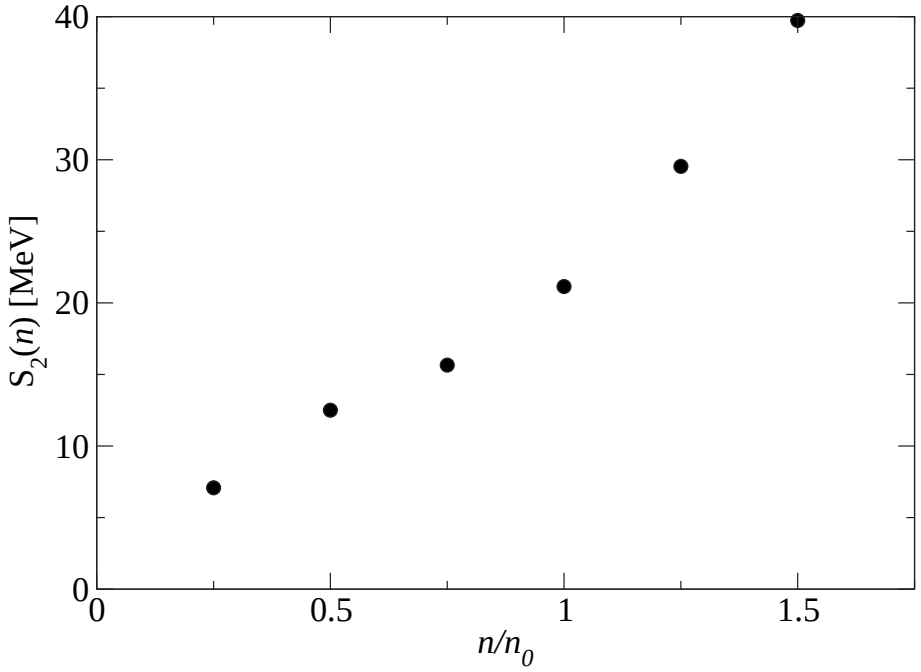

Figure 3.9: Symmetry energy S_2 as a function of the nuclear density for the medium-modified Bonn-B potential.

Obtaining the saturation energy is therefore a fine-tuning problem, which will be sensitive to how BRS is implemented. Nevertheless, we have found that the main effect is a lowering of the saturation density to its correct value.

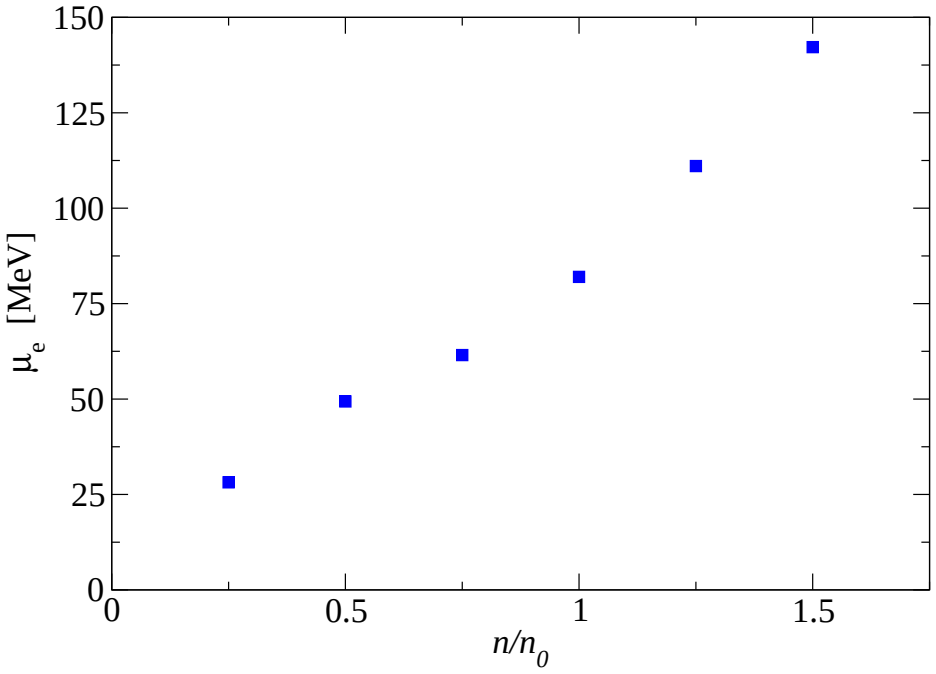

Figure 3.10: Electron chemical potential obtained from the symmetry energy S_2 by imposing charge neutrality and beta equilibrium. The results are plotted as a function of the nuclear density for the medium-modified Bonn-B potential.

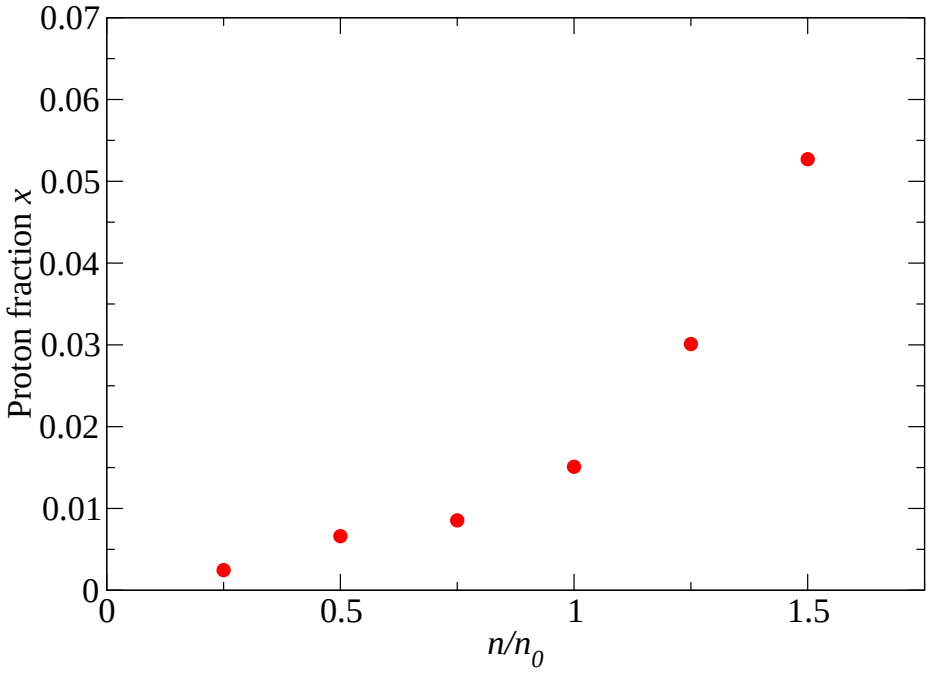

Figure 3.11: Proton fraction obtained by solving Eq. (3.34) using the values of the electon chemical potential shown in Fig. 3.10.

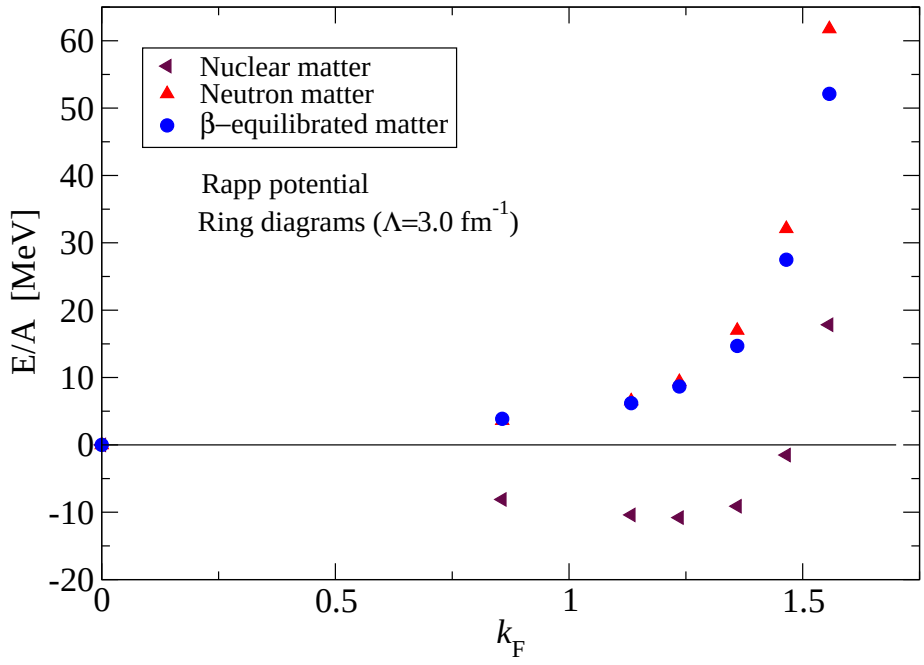

Figure 3.12: Equation of state for cold, catalyzed neutron star matter calculated from the Bonn-B potential with Brown-Rho scaling medium modifications. For comparison we also show the equation of state for symmetric nuclear matter and pure neutron matter.

Chapter 4

Fermi Liquid Theory and Brown-Rho-Scaled NN Interactions

4.1 Introduction

Landau's theory of normal Fermi liquids [90–92] describes strongly interacting many-body systems in terms of weakly interacting quasiparticles. Provided that the quasiparticles lie sufficiently close to the Fermi surface, they will be long-lived and constitute appropriate degrees of freedom for the system. The central aim of the theory is to determine the quasiparticle interaction, either phenomenologically or microscopically, with which it is possible to describe the low-energy, long-wavelength excitations of the system. This, in turn, is sufficient for the description of many bulk equilibrium properties of the interacting Fermi system. The initial application of Fermi liquid theory to nuclear physics was the phenomenological description of finite nuclei and nuclear matter by Migdal [93, 94], and later a microscopic approach to Fermi liquid theory based on the Brueckner-Bethe-Goldstone reaction matrix theory was developed by Bäckman [95, 96] and others [97, 98] to describe nuclear matter. Although the latter approach was quantitatively successful, it was observed [98] that Brueckner-Bethe-Goldstone theory is less reliable in the vicinity of the Fermi surface due to the use of angle-averaged Pauli operators and the unsymmetrical treatment of particle and hole self energies, which leads to an unphysical energy gap at the Fermi surface.

With the recent development of a nearly universal low-momentum nucleon-nucleon (NN) interaction $V_{\mathrm{low}-k}$ [14] derived from renormalization group methods, the application of Fermi liquid theory to nuclear matter has received

renewed attention [74, 99, 100]. The strong short-distance repulsion incorporated into all high-precision NN potential models is integrated out in low momentum interactions, rendering them suitable for perturbation theory calculations. Although limited Brueckner-Hartree-Fock studies [101] indicate that saturation is not achieved with $V_{\mathrm{low}-k}$ at a fixed momentum cutoff Λ, it has recently been shown [79] that by supplementing $V_{\mathrm{low}-k}$ with the leading-order chiral three-nucleon force, nuclear matter does saturate, thereby justifying the use of $V_{\mathrm{low}-k}$ in studies of nuclear matter.

Although many properties of the interacting ground state are beyond the scope of Fermi liquid theory, the quasiparticle interaction is directly related to several nuclear observables, including the compression modulus, symmetry energy, and anomalous orbital gyromagnetic ratio. As originally shown by Landau, the quasiparticle interaction is obtained from a certain limit of the four-point vertex function in the particle-hole channel. It is well known that using realistic NN interactions in the lowest order approximation to the quasiparticle interaction is insufficient to stabilize nuclear matter, as evidenced by a negative value of the compression modulus. This general phenomenon is observed in our calculations with $V_{\mathrm{low}-k}$ as well. However, stability is achieved by treating the exchange of density, spin, and isospin collective excitations to all orders in perturbation theory. The inclusion of these virtual collective modes in the quasiparticle interaction is carried out through the induced interaction formalism of Babu and Brown [66], which was originally developed for the description of liquid ^{3}He and later applied to nuclear matter by Sjöberg [102, 103]. Subsequent work [104, 105] has confirmed the importance of the induced interaction in building up correlations around a single quasiparticle, thereby increasing the compression modulus.

Our study is motivated in part by the work of Schwenk *et al.* [74], who were able to predict the spin-dependent parameters of the quasiparticle interaction from the experimentally extracted spin-independent parameters. Crucial to these calculations was a novel set of sum rules, derived from the induced interaction formalism, based on a similar treatment by Bedell and Ainsworth [106] to liquid ^{3}He. In this paper we present a fully self-consistent solution to the Babu-Brown induced interaction equations for symmetric nuclear matter. Our iterative solution turns out to be qualitatively similar to the results of [74], but we find that at nuclear matter density the compression modulus and symmetry energy are smaller than the experimentally observed values while the anomalous orbital gyromagnetic ratio is too large, suggesting the possibility that important phenomena have been neglected.

We propose to extend this study by including hadronic modifications associated with the partial restoration of chiral symmetry at nuclear matter

density, as suggested in [45]. In this scenario, referred to as Brown-Rho scaling, the dynamically generated hadronic masses drop in the approach to chiral restoration, and at nuclear matter density it is expected that the masses of the light hadrons (other than the masses of the pseudoscalar mesons, which are protected by their Goldstone nature) decrease by approximately 20%. The success of one-boson-exchange and chiral EFT potentials in describing the nucleon-nucleon interaction suggests that a modification of meson masses in medium ought to have verifiable consequences in low energy nuclear physics. Although there is much current theoretical and experimental effort devoted to the program of assessing these medium modifications, the consequences for low-energy nuclear physics have yet to be fully explored.

Applying the mass scaling suggested in [45] to our calculations of nuclear matter, we obtain a set of Fermi liquid coefficients in better agreement with both experiment and the nontrivial sum rules derived in [74]. Explicit three-body forces, though essential for a complete description of nuclear matter, have been neglected in this study. However, we argue that modifying the vector meson masses is equivalent to including a specific short-ranged three-body force. We conclude with a discussion of the consequences of Brown-Rho scaling on the tensor force, which is diminished by the increasing strength of ρ-meson exchange.

4.2 Fermi liquid theory

In this section we present a short description of Fermi liquid theory and its application to nuclear physics with emphasis on the microscopic foundation of the theory. The main assumption underlying Landau's description of many-body Fermi systems is that there is a one-to-one correspondence between states of the ideal system and states of the interacting system. As one gradually turns on the interaction, the noninteracting particles become "dressed" through interactions with the many-body medium and evolve into weakly interacting quasiparticles. The interacting system is in many ways similar to an ideal system in that the classification of energy states remains unchanged and there is a well-defined Fermi surface, but the quasiparticles acquire an effective mass m^* and finite lifetimes $\tau \sim (k - k_F)^{-2}$. The energy of the interacting system is a complicated functional of the quasiparticle distribution function, and in general the exact dependence is inaccessible. But one can extract important information about bulk properties of the system by considering small changes

in the distribution function. Expanding to second order, one finds

$$\delta E = \sum_{\mathbf{k}_1} \epsilon^{(0)}_{\mathbf{k}_1} \delta n(\mathbf{k}_1) + \frac{1}{2\Omega} \sum_{\mathbf{k}_1,\mathbf{k}_2} f(\mathbf{k}_1,\mathbf{k}_2)\delta n(\mathbf{k}_1)\delta n(\mathbf{k}_2) + \mathcal{O}(\delta n^3). \tag{4.1}$$

In this equation Ω is the volume of the system, $\epsilon^{(0)}_{\mathbf{k}_1}$ is the energy added to the system by introducing a single quasiparticle with momentum $\mathbf{k}_1$ (note that for $|\mathbf{k}_1| \equiv k_1 = k_F$, $\epsilon^{(0)}_{\mathbf{k}_1}$ is just the chemical potential), and $f(\mathbf{k}_1,\mathbf{k}_2)$ describes the interaction between two quasiparticles.

Since the quasiparticle interaction $f(\mathbf{k}_1,\mathbf{k}_2)$ is the fundamental quantity of interest in Fermi liquid theory, we will carefully discuss its properties and its relationship to nuclear observables. Assuming the interaction to be purely exchange, it can be written as

$$\begin{aligned} f(\mathbf{k}_1,\mathbf{k}_2) &= \frac{1}{N_0}[F(\mathbf{k}_1,\mathbf{k}_2) + F'(\mathbf{k}_1,\mathbf{k}_2)\tau_1\cdot\tau_2 + G(\mathbf{k}_1,\mathbf{k}_2)\sigma_1\cdot\sigma_2 \\ &+ G'(\mathbf{k}_1,\mathbf{k}_2)\tau_1\cdot\tau_2\sigma_1\cdot\sigma_2], \end{aligned} \tag{4.2}$$

where we have factored out the density of states per unit volume at the Fermi surface, $N_0 = \frac{2m^* k_F}{\hbar^2\pi^2}$, which leaves dimensionless Fermi liquid parameters denoted by F, G, F', G'. The spin-orbit interaction is neglected because it vanishes in the long wavelength limit in which we will be interested. Also, we have not included tensor operators (which would greatly complicate our calculation) because the tensor force contributes almost completely in second order, as shown in the original paper by Kuo and Brown [62], as an effective central interaction in the $^3S_1$ state. In [74] the tensor Fermi liquid parameters for symmetric nuclear matter were calculated from $V_{\mathrm{low}-k}$ in which the dominant second-order contributions from one-pion exchange were included. Since quasiparticles are well-defined only near the Fermi surface, we assume that $k_1 = k_F = k_2$. In this case the dimensionless Fermi liquid parameters F, F', G, G' depend on only the angle between $\mathbf{k}_1$ and $\mathbf{k}_2$, which we call θ. Then it is convenient to perform a Legendre polynomial expansion as follows

$$F(\mathbf{k},\mathbf{k}') = \sum_l F_l P_l(\cos\theta), \quad G(\mathbf{k},\mathbf{k}') = \sum_l G_l P_l(\cos\theta), \text{ etc.} \tag{4.3}$$

The Fermi liquid parameters $F_l, G_l, \ldots$ decrease rapidly for larger l, and so there are only a small number of parameters that can either be fit to experiment or calculated microscopically.

In the original application of the theory to liquid ^{3}He and nuclear systems, the quasiparticle interaction was obtained phenomenologically by fitting

the dimensionless Fermi liquid parameters to relevant data. For nuclear matter several important relationships exist between nuclear observables and the Fermi liquid parameters. Galilean invariance can be used [90] to connect the Landau parameter F_1 to the quasiparticle effective mass

$$\frac{m^*}{m} = 1 + F_1/3. \tag{4.4}$$

Adding a small number of neutrons and removing the same number of protons from the system will increase and decrease, respectively, the density of protons and neutrons in the system (and therefore the Fermi energies of the two species). The change in the energy, described by the symmetry energy β, can be related [94] to the Landau parameter F_0'

$$\beta = \frac{\hbar^2 k_F^2}{6m^*}(1 + F_0'). \tag{4.5}$$

In a similar way, the equal increase or decrease of the proton and neutron densities leads to a relationship between the scalar-isoscalar Landau parameter F_0 and the compression modulus $\mathcal{K}$

$$\mathcal{K} = \frac{3\hbar^2 k_F^2}{m^*}\left(1 + F_0\right). \tag{4.6}$$

Finally, it can be shown [94] that an odd nucleon added just above the Fermi sea induces a polarization of the medium leading to an anomalous contribution to the orbital gyromagnetic ratio of the form

$$\begin{aligned} g_l^p &= [1 - \delta g_l]\mu_N \\ g_l^n &= [\delta g_l]\mu_N, \end{aligned} \tag{4.7}$$

where δg_l is given by

$$\delta g_l = \frac{1}{6}\frac{F_1' - F_1}{1 + F_1/3}. \tag{4.8}$$

Clearly there are certain values of the Landau parameters that are physically unreasonable. For instance, if $F_1 < -3$ or $F_0 < -1$, the effective mass or compression modulus would be negative. Quite generally it can be shown [107] that the Landau parameters must satisfy stability conditions

$$X_l > -(2l + 1), \tag{4.9}$$

where X represents F, G, F', G'.

A rigorous foundation for the assumptions underlying Landau's theory can

be obtained through formal many-body techniques [108, 109]. It is not our goal to reproduce the original arguments [92], but rather to give a clear motivation for the diagrammatic expansion leading to the quasiparticle interaction. Starting from the usual definition of the four-point Green's function in momentum space

$$\begin{aligned} &G_{\alpha\beta,\gamma\delta}(k_1,k_2;k_3,k_4) = (2\pi)^8\delta^{(4)}(k_1+k_2-k_3-k_4) \\ &\times[G_{\alpha\gamma}(k_1)G_{\beta\delta}(k_2)\delta^{(4)}(k_1-k_3) - G_{\alpha\delta}(k_1)G_{\beta\gamma}(k_2)\delta^{(4)}(k_2-k_3) \\ &+\frac{i}{(2\pi)^4}G(k_1)G(k_2)G(k_3)G(k_4)\Gamma_{\alpha\beta,\gamma\delta}(k_1,k_2;k_3,k_4)], \end{aligned} \tag{4.10}$$

where $G(k_1)$ is the Fourier transform of $G(xt,x't')$ and $k_1,\ldots,k_4$ represent four-vectors (e.g. $k_1=(\mathbf{k}_1,\omega_1)$), it can be shown that the quasiparticle interaction is related to a certain limit of the four-point vertex function $\Gamma_{\alpha\beta,\gamma\delta}(k_1,k_2;k_3,k_4)$. From energy-momentum conservation ($k_1+k_2=k_3+k_4$) we can write $k_3-k_1=K=k_2-k_4$ and therefore define $\Gamma(k_1,k_2;K)=\Gamma(k_1,k_2;k_3,k_4)$. The important point is that since we are considering only low-energy long-wavelength excitations, the particle-hole energy-momentum K should be small. We can write a Bethe-Salpeter equation for the fully reducible vertex function Γ in terms of the *ph* irreducible vertex function $\tilde{\Gamma}$ in the direct channel with momentum transfer K:

$$\begin{aligned} \Gamma_{\alpha\beta,\gamma\delta}(k_1,k_2;K) &= \tilde{\Gamma}_{\alpha\beta,\gamma\delta}(k_1,k_2;K) \\ &-i\sum_{\epsilon,\eta}\int\frac{d^4q}{(2\pi)^4}\tilde{\Gamma}_{\alpha\epsilon,\gamma\eta}(k_1,q;K)G(q)G(q+K)\Gamma_{\eta\beta,\epsilon\delta}(q,k_2;K) \end{aligned} \tag{4.11}$$

shown diagrammatically in Fig. 4.1. The product of propagators may have singularities in the limit that $K\to 0$, in which case the poles can be replaced by δ-functions inside the integral:

$$G(q)G(q+K) = \frac{2i\pi z^2\hat{\mathbf{q}}\cdot\mathbf{K}}{\omega - v_F\hat{\mathbf{q}}\cdot\mathbf{K}}\delta(\epsilon-\mu)\delta(q-k_F)+\phi(\mathbf{q}), \tag{4.12}$$

where z is the renormalization at the quasiparticle pole and $\phi(\mathbf{q})$ accounts for the multipair background. The limit $K=(\omega,\mathbf{K})\to 0$ depends on the relative ordering of the two limits $\mathbf{K}\to 0$ and $\omega\to 0$. Defining

$$\begin{aligned} \Gamma^{\omega}(k_1,k_2) &= \lim_{\omega\to 0}\lim_{\mathbf{K}\to 0}\Gamma(k_1,k_2;K) \quad \text{and} \\ \Gamma^{K}(k_1,k_2) &= \lim_{\mathbf{K}\to 0}\lim_{\omega\to 0}\Gamma(k_1,k_2;K), \end{aligned} \tag{4.13}$$

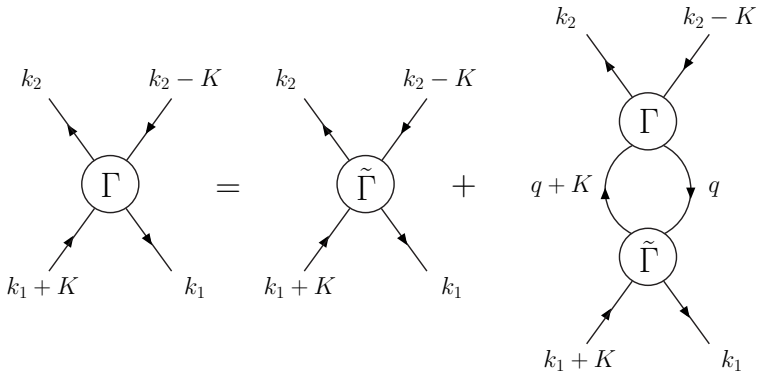

Figure 4.1: The Bethe-Salpeter equation for the fully irreducible vertex function Γ in terms of the *ph* irreducible vertex function $\tilde{\Gamma}$.

from eq. (4.12) we see that the product of propagators is regular for Γ^ω. Thus, to calculate Γ^ω we must first calculate the *ph* irreducible diagrams belonging to $\tilde{\Gamma}$ and then iterate via the Bethe-Salpeter equation with the intermediate multipair background ϕ. The δ-function singularities in Γ^K can be used to perform the integrals over q_0 and $|\mathbf{q}|$, and through algebraic manipulation it is possible to combine Γ^ω and Γ^K into a single integral equation

$$\begin{aligned}\Gamma^K_{\alpha\beta,\gamma\delta}(k_1,k_2) &= \Gamma^\omega_{\alpha\beta,\gamma\delta}(k_1,k_2) \\ &- \frac{1}{16\pi}N_0 z^2 \sum_{\epsilon,\eta}\int d\Omega_q \Gamma^\omega_{\alpha\epsilon,\gamma\eta}(k_1,q)\Gamma^K_{\eta\beta,\epsilon\delta}(q,k_2). \quad (4.14)\end{aligned}$$

Physically, Γ^ω represents the exchange of virtual excitations between quasiparticles, and Γ^K represents the forward scattering of quasiparticles at the Fermi surface. By relating these vertex functions to the equations describing zero sound, Landau [92] was able to make the identifications

$$\begin{aligned}f(k_1,k_2) &= z^2\Gamma^\omega(k_1,k_2) \quad \text{and} \\ a(k_1,k_2) &= z^2\Gamma^k(k_1,k_2), \quad (4.15)\end{aligned}$$

where $f(k_1,k_2)$ is just the quasiparticle interaction introduced earlier and $a(k_1,k_2)$ is the physical scattering amplitude.

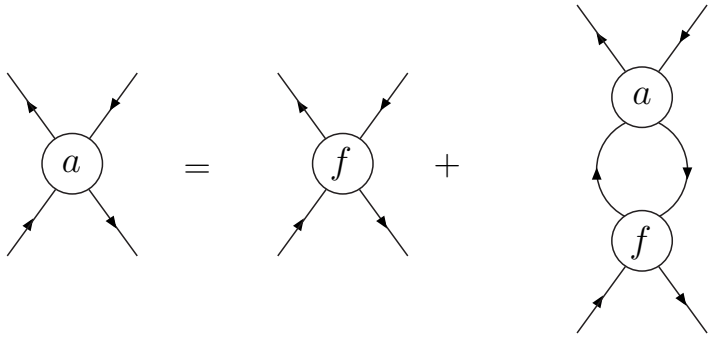

Figure 4.2: The diagrammatic relationship between the physical scattering amplitude a and the quasiparticle interaction f.

4.3 Induced interaction

In principle one could exactly calculate the quasiparticle interaction by summing up all ph irreducible diagrams contributing to the ph vertex function in the limit $k/\omega \to 0$. Since this is not practicable in general, one must limit the calculation to a certain subset of diagrams. We could proceed by calculating the relevant diagrams order by order, but this would miss an essential point, which we now elaborate. From eqs. (4.14) and (4.15), we see that the physical scattering amplitude $a(k_1, k_2)$ iterates the quasiparticle interaction to all orders through an integral equation shown schematically in Fig. 4.2. If only a finite set of diagrams are included in the quasiparticle interaction, then the scattering amplitude will not be antisymmetric. For instance, if we include only the bare particle-hole antisymmetrized vertex shown in Fig. 4.3(a), then diagram (b) will be contained in the equation for the scattering amplitude but its exchange diagram, labeled (c), will not. Quantitatively, the fact that the scattering amplitude is antisymmetric requires that it vanish in singlet-odd and triplet-odd states as the Landau angle θ approaches 0. This leads to two constraints [92, 110] on the Fermi liquid parameters in the form of sum rules:

$$\sum_l \left(\frac{F_l}{1 + F_l/(2l+1)} + 3\frac{G'_l}{1 + G'_l/(2l+1)} \right) = 0 \tag{4.16}$$

$$\sum_l \left(\frac{2}{3}\frac{F_l}{1 + F_l/(2l+1)} + \frac{F'_l}{1 + F'_l/(2l+1)} + \frac{G_l}{1 + G_l/(2l+1)} \right) = 0 \tag{4.17}$$

Clearly, the sum rules must be satisfied for the "correct" set of Fermi liquid

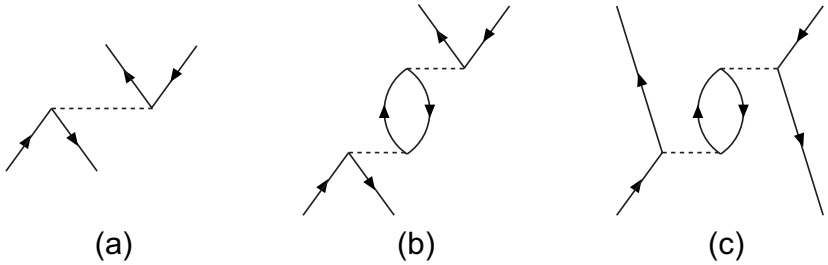

Figure 4.3: Diagrams contributing to the quasiparticle interaction f and the scattering amplitude a. Diagrams (a) and (c) contribute to f, whereas all three contribute to a.

parameters describing nuclear matter. To account for this infinite set of exchange diagrams, Babu and Brown [66] proposed separating the quasiparticle interaction into a *driving term* and an *induced term*:

$$f(k,k') = f_d(k,k') + f_i(k,k'), \tag{4.18}$$

where the induced interaction is defined to contain those diagrams that would be the exchange terms necessary to preserve the antisymmetry of $a(k_1,k_2)$. Then the induced interaction is given by a diagrammatic expansion shown in Fig. 4.4. Physically, the induced interaction represents that part of the quasiparticle interaction that results from the exchange of virtual collective modes, which can be classified as density, spin, or isospin excitations. In the limit that $\mathbf{k}_1 \to \mathbf{k}_2$ it can be rigorously proved [66] that the coupling of quasiparticles to these collective excitations is precisely through the quasiparticle interaction itself, thereby justifying the diagrammatic expression in Fig. 4.4.

The relationship between the induced interaction and the full quasiparticle interaction was derived by Babu and Brown [66] for liquid ^{3}He and applied to nuclear matter by Sjöberg [102]. To lowest order in the Fermi liquid parame-

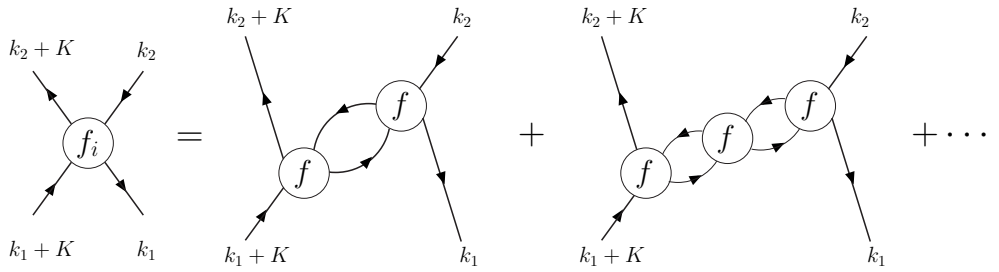

Figure 4.4: The diagrammatic form of the induced interaction. In the limit that $k_1 = k_2$ it can be shown that the external lines exactly couple to particle-hole excitations through the f function.

ters, the induced interaction is given by

$$\begin{aligned}
4F_i &= \left[\frac{{F_0}^2}{1+F_0\alpha_0} + \frac{3{F_0}'^2}{1+F_0'\alpha_0} + \frac{3{G_0}^2}{1+G_0\alpha_0} + \frac{9{G_0}'^2}{1+G_0'\alpha_0}\right]\alpha_0 \\
4G_i &= \left[\frac{{F_0}^2}{1+F_0\alpha_0} + \frac{3{F_0}'^2}{1+F_0'\alpha_0} - \frac{{G_0}^2}{1+G_0\alpha_0} - \frac{3{G_0}'^2}{1+G_0'\alpha_0}\right]\alpha_0 \\
4F_i' &= \left[\frac{{F_0}^2}{1+F_0\alpha_0} - \frac{{F_0}'^2}{1+F_0'\alpha_0} + \frac{3{G_0}^2}{1+G_0\alpha_0} - \frac{3{G_0}'^2}{1+G_0'\alpha_0}\right]\alpha_0 \\
4G_i' &= \left[\frac{{F_0}^2}{1+F_0\alpha_0} - \frac{{F_0}'^2}{1+F_0'\alpha_0} - \frac{{G_0}^2}{1+G_0\alpha_0} + \frac{{G_0}'^2}{1+G_0'\alpha_0}\right]\alpha_0
\end{aligned} \tag{4.19}$$

where

$$\alpha_0 = \alpha_0(\mathbf{q},0) = \frac{1}{2} + \frac{1}{2}\left(\frac{q}{4k_F} - \frac{k_F}{q}\right)\ln\frac{k_F - q/2}{k_F + q/2} \tag{4.20}$$

is the Lindhard function, which is related to the density-density correlation function $\chi_{\rho\rho}$ by

$$\chi_{\rho\rho}(\mathbf{q},\omega) = \frac{-\alpha_0(\mathbf{q},\omega)}{1+F_0\alpha_0(\mathbf{q},\omega)}, \tag{4.21}$$

and $\mathbf{q} = \mathbf{k}_1 - \mathbf{k}_2$. The interpretation of equation (4.19) is as follows. The Landau parameters in the numerator describe the coupling of quasiparticles to particular collective modes. For instance, the F_0 represents the coupling to density excitations, G_0 the coupling to spin excitations, etc., and the denominators enter from the summation of bubbles to all orders. Including the $l = 1$

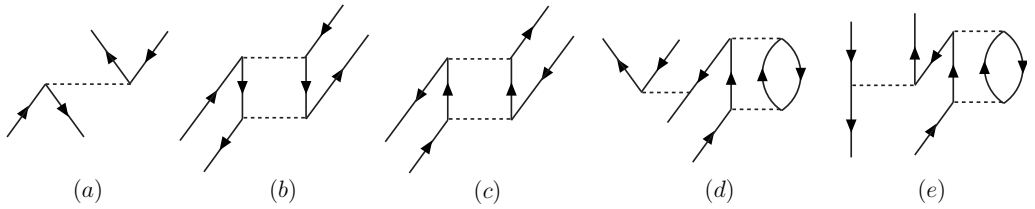

Figure 4.5: A selection of diagrams contributing to the driving term in the quasiparticle interaction. Diagrams (d) and (e) are included implicitly through the renormalization at the quasiparticle pole.

Fermi liquid parameters, the induced interaction is given by

$$4F_i = \left[\frac{{F_0}^2\alpha_0}{1+F_0\alpha_0} + \left(1-\frac{q^2}{4k_F^2}\right)\frac{{F_1}^2\alpha_1}{1+F_1\alpha_1} + \frac{3{G_0}^2\alpha_0}{1+G_0\alpha_0} + \left(1-\frac{q^2}{4k_F^2}\right)\frac{3{G_1}^2\alpha_1}{1+G_1\alpha_1} + \frac{3{F_0}'^2\alpha_0}{1+F_0'\alpha_0} + \left(1-\frac{q^2}{4k_F^2}\right)\frac{3{F_1}'^2\alpha_1}{1+F_1'\alpha_1} + \frac{9{G_0}'^2\alpha_0}{1+G_0'\alpha_0} + \left(1-\frac{q^2}{4k_F^2}\right)\frac{9{G_1}'^2\alpha_1}{1+G_1'\alpha_1}\right], \tag{4.22}$$

where α_1 defined by

$$\alpha_1(\mathbf{q},0) = \frac{1}{2}\left[\frac{3}{8} - \frac{k_F^2}{2q^2} + \left(\frac{k_F^3}{2q^3} + \frac{k_F}{4q} - \frac{3q}{32k_F}\right)\ln\left(\frac{k_F+q/2}{k_F-q/2}\right)\right] \tag{4.23}$$

is related to the current-current correlation function, and analogous expressions hold for the spin- and isospin-dependent parts of the induced interaction. These equations were first obtained in [105], carried far enough to include velocity-dependent effects in terms of an effective mass, in the approximation of quadratic spectrum.

Having characterized the induced part of the quasiparticle interaction, let us now elaborate on the driving term. By definition, this component of the interaction consists of those diagrams that cannot be separated into two diagrams by cutting one particle line and one hole line. Some of the low order terms contributing to the driving term are shown in Fig. 4.5, where the interaction vertices are assumed to be antisymmetrized. Some higher-order terms, such as diagram (d) in Fig. 4.5, are included implicitly through the quasiparticle renormalization z and need not be calculated explicitly, as described in detail in [111]. In order to preserve the Pauli principle sum rules (4.16) and (4.17) the driving term must be antisymmetrized. Thus, including Fig. 4.5(d) requires that (e) also be included in order for the scattering amplitude to be antisymmetric.

4.4 Calculations and results

According to the discussion in the previous section, the starting point of a microscopic derivation of the quasiparticle interaction is a calculation of the antisymmetrized driving term to some specified order in the bare potential. Nearly all previous calculations have used the G-matrix, since it is well known that the unrenormalized high-precision NN potentials are unsuitable for perturbation theory calculations due to the presence of a strong short-distance repulsion. The resummation of particle-particle ladder diagrams in the G-matrix softens the potential but introduces several undesirable features from the perspective of Fermi liquid theory. Most important is the unphysical gap in the single particle energy spectrum at the Fermi surface due to the fact that hole lines receive self-energy corrections but particle lines do not. In the past it was suggested [98, 103] that introducing a model space, within which particles and holes are treated symmetrically, could overcome this difficulty.

An alternative method for taming the repulsive core is to integrate out the high momentum components of the interaction in such a way that the low energy dynamics are preserved [14, 58]. This is accomplished by rewriting the half-on-shell T-matrix

$$T(p', p, p^2) = V_{NN}(p', p) + \frac{2}{\pi}\mathcal{P}\int_0^\infty \frac{V_{NN}(p', q)T(q, p, p^2)}{p^2 - q^2}q^2 dq \tag{4.24}$$

with an explicit momentum cutoff Λ, which yields the low momentum T-matrix defined by

$$T_{\text{low}-k}(p', p, p^2) = V_{\text{low}-k}(p', p) + \frac{2}{\pi}\mathcal{P}\int_0^\Lambda \frac{V_{\text{low}-k}(p', q)T_{\text{low}-k}(q, p, p^2)}{p^2 - q^2}q^2 dq. \tag{4.25}$$

Enforcing the requirement that $T_{\text{low}-k}(p', p, p^2) = T(p', p, p^2)$ for $p', p < \Lambda$ preserves the low energy physics encoded in the scattering phase shifts. Remarkably, under this construction all high-precision NN potentials flow to a nearly universal low momentum interaction $V_{\text{low}-k}$ as the momentum cutoff Λ is lowered to 2.1 fm^{-1}. In fact, $k = 2.1$ fm^{-1} is precisely the CM momentum beyond which the experimental phase shift analysis has not been incorporated in the high-precision NN interactions.

For an initial approximation to the driving term, we include the first-order antisymmetrized matrix element shown diagrammatically in Fig. 4.5(a) as well as the higher order diagrams, such as (d) and (e), that are included implicitly through the renormalization strength at the quasiparticle pole. The

quasiparticles are confined to a thin model space P near the Fermi surface

$$P = \lim_{\delta \to 0} \sum_{k_F < k < k_F + \delta} |\boldsymbol{k}\rangle\langle\boldsymbol{k}|, \tag{4.26}$$

and the first-order contribution is given by

$$\langle \boldsymbol{k}_1 \boldsymbol{k}_2 ST|V|(\boldsymbol{k}_3 \boldsymbol{k}_4 - \boldsymbol{k}_4 \boldsymbol{k}_3)ST\rangle = \langle k, \theta ST|V|k, \theta ST\rangle, \tag{4.27}$$

where $k_1 = k_2 = k_3 = k_4 = k_F$, θ is the angle between the two momenta, and the relative momentum $k = k_F \sin(\theta/2)$. Given the $V_{\mathrm{low}-k}$ matrix elements in the basis $|klSTJ\rangle$, we project onto the central components and change from a spherical wave basis to a plane wave basis. Then the dimensionful driving term is given by

$$\langle kST|V_d|kST\rangle = z^2 \frac{4\pi}{2S+1} \sum_{J,l} (2J+1)(1-(-1)^{l+S+T}) \langle klSJT|V_{\mathrm{low}-k}|klSJT\rangle. \tag{4.28}$$

Inserting the form of the quasiparticle interaction in eq. (4.2) into the left hand side of eq. (4.28), we obtain the Fermi liquid parameters in terms of $V_{ST}(k) = \langle kST|V|kST\rangle$. The result is

$$\begin{aligned}
f &= \frac{1}{16}V_{00} + \frac{3}{16}V_{01} + \frac{3}{16}V_{10} + \frac{9}{16}V_{11} \\
g &= -\frac{1}{16}V_{00} - \frac{3}{16}V_{01} + \frac{1}{16}V_{10} + \frac{3}{16}V_{11} \\
f' &= -\frac{1}{16}V_{00} + \frac{1}{16}V_{01} - \frac{3}{16}V_{10} + \frac{3}{16}V_{11} \\
g' &= \frac{1}{16}V_{00} - \frac{1}{16}V_{01} - \frac{1}{16}V_{10} + \frac{1}{16}V_{11},
\end{aligned} \tag{4.29}$$

where the momentum dependence has been suppressed for simplicity. From eq. (4.4) it can be shown that

$$\frac{m^*}{m} = \frac{1}{1 - \mu f_1/3}, \tag{4.30}$$

where $\mu = 2mk_F/\pi^2\hbar^2 = \frac{m}{m^*}N_0$, from which we construct the dimensionless Fermi liquid parameters. In all of our calculations we include partial waves up to $J = 6$. In Table 4.1 we show the Landau parameters of the driving term derived from three different low momentum interactions obtained from the Nijmegen I & II potentials [6] and the CD-Bonn potential [9] for a momentum cutoff of $\Lambda = 2.1$ fm^{-1} and a Fermi momentum of $k_F = 1.36$ fm^{-1}. From

	Nijmegen I			
l	F_l	G_l	F'_l	G'_l
0	-1.230	0.130	0.392	0.619
1	-0.506	0.241	0.252	0.118
2	-0.201	0.120	0.101	0.021
3	-0.110	0.054	0.051	0.009
	Nijmegen II			
l	F_l	G_l	F'_l	G'_l
0	-1.475	0.248	0.549	0.583
1	-0.445	0.161	0.172	0.225
2	-0.213	0.127	0.106	0.020
3	-0.120	0.060	0.056	0.007
	CD-Bonn			
l	F_l	G_l	F'_l	G'_l
0	-1.199	0.135	0.350	0.603
1	-0.498	0.240	0.259	0.118
2	-0.200	0.122	0.101	0.022
3	-0.111	0.055	0.051	0.010

Table 4.1: The Fermi liquid parameters of the NN interaction $V_{\mathrm{low}-k}$ derived from the Nijmegen potentials and CD-Bonn potential for a cutoff of $\Lambda = 2.1$ fm^{-1} and Fermi momentum 1.36 fm^{-1}.

the available theoretical analyses of nucleon momentum distributions [112], we take the quasiparticle renormalization strength to be $z = 0.7$ for nuclear matter.

The induced interaction is obtained by iterating equations (4.18) and (4.22) until a self-consistent solution is reached. The density-density and current-current correlation functions in (4.22) introduce a momentum dependence in the induced interaction, and the Fermi liquid parameters for the induced interaction are obtained by projecting onto the Legendre polynomials

$$F_{i,l} = \frac{2l+1}{2} \int_{-1}^{1} F_i(\theta) P_l(\cos\theta)\, d(\cos\theta), \text{ etc.} \tag{4.31}$$

For the first iteration we use the Landau parameters obtained from the bare low momentum interaction as an estimate for the full quasiparticle interaction in eq. (4.22). However, since F_0 does not satisfy the stability criteria (4.9) for either the Nijmegen or CD-Bonn potentials, in the first iteration we replace it in both cases with an arbitrary value that does. The convergence of

	Full			
l	F	G	F'	G'
0	-0.476	0.025	0.221	0.784
1	-0.335	0.263	0.273	0.171
2	-0.238	0.139	0.117	0.020
3	-0.101	0.055	0.050	0.014
	Driving			
l	F_d	G_d	F'_d	G'_d
0	-1.276	0.144	0.373	0.642
1	-0.530	0.256	0.275	0.125
2	-0.212	0.130	0.107	0.024
3	-0.119	0.059	0.054	0.011
	Induced			
l	F_i	G_i	F'_i	G'_i
0	0.801	-0.119	-0.152	0.142
1	0.195	0.007	-0.002	0.048
2	-0.026	0.009	0.010	-0.003
3	0.018	-0.004	-0.004	0.003

Table 4.2: The self-consistent solution of the Babu-Brown equations for the low momentum CD-Bonn potential. The full Fermi liquid parameters are obtained by projecting the quasiparticle interaction in Fig. 4.6 onto the Legendre polynomials.

the iteration scheme is generally rapid and relatively insensitive to the set of initial parameters chosen for the low-momentum Nijmegen I and CD-Bonn potentials. In contrast, the low momentum Nijmegen II potential exhibits poor convergence properties, though a solution to the coupled equations can still be found. For a completely consistent solution at each iteration we recalculate the driving term with the new effective mass.

The final self-consistent result for the quasiparticle interaction is shown in Fig. 4.6 for the CD-Bonn potential, and the Fermi liquid parameters for the driving term, induced interaction, and full quasiparticle interaction are shown in Table 4.2. For comparison we list the Fermi liquid parameters obtained in [74] where the spin-independent Landau parameters were taken from experiment and used to calculate the spin-dependent parameters with a set of nontrivial sum rules: Although the experimental values for the spin-independent parameters are appreciably different from the self-consistent solution we have obtained, our values for the spin-dependent parameters fall within

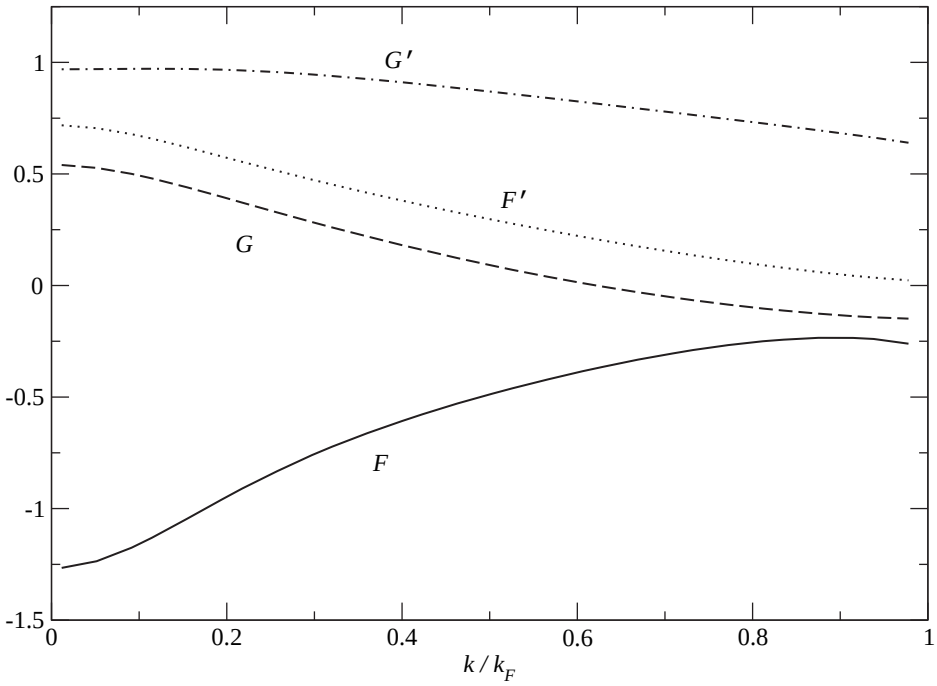

Figure 4.6: The self-consistent solution for the full quasiparticle interaction as a function of $k = \frac{1}{2}|\mathbf{k}_1 - \mathbf{k}_2|$ derived from the low momentum CD-Bonn potential.

$F_0 = -0.27$	$G_0 = 0.15 \pm 0.3$	$F_0{}' = 0.71$	$G_0{}' = 1.0 \pm 0.2$
$F_1 = -0.85$	$G_1 = 0.45 \pm 0.3$	$F_1{}' = 0.14$	$G_1{}' = 0.0 \pm 0.2$

Table 4.3: Fermi liquid parameters deduced from renormalization group equations in [74].

	Nijmegen I	Nijmegen II	CD-Bonn
m^*/m	0.887	0.930	0.888
$\mathcal{K}$ [MeV]	136	102	136
β [MeV]	18.1	20.5	17.6
δg_l [μ_N]	0.682	0.452	0.685
δS_1	0.20	0.16	0.27
δS_2	-0.04	-0.02	-0.04

Table 4.4: Nuclear observables obtained from the self-consistent solution of the Babu-Brown equations and deviations δS_1 and δS_2 from the Pauli principle sum rules.

the errors predicted from the sum rules. However, the main effect of the induced interaction is to cut down the strong attraction in the spin-independent, isospin-independent part of the quasiparticle interaction. In fact, the repulsion in this channel coming from the induced interaction is large enough for the resulting F_0 to satisfy the stability condition in (4.9). The effective mass, compression modulus, and symmetry energy are shown in Table 4.4 together with the deviations δS_1 and δS_2 from the sum rules (4.16) and (4.17). We list the results for the three different bare potentials with a momentum cutoff of $\Lambda = 2.1$ fm^{-1}. In calculating the contributions to (4.16) and (4.17) we have included Landau parameters for $l \leq 3$. The compression modulus for nuclear matter is extrapolated from the data on giant monopole resonances in heavy nuclei, with the expected value being $200 - 300$ MeV [85, 86]. The symmetry energy is determined by fitting the data on nuclear masses to various versions of the semi-empirical mass formula [113], and currently the accepted value is $\beta = 25$–35 MeV [86, 88]. Both the compression modulus and the symmetry energy shown in Table 4.4 are significantly smaller than the experimental values. On the other hand, the anomalous orbital gyromagnetic ratio, determined from giant dipole resonances in heavy nuclei, is too large compared with the experimental value of $\delta g_l^p = 0.23 \pm 0.03$ [114].

As suggested in the introduction, we propose to remedy these discrepancies by considering the effects of Brown-Rho scaling on hadronic masses. The proposed scaling law for light hadrons – other than the pseudoscalar mesons, whose masses are protected by chiral invariance – is [45, 115]

$$\frac{m_V^*}{m_V} = \frac{m_\sigma^*}{m_\sigma} = \sqrt{\frac{g_A}{g_A^*}}\frac{m_N^*}{m_N} = 1 - C\frac{n}{n_0}, \tag{4.32}$$

where the subscript V denotes either the ρ or ω vector meson, σ refers to

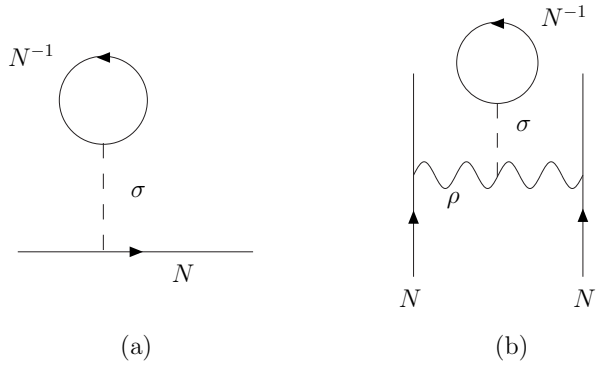

Figure 4.7: Walecka mean field contribution of the scalar tadpole to the nucleon mass (a) and its extrapolation to constituent quarks in vector mesons (b).

the scalar meson, g_A is the axial vector coupling, and n/n_0 is the ratio of the medium density to nuclear matter density. This scaling can be thought of as extending Walecka mean field theory, in which the scalar tadpole contribution to the nucleon self-energy lowers the effective mass, to the level of constituent quarks. Attaching a scalar tadpole on the nucleon line, as shown in Fig. 4.7(a), lowers the mass according to (4.32), and a scalar tadpole connected to the vector mesons gives an effective three-body force as shown in Fig. 4.7(b). Including the in-medium scaling of the axial-vector coupling, which should approach $g_A^* = 1$ at chiral restoration, the net result is a lowering of the in-medium m_V^* by $\sim 2/3$ as much as m_N^*. Recent experimental results [53, 54] are consistent with the scaling law (4.32) for $C = 0.14$ and 0.092, respectively. The Brown-Rho "parametric scaling" has $C = 0.2$. However, the dense loop term ΔM [116] gives a shift of the ρ-meson pole upwards. So far no one has been able to calculate it at finite density.

A number of previous studies [117–119] were successful in describing nuclear matter by starting from a chiral Lagrangian with nuclear, scalar, and vector degrees of freedom in which the hadronic masses were scaled with density according to (4.32). In particular, the compression modulus and anomalous orbital gyromagnetic ratio were found to be in excellent agreement with experiment, which suggests that a similar approach may prove fruitful in our present analysis. An alternative approach, complementary to the chiral Lagrangian method, is to include medium modifications directly into a one-boson-exchange potential. Such a calculation was carried out in [84] to study the saturation of nuclear matter. In their work it was suggested that the σ particle should be constructed microscopically as a pair of correlated pions interacting largely

through crossed-channel ρ exchange. Medium modifications to the σ mass then arise naturally from the density-dependence of the ρ mass. The final conclusion established in [84] is that at low densities the σ scales according to (4.32) but that toward nuclear matter density the scaling is slowed to such an extent that saturation can be achieved.

We proceed along the lines of [84] and introduce medium modifications directly into a one-boson-exchange potential. The most refined NN potentials in this category are the Nijmegen I, Nijmegen II, and CD-Bonn potentials. The Nijmegen potentials include contributions from the exchange of $\rho, \omega, \phi, \sigma, f_0$, and a_0 mesons, as well as the pseudoscalar particles which do not receive medium modifications in Brown-Rho scaling. The CD-Bonn potential includes two vector particles (the ρ and ω) and two scalars (σ_1 and σ_2). For both potentials we scale the vector meson masses by 15% and the scalar meson masses by 7%. In this way we roughly account for the decreased scaling of the scalar particle mass observed in [84]. In the full many-body calculation we also scale the nucleon mass by 15% and with an additional $\sqrt{g_A^*/g_A} \simeq 1/\sqrt{1.25}$ at nuclear matter density. It is essential to also scale the form factor cutoffs Λ_f of the vector mesons in the boson-exchange potentials.

In Table 4.5 we show the effective mass, compression modulus, symmetry energy, and anomalous orbital gyromagnetic ratio for the Nijmegen I & II and CD-Bonn potentials with the in-medium modifications. We also show for comparison the results from the Nijmegen93 one-boson-exchange potential, which has only 15 free parameters and is not fine-tuned separately in each partial wave. We observe that the iterative solution is in better agreement with all nuclear observables. The anomalously large compression modulus in the CD-Bonn potential results almost completely from the presence of a large ω coupling constant $g^2_{\omega NN}/4\pi = 20.0$. With the same $g^2_{\omega NN}/4\pi$ and Bonn-B potential, Rapp *et al.* [84] obtained $\mathcal{K} = 356$ MeV. The compression modulus is very sensitive to this parameter, as we have checked that dropping this coupling by 20% cuts the compression modulus in half but alters the other nuclear observables by less than 5%. The naive quark model predicts a ratio of $g^2_{\omega NN}/g^2_{\rho NN} = 9$ between the ω and ρ coupling constants, which is largely violated in the CD-Bonn potential $g^2_{\omega NN}/g^2_{\rho NN} = 24$ though roughly satisfied in the Nijmegen potentials $g^2_{\omega NN}/g^2_{\rho NN} = 11$, perhaps resulting in better agreement with experiment.

Thus, by extension of the Walecka mean field on nucleons to those on constituent quarks, we obtain the Fermi liquid parameters for the theory that is now essentially Brown-Rho scaled, as shown in Table 4.6. One should note that these results are only for infinite nuclear matter and especially the three-body term will act in many different diagrams in the finite systems. However, our

	$V_{\rm NI}$	$V_{\rm NII}$	V_{N93}	$V_{\rm CDB}$
m^*/m	0.721	0.763	0.696	0.682
$\mathcal{K}$ [MeV]	218	142	190	495
β [MeV]	20.4	25.5	23.7	19.2
δg_l	0.246	0.181	0.283	0.267

Table 4.5: Nuclear observables obtained from the self-consistent solution to the Babu-Brown equations incorporating Brown-Rho scaling. Four different bare potentials – the CD-Bonn potential ($V_{\rm CDB}$), Nijmegen I ($V_{\rm NI}$), Nijmegen II ($V_{\rm NII}$), and Nijmegen93 ($N93$) potentials – were used to construct low momentum interactions for a cutoff of $\Lambda = 2.1$ fm^{-1}.

l	F_l	G_l	F'_l	G'_l
0	-0.20 ± 0.39	0.04 ± 0.11	0.24 ± 0.16	0.53 ± 0.09
1	-0.86 ± 0.10	0.19 ± 0.06	0.18 ± 0.05	0.17 ± 0.12
2	-0.21 ± 0.01	0.12 ± 0.01	0.10 ± 0.02	0.01 ± 0.02
3	-0.09 ± 0.01	0.05 ± 0.01	0.05 ± 0.01	0.01 ± 0.01

Table 4.6: Fermi liquid coefficients for the self-consistent solution to the Babu-Brown equations using Brown-Rho scaled nucleon and meson masses in the four low momentum CD-Bonn and Nijmegen potentials listed in Table 4.5. The tabulated values display the average and spread from the four different potentials and not the actual uncertainties associated with the Fermi liquid parameters.

arguments suggest that the three-body terms intrinsic to Brown-Rho scaling will be useful in stabilizing light nuclei.

4.5 Discussion of the tensor force

The tensor force contributes chiefly in second order perturbation theory as an effective central force in the $I = 1$ channel. As the density increases, some of the intermediate states are blocked by the Pauli principle. In the two-body system the tensor force contributes to the $^3S_1$ state, but not to the $^1S_0$ state, and gives most of the attractive interaction difference between the $^3S_1$ and $^1S_0$ states, effectively binding the deuteron. However, the intermediate state energies relevant for the second-order tensor force are > 225 MeV (See Fig. 69 of [64] which is for ^{40}Ca. For nuclear matter the intermediate state momenta would be higher.), well above the Fermi energy of nuclear matter, and most

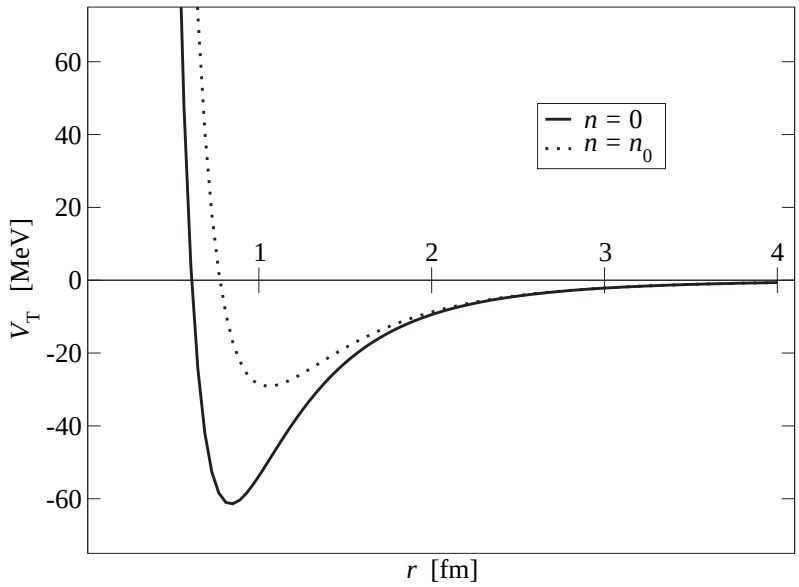

Figure 4.8: Reduction in the strength of the tensor force due to a scaled ρ-meson mass. Contributions from both π-meson and ρ-meson exchange are included in both curves. We have used the Brown-Rho parametric scaling, so that at nuclear matter density $m_\rho^* = 0.8 m_\rho$.

intermediate momenta are above the $V_{\mathrm{low}-k}$ upper model space limit of 420 MeV/c, so the tensor force is largely integrated out.

However, since the beginning of Brown-Rho scaling it has been understood that the tensor force is rapidly cut down with increasing density. That is because the pion mass does not change with density, being protected by chiral invariance, but the ρ-meson mass, which is dynamically generated, decreases by 20% (parametric scaling) in going from a density of $n = 0$ to nuclear matter density $n = n_0$. Since the ρ-meson exchange contributes with opposite sign from that of the pion, this cuts down the tensor force substantially. In Fig. 4.8 we show the total tensor force from π and ρ exchange at zero density and nuclear matter density n_0. Since it enters in the square, this means a factor of several drop in the tensor contribution to the binding energy, as shown in Fig. 4.9.

We believe that the work of ref. [53] shows unambiguously that the mass of the ω-meson is $\sim 14\%$ lower at nuclear matter density than in free space. It is remarkable that nuclear structure calculations have been carried out for many years without density-dependent masses but with results usually in quanti-

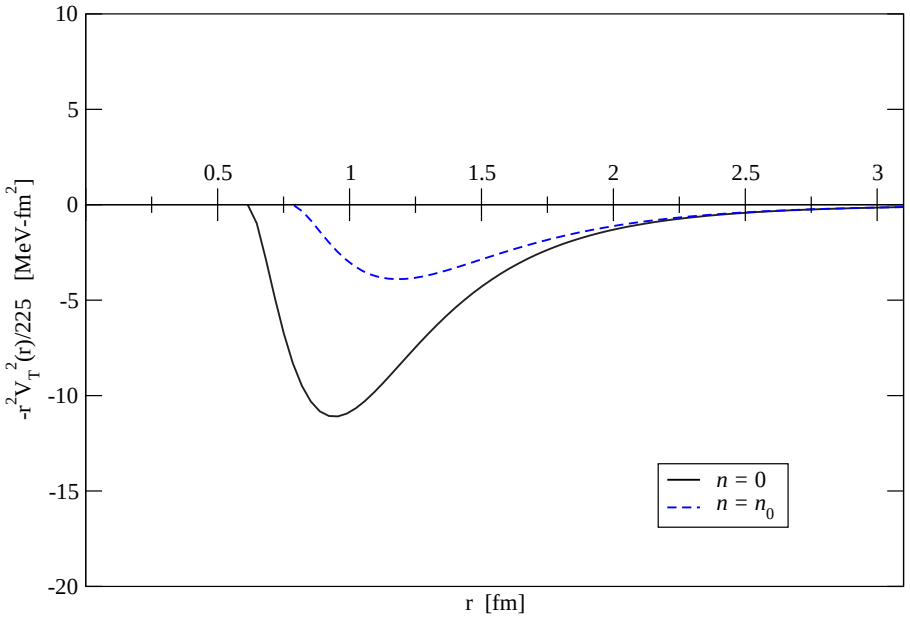

Figure 4.9: Reduction of the tensor force in second order perturbation theory due to a scaled ρ-meson mass. The intermediate state energy is approximated as 225 MeV. Contributions from both π-meson and ρ-meson exchange are included in both curves. At nuclear matter density, n_0, we have used the parametric scaling $m_\rho^* = 0.8 m_\rho$.

tative agreement with experiment. In [56] Brown and Rho showed that in cases where the exchange of the π-meson is not important, such as in Dirac phenomenology, there is a scale invariance such that if the masses of all relevant mesons are changed by the same amount, the results for the physical phenomena are very little changed.

Since the pion exchange gives the longest range part of the nucleon-nucleon interaction, it is amazing that there are not clearcut examples in nuclear spectroscopy such as level orderings that are altered by the ρ-meson exchange playing counterpoint to the π-meson exchange, as we find in this paper for nuclear saturation. The in-medium decrease in the ρ-mass increases the effect of ρ-exchange, which enters so as to cut down the overall tensor force, the ρ and π exchange entering with opposite sign.

Finally, nearly forty years since the Kuo-Brown nucleon-nucleon forces were first published, it was shown [65] that the summation of core polarization diagrams to all orders is well-approximated by a single bubble. However, in light of the double decimation of [56] being carried out here in one step, these forces should be modified to include the medium dependence of the masses. Phenomenologically this can be done by introducing three-body terms, as we did here, but from our treatment of the second-order tensor force it is clear that this should be done at constituent quark level.

4.6 Conclusion

We believe that by discussing the nuclear many-body problem within the context of Fermi liquid theory with the interaction $V_{\mathrm{low}-k}$ following the work of Schwenk *et al.* [74] we have a format for understanding connections between the physical properties of the many-body system and the nuclear potentials. We carried out an iterative solution of the Babu-Brown equations, which include both density-density and current-current correlation functions, calculating input potentials via a momentum space decimation to $V_{\mathrm{low}-k}$. By including Brown-Rho scaling through scalar tadpoles, as suggested by Walecka theory, our iterative solution provides the empirical Fermi liquid quantities. Our nucleon effective mass is on the low side of those usually employed, as is common in Walecka mean field theory.

Chapter 5

All-Order Core Polarization and Shell Model Effective Interactions

5.1 Introduction.

Understanding the properties of finite nuclei starting from realistic models of the NN interaction in free space is one of the most important programs in nuclear physics. In the previous chapters we described the first step in developing a formalism for such studies: taming the strong short-distance repulsion in relative S-states. Traditionally, microscopic studies of finite nuclei have relied on first constructing the G-matrix, but the development of low momentum interactions that are energy-independent and well-behaved at short distances have provided a compelling new framework for calculating the properties of finite nuclei from realistic NN interactions.

Since the early works of Bertsch [120] and Kuo and Brown [62], the effect of core polarization in microscopic calculations of finite nuclei has received much attention. Core polarization is particularly important in the shell model effective interactions, where this process provides the long-range inter-nucleon interaction mediated by excitations of the core [64]. In microscopic calculations of effective interactions, core polarization has played an essential role, as illustrated by the familiar situation in ^{18}O. There the spectrum calculated with the bare G-matrix was too compressed compared with experiment, while the inclusion of core polarization had the desirable effect of both lowering the 0^+ ground state and raising the 4^+ state, leading to a much improved agreement with experiment [62, 120]. As pointed out by Zuker [121], the Kuo-Brown matrix elements, although developed quite some time ago, continue to be a

highly useful shell model effective interaction. It should be noted that the core polarization (CP) diagrams associated with the above interactions were all calculated to second order (in the G-matrix) in perturbation theory. But what are the effects of core polarization beyond second order, and how can they be calculated? In this chapter we would like to address these questions and present an all-order summation of CP diagrams for the *sd*-shell interactions.

There have been a number of important CP studies beyond second order. Third-order core polarization diagrams, including those with one fold, were studied in detail by Barrett and Kirson [122] for the *sd*-shell effective interactions. Hjorth-Jensen *et al.* [123] have carried out extensive investigations of the third-order CP diagrams for the tin region. A main result of these studies is that the effect of the third-order diagrams is generally comparable to that of the second order; the former cannot be ignored in comparison with the latter. As is well known, high-order CP calculations are difficult to perform, largely because the number of CP diagrams grows rapidly as one goes to higher orders in perturbation theory. The number of diagrams at third order is already quite large, though still manageable. Primarily because of this difficulty, a complete fourth-order calculation has never been carried out. It was soon realized that an order-by-order calculation of CP diagrams beyond third order is not practicable. To fully assess the effects of core polarization to high order, a non-perturbative method is called for.

In this chapter we introduce a new formalism for summing core polarization diagrams to all orders. The non-perturbative method we use is based on the elegant and rigorous induced interaction approach of Kirson [124, 125] and Babu and Brown [66], hereafter referred to as KBB. Other successful non-perturbative summation methods have also been developed, such as the parquet summation [126, 127] and coupled cluster expansion [128]. In the KBB formalism the vertex functions are obtained by solving a set of self-consistent equations, thereby generating CP diagrams to all orders. Using this approach, Kirson has studied ^{18}O and ^{18}F using a G-matrix interaction, and Sprung and Jopko [129] have carried out a model study of this approach using a separable interaction. A main conclusion of both studies is that when CP diagrams are included to all orders the effective interaction is very close to that given by the bare interaction alone. In contrast, Sjöberg [102] applied the Babu-Brown formalism to nuclear matter and found that the inclusion of CP diagrams to all orders has a significant effect on the Fermi liquid parameters, in comparison with those given by the bare interaction. These conflicting results for CP studies of finite nuclei and infinite nuclear matter have served as a primary motivation for our present re-examination of the CP effect.

Our application of the KBB formalism to shell-model effective interactions

is similar to that of Kirson, but our treatment is different in a number of important regards. As we will discuss, the particle-core and hole-core coupling vertices used in the present work include a larger class of diagrams than have been previously studied. We will show how the inclusion of these diagrams is facilitated by using the recently developed low-momentum nucleon-nucleon interaction $V_{\mathrm{low-k}}$ [14, 15, 57, 73, 75, 130, 131] instead of the previously used G-matrix. This is primarily because the G-matrix [123, 132] depends on both starting energy and Pauli exclusion operator, while $V_{\mathrm{low-k}}$ depends on neither. It is noted that the S-wave interactions calculated from the Moszkowski-Scott separation method gave essentially the same matrix elements as $V_{\mathrm{low-k}}$.[69, 133] In the subsequent Formalism section we will discuss these topics in greater detail, and in the final section we present our results together with a summary.

5.2 Formalism

The many-particle Schrödinger equation describing the state of a nucleus is given by

$$H\Psi_n = E_n\Psi_n, \tag{5.1}$$

which cannot be solved exactly beyond just a few interacting nucleons. Therefore, it is practical to assume that we can neglect the detailed dynamics of nucleons filling the closed nuclear shells. In this way, we focus directly on the valence nucleons and attempt to derive the energy spectrum by considering the model space problem

$$PH_{eff}P\Psi_m = (E_m - E_0^c)\Psi_m, \quad m = 1, 2, \ldots, d \tag{5.2}$$

where P is the projection operator

$$P = \sum_i^d |\Phi_i\rangle \langle\Phi_i| \tag{5.3}$$

that projects onto the model space consisting of the valence nucleons (labeled $1, 2, \ldots, d$). These valence nucleons occupy the unperturbed shell model states Φ_i defined by

$$H_0\Phi_n = \epsilon_n\Phi_n. \tag{5.4}$$

The unperturbed Hamiltonian H_0 consists of the kinetic energy and a single particle harmonic oscillator potential U

$$H_0 = T + U \tag{5.5}$$

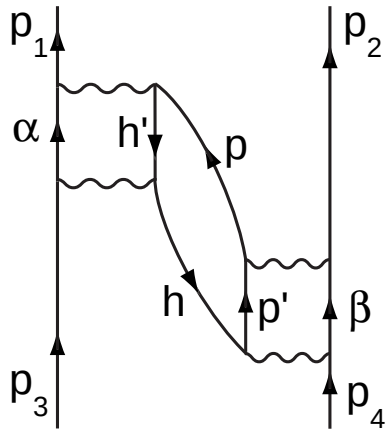

Figure 5.1: The 4$^{\text{th}}$ order diagram calculated in the text below.

and the perturbed Hamiltonian is then

$$H_1 = V_{NN} - U \tag{5.6}$$

so that

$$H = H_0 + H_1. \tag{5.7}$$

There are d energy eigenvalues calculated with respect to the binding energy E_0^c of the closed core. The question is how to compute $H_{eff} = H_0 + V_{eff}$. One method is the folded diagram expansion in which the effective interaction V_{eff} is calculated from

$$V_{\text{eff}} = \hat{Q} - \hat{Q}' \int \hat{Q} + \hat{Q}' \int \hat{Q} \int \hat{Q} - \cdots , \tag{5.8}$$

where $\hat{Q}$ is the irreducible *pp* vertex function consisting of valence-linked irreducible diagrams, and $\hat{Q}'$ is obtained by removing from $\hat{Q}$ all terms that are first order in the perturbing potential. This folded diagram series can be summed to all orders with the Lee-Suzuki iteration method as discussed in [123]. Therefore, the problem is reduced to calculating the irreducible *pp* vertex function. In most studies one sums the terms in this series order by order, but our aim is to develop a formalism for including an infinite number of core polarization diagrams in the *pp* vertex function.

To best illustrate the techniques involved in these types of diagrammatic calculations, we begin by explicitly calculating the fourth order core polarization diagram shown in Fig. 5.1 that could be included in $\hat{Q}$, if so desired. Although many of the diagram rules used in this brief derivation will not ap-

pear explicitly in the discussion of our all-order method, we strictly adhere to them in our calculations, and all details can be found in Ref. [134]. In the uncoupled angular momentum representation, the diagram shown in Fig. 5.1 is given by

$$\text{diag. } 1 = \frac{(-1)^3}{2^0} \sum_{ph} \frac{\langle p_1 h \mid L_{ph} \mid p_3 p \rangle \langle p p_2 \mid L_{pp} \mid h p_4 \rangle}{(\epsilon_3 + \epsilon_4) - (\epsilon_3 - \epsilon_h + \epsilon_p + \epsilon_2)}, \tag{5.9}$$

where the sum is over all intermediate particle-hole states and L_{pp} and L_{ph} represent the two-interaction ladders to be discussed shortly. In this uncoupled representation, we have the phase factors, energy denominators, and matrix element form, but when the initial and final states are coupled to some given angular momentum, we must include the proper coupling factors. To determine these factors, we take the initial diagram in which the incoming and outgoing states are coupled to definite J and T values and cut the ph pair to get the new couplings as shown in Fig. 5.2. Applying the diagram rules for this coupling, we have

$$\begin{aligned} \text{diag. } 1 \;=\; & \sum_{ph} \frac{1}{(\epsilon_3 + \epsilon_4) - (\epsilon_3 - \epsilon_h + \epsilon_p + \epsilon_2)} \hat{J}^{-1} \hat{T}^{-1} \\ & \times \sum_{J'T'} X \begin{pmatrix} p_3 & p_4 & J \\ p_1 & p_2 & J \\ J' & J' & 0 \end{pmatrix} X \begin{pmatrix} \frac{1}{2} & \frac{1}{2} & T \\ \frac{1}{2} & \frac{1}{2} & T \\ T' & T' & 0 \end{pmatrix} \\ & \times \hat{J}' \hat{T}' \langle p_1 h \mid L_{ph} \mid p_3 p \rangle \langle p p_2 \mid L_{pp} \mid h p_4 \rangle, \end{aligned} \tag{5.10}$$

where $\hat{A} = \sqrt{2A+1}$ and the X-coefficient is defined in terms of the 6-j symbol as follows

$$X \begin{pmatrix} i & j & x \\ k & l & x \\ y & y & 0 \end{pmatrix} = \hat{x}\hat{y}(-1)^{j+x+k+y} \begin{Bmatrix} i & j & x \\ l & k & y \end{Bmatrix}.$$

To continue, further cuts must be made to evaluate the L_{pp} and the L_{ph} terms, as shown in Figs. 5.3 and 5.4, where each gives two cross-coupled matrix elements. With the appropriate angular momentum coupling coefficients, the final step in evaluating this diagram is the calculation of the cross-coupled

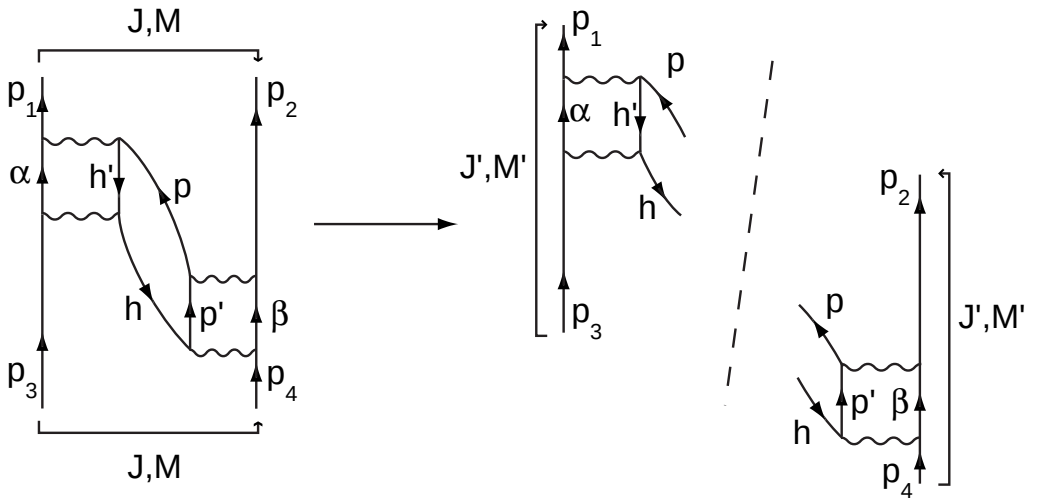

Figure 5.2: This fourth-order core polarization diagram can be factorized by performing the "cut" shown here and applying the appropriate angular momentum recouplings.

matrix elements that result, where, for example

$$\langle \overset{\downarrow}{p_1} \overset{}{h} \overset{\uparrow}{} \mid V \mid \overset{J'\rceil}{p_3} \overset{}{p} \overset{}{} \overset{}{} \overset{J'\rfloor}{} \rangle = \hat{J'}^{-1}\hat{T'}^{-1} \sum_{J''T''} \hat{J''}\hat{T''} X \begin{pmatrix} p_3 & p_1 & J' \\ p & h & J' \\ J'' & J'' & 0 \end{pmatrix} X \begin{pmatrix} \frac{1}{2} & \frac{1}{2} & T' \\ \frac{1}{2} & \frac{1}{2} & T' \\ T'' & T'' & 0 \end{pmatrix}$$
$$\times \langle p_1 h J'' M \mid V \mid p_3 p J'' M \rangle.$$

Now that we have seen how to calculate the second-order core polarization diagram, we turn to our attention to a non-perturbative all-order approach. The diagram in Fig. 5.5 illustrates the key features that the all-order method should capture, though it is obviously too complicated to calculate explicitly. As indicated in the figure, *pp* and *ph* vertex corrections in addition to general *pp* and *ph* corrections deeper in the diagram should all be generated including the bubble-inside-bubble structures.

The KBB induced interaction approach provides a very appealing way for summing up planar diagrams to all orders. Its fundamental requirement is that the irreducible vertex functions be calculated self-consistently. This means that any core polarization term contained in a vertex function must be generated self-consistently from the same vertex function. We note that it is this requirement which plays the essential role of generating CP diagrams to all orders. To see this point, it may be convenient to first consider the

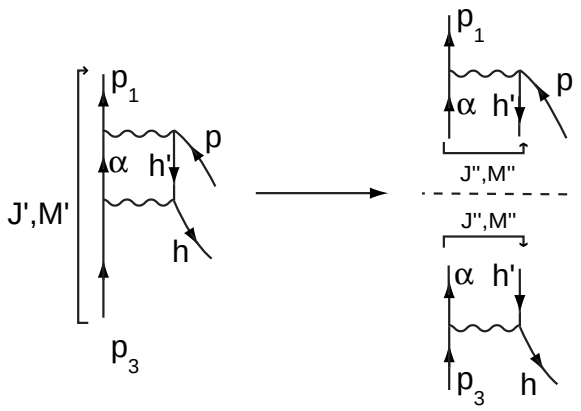

Figure 5.3: Further "cutting" that is needed to calculate the L_{ph} term.

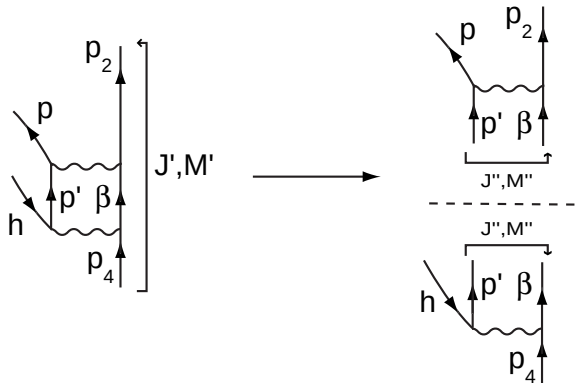

Figure 5.4: Further "cutting" that is needed to calculate the L_{pp} term.

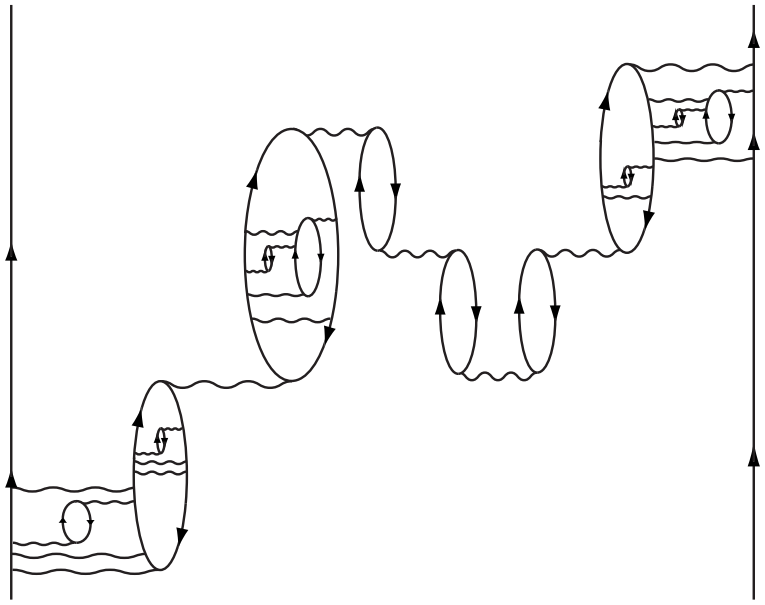

Figure 5.5: An example of the type of core polarization diagram our iteration method will include.

particle-hole (ph) vertex function f. (We shall consider the particle-particle vertex a little later.) As shown in Fig. 5.6, f is generated by summation of the driving term V and core polarization terms, the latter being dependent on f. This then gives the self-consistent equation for f

$$f = V + \Sigma g_{ph} \Sigma + \Sigma g_{ph} f g_{ph} \Sigma + \Sigma g_{ph} f g_{ph} f g_{ph} \Sigma + \cdots , \tag{5.11}$$

where g_{ph} is the free ph Green function, and Σ denotes the vertex for particle-core and hole-core coupling. The second-order CP diagram of Fig. 5.6 is the lowest-order term contained in $\Sigma g_{ph} \Sigma$. We note that for simplicity the bra and ket indices have been suppressed in the above equation as well as the equations that follow. For example, in Eq. (5.6) the f on the LHS represents $\langle 12^{-1}|f|34^{-1}\rangle$, while the fifth and sixth Σ's on the RHS represent $\langle 1ph^{-1}|\Sigma|3\rangle$ and $\langle 2^{-1}|\Sigma|p'h'^{-1}4^{-1}\rangle$, respectively.

The generation of high-order CP diagrams may be seen easily for the special case $\Sigma = V$. In this case Eq. (5.11) becomes

$$f = V + V g_{ph} V + V g_{ph} f g_{ph} V + V g_{ph} f g_{ph} f g_{ph} V + \cdots . \tag{5.12}$$

Since f appears on both sides of this equation, it is clear that an iterative solution for f will yield core polarization diagrams to all orders, including those with "bubbles inside bubbles," like those shown in diagram (a) of Fig. 5.8.

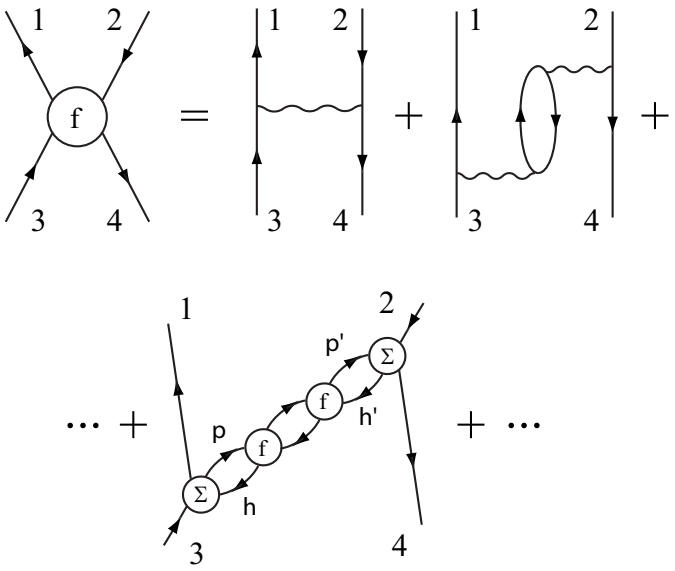

Figure 5.6: Self-consistent diagrammatic expansion of the *ph* vertex function, f, where Σ is defined in the text.

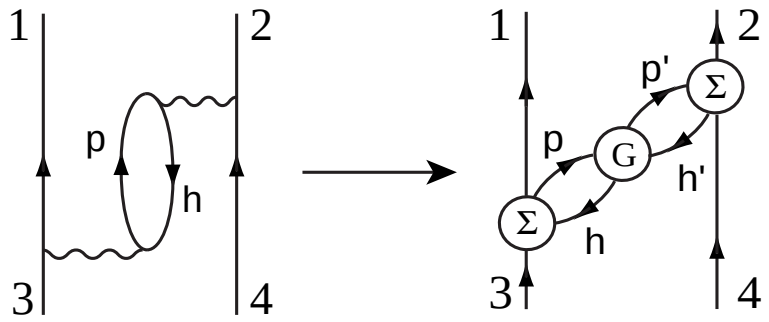

Figure 5.7: Structure of our generalization of the second-order diagram.

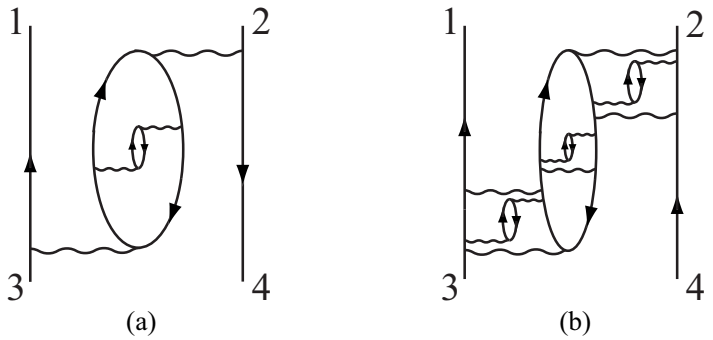

Figure 5.8: Higher-order terms contributing to the vertex functions f and Γ, including (a) nested bubbles in bubbles and (b) particle-core and hole-core couplings.

For nuclear many-body calculations in general, we also need the particle-particle (pp) vertex function Γ. Like f, Γ is given by a driving term plus core polarization terms. Furthermore, the diagrammatic representation of Γ is identical to Fig. 5.6 except that the hole lines 2 and 4 are replaced by corresponding particle lines. This gives the self-consistent equation for Γ

$$\Gamma = V + \Sigma g_{ph} \Sigma + \Sigma g_{ph} f g_{ph} \Sigma + \Sigma g_{ph} f g_{ph} f g_{ph} \Sigma + \cdots . \tag{5.13}$$

To clarify our compact notation, we note that the external lines of the Σ vertices in Γ are different than those shown in Fig. 5.6. The upper Σ vertex, for example, now represents $\langle 2|\Sigma|ph^{-1}4\rangle$. These different Σ vertices can be related to each other, however, via appropriate particle-hole transformations.

Finally, the vertex functions f and Γ are coupled together via the coupling vertex Σ. In the present work we choose

$$\begin{aligned} \Sigma &= V + \Sigma_{ph} + \Sigma_{pp}, \\ \Sigma_{ph} &= V g_{ph} V + V g_{ph} f g_{ph} V + V g_{ph} f g_{ph} f g_{ph} V + \cdots , \\ \Sigma_{pp} &= V g_{pp} V + V g_{pp} \Gamma g_{pp} V + V g_{pp} \Gamma g_{pp} \Gamma g_{pp} V + \cdots \end{aligned} \tag{5.14}$$

where g_{pp} is the free pp Green function.

The self-consistent vertex functions f and Γ are determined from Eqs. (5.11) and (5.13–5.14). These are similar to the equations used by Kirson [124, 125], except that our Σ includes both Σ_{ph} and Σ_{pp}, while the equivalent term in Kirson's calculations only includes Σ_{ph} [124, 125, 135]. To see the role of the Σ vertices, let us consider diagram (b) of Fig. 5.8. Here the lower particle-core vertex, which contains repeated particle-particle interactions, belongs to

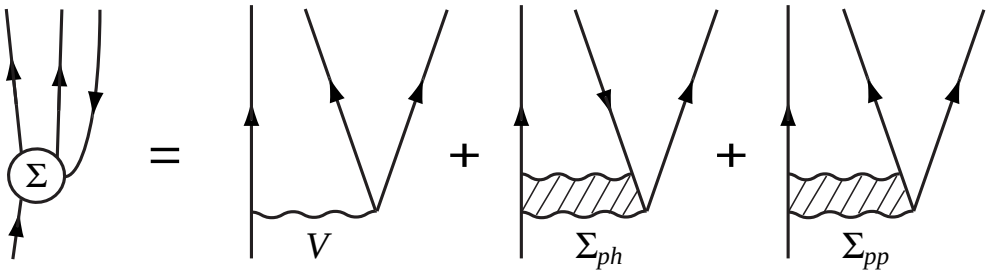

Figure 5.9: Diagrammatic representation of the coupling vertex Σ.

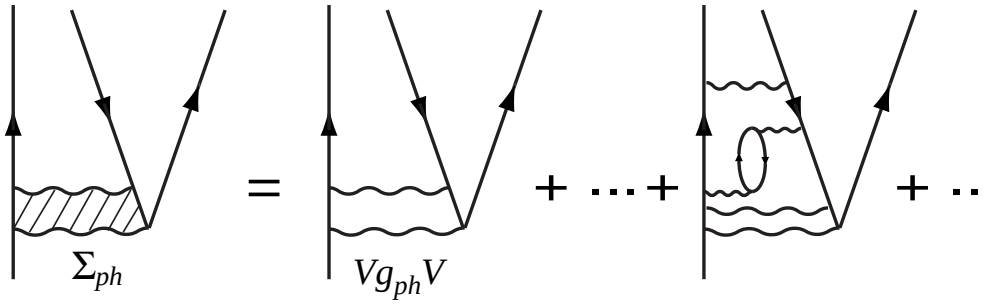

Figure 5.10: Some typical diagrammatic contributions to the *ph* coupling vertex Σ_{ph}.

Σ_{pp}, while the upper one, which contains repeated particle-hole interactions, belongs to Σ_{ph}. It is, of course, necessary to include Σ_{pp} in order to have such CP diagrams in the all-order sum. Our equations are equivalent to those of Kirson when Σ_{pp} is set to zero, and in this case Γ does not enter the calculation of f.

Solving the above equations for f and Γ may seem complicated, but we have found their solution can be simplified significantly through use of the true *ph* and *pp* Green functions

$$\begin{aligned} G_{ph} &= g_{ph} + g_{ph} f G_{ph}, \\ G_{pp} &= g_{pp} + g_{pp} \Gamma G_{pp}. \end{aligned} \tag{5.15}$$

Using these Green functions to partially sum and regroup our series, the self-consistent Eqs. (5.11) and (5.13–5.14) assume a much simpler form

$$\begin{aligned} f &= V + \Sigma G_{ph} \Sigma, \\ \Gamma &= V + \Sigma G_{ph} \Sigma, \\ \Sigma &= V + V G_{ph} V + V G_{pp} V. \end{aligned} \tag{5.16}$$

The above simplifications also aid our numerical efforts, and using the following iterative method we find our coupled equations can be solved rather efficiently. For the n^{th} iteration, we start from $f^{(n)}$ and $\Gamma^{(n)}$, to first calculate $G_{ph}^{(n)}$ and $G_{pp}^{(n)}$ followed by $\Sigma^{(n)}$, as seen from Eqs. (5.15)-(5.16). The vertex functions for the subsequent iteration are then obtained by taking $f^{(n+1)} = V + \Sigma^{(n)} G_{ph}^{(n)} \Sigma^{(n)}$ and $\Gamma^{(n+1)} = V + \Sigma^{(n)} G_{ph}^{(n)} \Sigma^{(n)}$. The entire iterative process begins from the initial $f^{(0)} = V + V g_{ph} V$ and $\Gamma^{(0)} = V + V g_{ph} V$, and typically converges after just a few iterations.

In the present work, we have included folded diagrams to all orders. As detailed in [17], we use this method to reduce the full-space nuclear many-body problem $H\Psi_n = E_n \Psi_n$ to a model space problem $H_{\rm eff}\chi_m = E_m \chi_m$, where $H = H_0 + V$, $H_{\rm eff} = H_0 + V_{\rm eff}$ and V denotes the bare NN interaction. The effective interaction $V_{\rm eff}$ is given by the folded-diagram expansion

We consider the effective interactions for valence nucleons, and in this case $\hat{Q}$ is the irreducible *pp* vertex function which we shall calculate using the KBB equations. In Ref. [124, 125], the effect of higher order CP diagrams to the non-folded $\hat{Q}$ term was extensively studied. In the present work, we first calculate $\hat{Q}$ including CP diagrams to all orders. Then the above folded diagram series for $V_{\rm eff}$ is summed to all orders using the Lee-Suzuki iteration method as discussed in Ref. [123]. In this way, folded CP diagrams are included to all orders.

For the present calculation we have chosen to use the low-momentum nucleon-nucleon interaction, $V_{\rm low-k}$. Since the vertex functions f and Γ both depend on the starting energy, there would be off-energy-shell effects present in many CP diagrams if the G-matrix interaction were chosen. This would make the calculation very complicated. $V_{\rm low-k}$, on the other hand, is energy independent so no such difficulties are encountered. Since detailed treatments of $V_{\rm low-k}$ have been given elsewhere [14, 15, 57, 73, 75, 130, 131], here we provide only a brief description. We define $V_{\rm low-k}$ through the T-matrix equivalence $T(p', p, p^2) = T_{\rm low-k}(p', p, p^2);\ (p', p) \leq \Lambda$ where T is given by the full-space equation $T = V_{NN} + V_{NN} g T$ while $T_{\rm low-k}$ by the model-space (momenta $\leq \Lambda$) equation $T_{\rm low-k} = V_{\rm low-k} + V_{\rm low-k} g T_{\rm low-k}$. Here V_{NN} represents some realistic NN potential and Λ is the decimation momentum beyond which the high-momentum components of V_{NN} are integrated out. $V_{\rm low-k}$ preserves both the deuteron binding energy and the low-energy scattering phase shifts of V_{NN}. Since empirical nucleon scattering phase shifts are available only up to the pion production threshold ($E_{lab} \sim 350$ MeV), beyond this momentum the realistic NN potentials cannot be uniquely determined. Accordingly, we choose $\Lambda \approx 2.0$ fm^{-1} thereby retaining only the information from a given potential that is constrained by experiment. In fact for this Λ, the $V_{\rm low-k}$ derived from

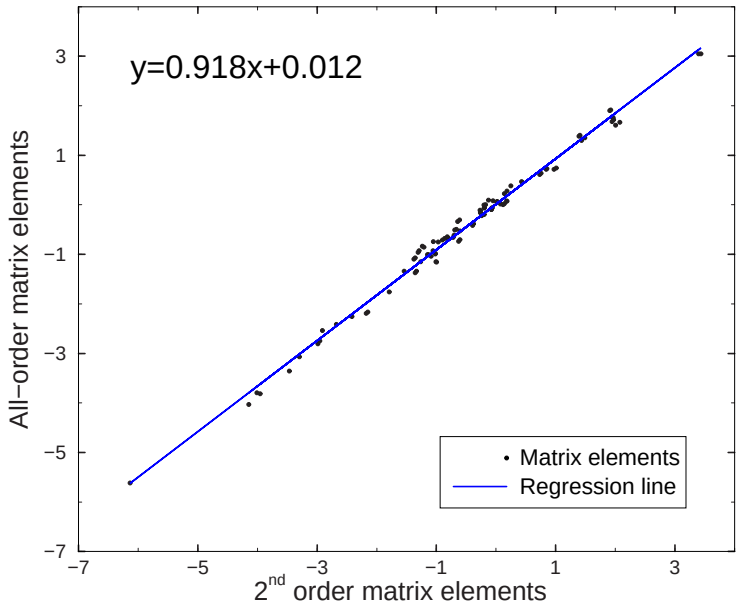

Figure 5.11: A comparison of the second-order core polarization matrix elements with those of the all-order KBB calculation.

various NN potentials [6, 8–10] are all nearly identical [14]. Except where noted otherwise, in our calculations we employ the $V_{\mathrm{low-k}}$ derived from the CD-Bonn potential [9].

5.3 Results and discussion

As an initial study, we have carried out a restricted all-order CP calculation for the *sd*-shell effective interactions. In particular, we sum only the TDA diagrams for the Green functions G_{pp} and G_{ph}, leaving a study of RPA diagrams to a future publication. We have used two choices for the shell model space: one with 4 shells (10 orbits from $0s_{1/2}$ to $1p_{1/2}$) and the other with 5 shells (15 orbits from $0s_{1/2}$ to $3s_{1/2}$), both with oscillator constant $\hbar\omega$=14 MeV. Only core excitations within this space are included. Vary, Sauer and Wong [136] have pointed out that for CP diagrams one needs to include intermediate states of high excitation energies (up to $\sim 10\hbar\omega$) in order for the second-order core polarization term to converge. In their work a G-matrix derived from the Reid soft-core potential was used, and our use of V_{low-k} may yield different results as it has greatly reduced high-momentum components. We have found that the difference between our five-shell and four-shell calculations was minimal;

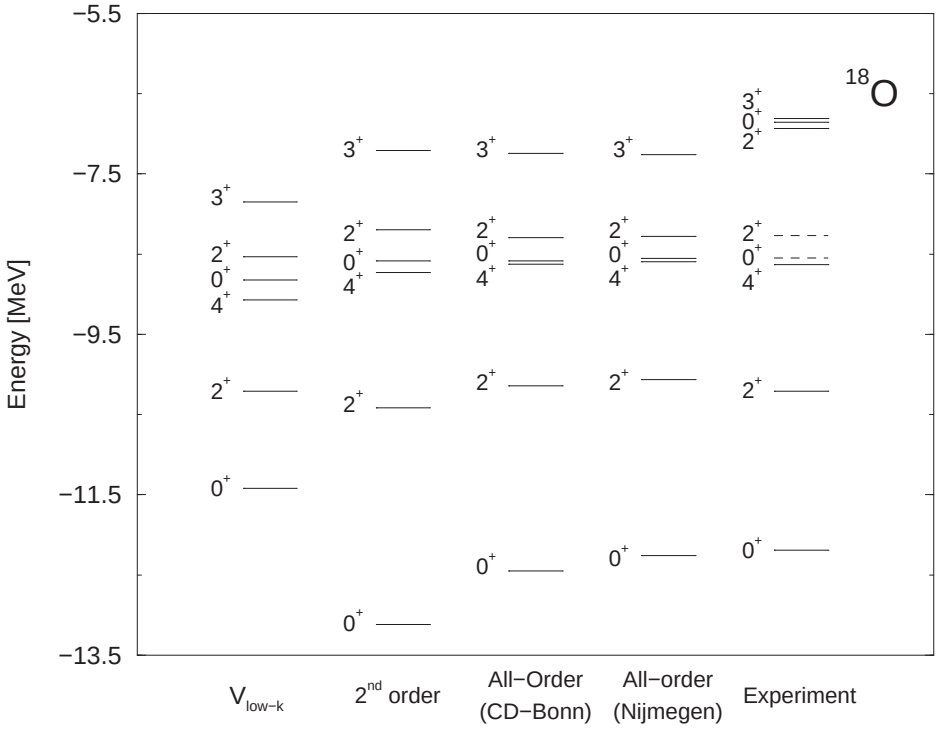

Figure 5.12: Spectra for the ^{18}O system calculated to different orders in perturbation theory. Dashed lines indicate levels with large intruder state mixing, and all calculations were performed using the experimental single particle energies of ^{17}O.

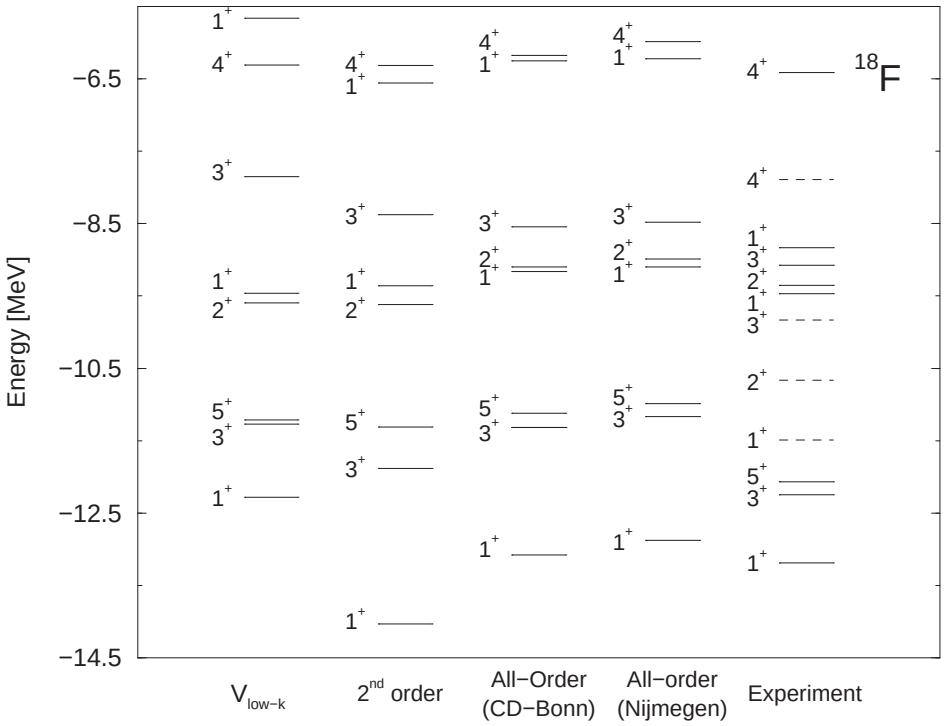

Figure 5.13: Spectra for the ^{18}F system calculated to different orders in perturbation theory. See the caption to Fig. 5.12 for details.

the results differing by about 2% or less. This finding is supported by recent studies which show desirable convergence properties of $V_{\mathrm{low-k}}$ [79]. We plan to study this convergence problem for $V_{\mathrm{low-k}}$ in the near future.

With these restrictions, we have calculated V_{eff} from Eqs. (5.15)-(5.16). A large number of angular momentum recouplings are involved in calculating the CP diagrams. In this regard, we have followed closely the diagram rules in [134]. Previous second-order calulations [15, 123] included in the $\hat{Q}$-box the first-order *pp* diagram, the second-order *pp* and *hh* ladder diagrams, and the second-order CP diagram. Our all-order calculation includes these same diagrams except the second-order CP diagram is replaced with the all-order CP diagrams from KBB. In Fig. 5.11 we compare the *sd*-shell V_{eff} matrix elements calculated from the second-order and all-order $\hat{Q}$-boxes just described, both using the 5-shell space mentioned above. A least-squares fit was applied to the data, and it is apparent that the effect of including CP to all orders in our calculation is a mild suppression of the second-order contributions. This conclusion is further born out in the calculation of the ^{18}O and ^{18}F spectra, the results of which are shown in Figs. 5.12 and 5.13. Here we observe a weak suppression of the second-order effects in ^{18}O but a moderate suppression in ^{18}F. In the same figures we also observe that the spectra for different $V_{\mathrm{low-k}}$ derived from the CD-Bonn and Nijmegen bare potentials are nearly identical.

5.4 Conclusion

In summary, we have presented a method based on the KBB induced interaction formalism for efficiently summing core polarization diagrams to all orders in perturbation theory. This summation is carried out by way of the KBB self-consistent equations whose solution is significantly simplified by the use of the true *pp* and *ph* Green functions, and by the use of the energy-independent $V_{\mathrm{low-k}}$. Although our calculation was restricted in several important aspects, we find that our final renormalized interaction is remarkably close to that of second-order perturbation theory. This is of practical importance and a welcoming result, for it allows one to use the results from a second-order calculation to approximate the contributions resulting from a large class of higher-order diagrams. In the future we intend both to expand our treatment by including additional diagrammatic contributions (RPA) and to generalize our method to study the all order CP effects for effective operators such as magnetic moment.

Chapter 6

The ^{14}C Dating Beta Decay with Brown-Rho-Scaled NN Interactions

6.1 Introduction

The application of density-dependent interactions to finite nuclei is more difficult than for nuclear matter. Whereas nuclear matter by definition has a uniform density, for finite nuclei the wavefunctions of the valence nucleons, which largely determine the properties of the nucleus, will be spread over a region with widely varying density. Moreover, shell model calculations are more reliable and practicable for few particles above and below closed shells (the latter can be treated with nucleon hole formalism). But just above a shell closure the nuclear density sampled by the valence nucleons will be too small for medium effects to be noticeable. Finally, as we have already discussed, realistic NN interactions are fine-tuned, especially with respect to the properties (masses and coupling constants) of the σ meson. Therefore, in order to make model-independent predictions for finite nuclei, we should attempt to find properties which are generally insensitive to how we scale the σ mass. As we now discuss, the beta decay of ^{14}C is a nearly perfect example for testing the hypothesis of Brown-Rho scaling.

The anomalously long beta decay lifetime of ^{14}C has long been an important test for low energy nuclear structure models. The nuclear transition matrix element is very small ($\simeq 2 \times 10^{-3}$), and is expected to result from an accidental cancellation among the different components contributing to the transition amplitude. This decay has therefore been used to investigate phenomena not normally considered in studies of allowed transitions, such as

Transition	End-Point Energy	Lifetime
$^{11}\mathrm{C} \rightarrow {}^{11}\mathrm{B} + e^+ + \nu_e$	1.98 MeV	20.4 min
$^{13}\mathrm{N} \rightarrow {}^{13}\mathrm{C} + e^+ + \nu_e$	2.20 MeV	10.0 min
$^{14}\mathrm{O} \rightarrow {}^{14}\mathrm{N} + e^+ + \nu_e$	5.14 MeV	1.18 min
$^{15}\mathrm{O} \rightarrow {}^{15}\mathrm{N} + e^+ + \nu_e$	2.75 MeV	2.04 min
$^{14}\mathrm{C} \rightarrow {}^{14}\mathrm{N} + e^- + \bar{\nu}_e$	0.156 MeV	2×10^9 min

Table 6.1: Typical half-lives of allowed transitions in p-shell nuclei. Data obtained from [142].

meson exchange currents [137, 138], relativistic effects [139], and configuration mixing [140, 141]. More importantly, the suppressed Gamow-Teller strength is a challenge for models of the in-medium nuclear interaction and in particular for the current program to extend the microscopic description of the nuclear force beyond that of a static two-body potential fit to the experimental data on two-nucleon systems. The connection between this decay and the radiocarbon dating method, whose importance for all of science can hardly be exaggerated, makes this problem of broad interest even beyond nuclear physics.

A priori one would not expect ^{14}C, which beta decays to the ^{14}N ground state, to be a good isotope for radiocarbon dating over archaeological times because the quantum numbers of the initial and final states, $(J_i^\pi, T_i) = (0^+, 1)$ and $(J_f^\pi, T_f) = (1^+, 0)$, satisfy the selection rules for an allowed Gamow-Teller transition. The expected half-life would therefore be on the order of hours as shown in Table 6.1, far from the unusually long value of 5730 years [142] observed in nature. In fact, the ^{14}O transition would be suppressed as well, except that there exists an additional decay mode to the 2.31 MeV 0^+ excited state of ^{14}N. The decay of ^{14}O to the ^{14}N ground state was studied in [143]. Although nearly two orders of magnitude shorter, the half-life of this transition was found to also be highly suppressed.

In this chapter, we suggest that a large part of the suppression arises from in-medium modifications to the nuclear interaction. Such contributions include three-nucleon forces, which have been tested in *ab initio* nuclear structure calculations of light nuclei [144, 145], or hadronic medium modifications in which the masses of nucleons and mesons are altered at finite density due to either many-body interactions [35, 146] or the partial restoration of chiral symmetry at finite density [38, 147, 148]. In fact, three-nucleon forces and hadronic medium modifications are not unrelated, for they both parameterize the effects of missing degrees of freedom, such as resonance-hole excitations and virtual nucleon-antinucleon excitations. We study the problem of the ^{14}C

beta decay from the perspective of Brown-Rho scaling (BRS) [45, 56], which was the first model to make a comprehensive prediction for hadronic masses in medium. In BRS the masses of nucleons and most light mesons (except the pion whose mass is protected by its Goldstone boson nature) decrease at finite density as the ratio of the in-medium to free-space pion decay constant:

$$\sqrt{\frac{g_A}{g_A^*}}\frac{m_N^*}{m_N} = \frac{m_\sigma^*}{m_\sigma} = \frac{m_\rho^*}{m_\rho} = \frac{m_\omega^*}{m_\omega} = \frac{f_\pi^*}{f_\pi} = \Phi(n), \tag{6.1}$$

where g_A is the axial coupling constant, Φ is a function of the nuclear density n with $\Phi(n_0) \simeq 0.8$, and the star indicates in-medium values of the given quantities. Since all realistic models of the NN interaction are based on meson exchange and fit to only free-space data, Eq. (6.1) prescribes how to construct a density-dependent nuclear interaction that accounts for hadronic medium modifications. This program has been carried out in several previous studies of symmetric nuclear matter [80, 84], where it was found that one could well describe saturation and several bulk equilibrium properties of nuclear matter use such Brown-Rho-scaled NN interactions.

The case of the ^{14}C beta decay provides a nearly ideal situation in nuclear structure physics for testing the hypothesis of Brown-Rho scaling. Just below a double shell closure, the valence nucleons of ^{14}C will inhabit a region with a large nuclear density. But more important is the sensitivity of this GT matrix element to the nuclear tensor force, which as articulated by Zamick and collaborators [149, 150] is one of the few instances in nuclear structure where the role of the tensor force is clearly revealed. In fact, with a residual interaction consisting of only central and spin-orbit forces it is not possible to achieve a vanishing matrix element in a pure p^{-2} configuration [151]. Jancovici and Talmi [152] showed that by including a strong tensor force one could construct an interaction which reproduces the lifetime of ^{14}C as well as the magnetic moment and electric quadrupole moment of ^{14}N, although agreement with the known spectroscopic data was unsatisfactory.

The most important contributions to the tensor force come from π and ρ meson exchange, which act opposite to each other:

$$V_\rho^T(r) = \frac{f_{N\rho}^2}{4\pi} m_\rho \tau_1 \cdot \tau_2 \left(-S_{12} \left[\frac{1}{(m_\rho r)^3} + \frac{1}{(m_\rho r)^2} + \frac{1}{3 m_\rho r} \right] e^{-m_\rho r} \right), \tag{6.2}$$

$$V_\pi^T(r) = \frac{f_{N\pi}^2}{4\pi} m_\pi \tau_1 \cdot \tau_2 \left(S_{12} \left[\frac{1}{(m_\pi r)^3} + \frac{1}{(m_\pi r)^2} + \frac{1}{3 m_\pi r} \right] e^{-m_\pi r} \right). \tag{6.3}$$

Since the ρ meson mass is expected to decrease substantially at nuclear matter density while the π mass remains relatively constant, an unambiguous prediction of BRS is the decreasing of the tensor force at finite density, which should be clearly seen in the GT matrix element. In fact, recent shell model calculations [153] performed in a larger model space consisting of $p^{-2} + 2\hbar\omega$ excitations have shown that the β-decay suppression requires the in-medium tensor force to be weaker and the in-medium spin-orbit force to be stronger in comparison to a typical G-matrix calculation starting with a realistic NN interaction. As originally shown in Chapter 4, in Fig. 6.1 we plot the radial part of the tensor interaction $V^T(r) = V^T_\pi(r) + V^T_\rho(r)$ at zero density and nuclear matter density assuming that $m^*_\rho(n_0)/m_\rho = 0.80$.

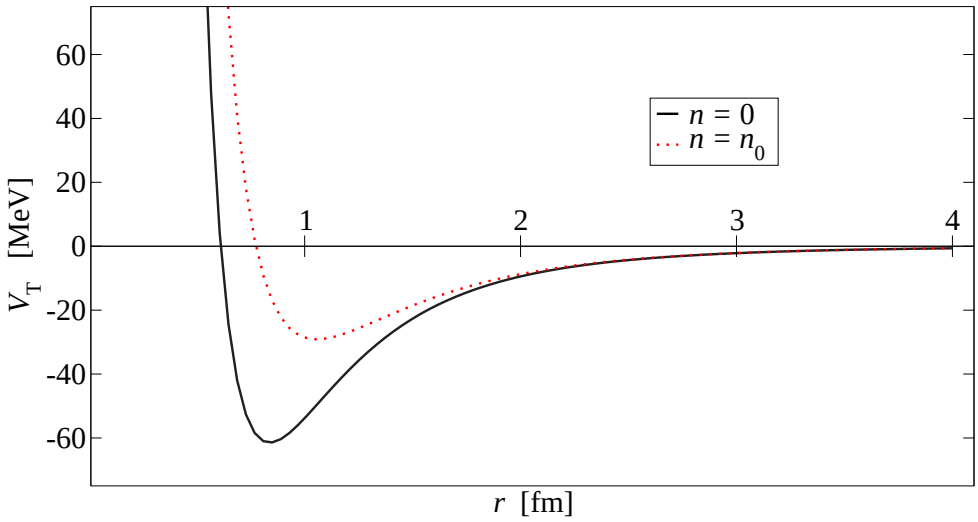

Figure 6.1: The radial part of the nuclear tensor force given in Eqs. (6.2) and (6.3) from π and ρ meson exchange at zero density and nuclear matter density under the assumption of BRS.

6.2 Medium-modified Bonn-B potential

In Chapter 1 we have already reviewed the experiments designed to study the properties of hadrons in medium directly. However, we suggest the possibility that normal nuclei can give evidence – although perhaps indirect – for these medium modifications. In particular, our present study may test the decrease in ρ mass more simply.

Today there are a number of high precision NN interactions based solely on one-boson exchange. In the present work we use the Bonn-B potential

[68] which includes the exchange of the π, η, σ, a_0, ρ, and ω mesons. In [84] the consequences of BRS on the free-space NN interaction were incorporated into the Bonn-B potential and shown to reproduce the saturation properties of nuclear matter in a Dirac-Brueckner-Hartree-Fock calculation. The masses of the pseudoscalar mesons were unchanged, and the vector meson masses as well as the corresponding form factor cutoffs were decreased according to

$$\frac{m_\rho^*}{m_\rho} = \frac{m_\omega^*}{m_\omega} = \frac{\Lambda^*}{\Lambda} = 1 - 0.15\frac{n}{n_0}. \tag{6.4}$$

The medium-modified (MM) Bonn-B potential is unique in its microscopic treatment of the scalar σ particle as correlated 2π exchange. In [84] it was shown that scaling the σ meson as in Eq. (6.1) led to a NN interaction that was much too attractive at large densities. This was observed in their calculations of the binding energy of symmetric nuclear matter, which saturated at much too high a density. To overcome this difficulty, it was suggested that the σ meson be replaced by a pair of pions coupled to a $J^\pi = 0^+$ state. This can be calculated from dispersion relations together with the experimental results from πN and $\pi\pi$ phase shift data as discussed in [154]. Their model for the pionic interaction $V_{\pi\pi}$ is shown in Fig. 6.2. It includes the exchange of various mesons, and is coupled to the $K\bar{K}$ interaction. From $V_{\pi\pi}$ one can calculate the T-matrix for $\pi\pi$ scattering

$$T_{\pi\pi} = V_{\pi\pi} + V_{\pi\pi} G_{\pi\pi} M_{\pi\pi}, \tag{6.5}$$

where medium modifications are induced both in changes to the 2π propagator $M_{\pi\pi}$ and to the $\pi\pi$ interaction. The latter is altered by the scaling of the ρ meson mass and form factor cutoff. The $\pi\pi$ interaction is then used to calculate the $N\bar{N} \to \pi\pi \to N\bar{N}$ reaction. This is then related to the 2π exchange process in the NN channel through dispersion relations and crossing symmetry. Given this model for the medium-modified NN interaction, satisfactory results were obtained for the saturation of nuclear matter within the Dirac-Brueckner-Hartree-Fock formalism [84].

6.3 Formalism

One traditional difficulty associated with using realistic NN interactions in many-body perturbation theory is that the interaction for relative S states becomes strongly repulsive at short distances. The modern solution to this problem is to integrate out the high momentum components of the interaction in such a way that the low energy physics is preserved. The details

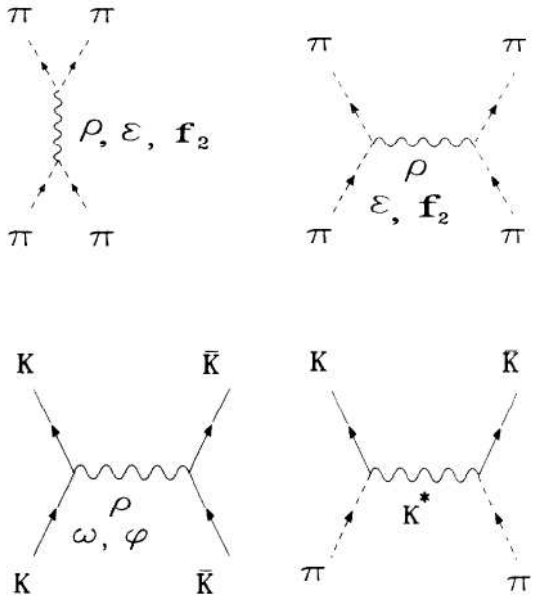

Figure 6.2: The $\pi\pi$ interaction calculated from the exchange of various mesons. Figure reproduced from [154].

for constructing such a low momentum interaction, $V_{\mathrm{low}-k}$, are described in [15, 155]. We define $V_{\mathrm{low-k}}$ through the T-matrix equivalence $T(p', p, p^2) = T_{\mathrm{low-k}}(p', p, p^2)$ for $(p', p) \leq \Lambda$, where T is given by the full-space equation $T = V_{NN} + V_{NN}gT$ and $T_{\mathrm{low-k}}$ by the model-space (momenta $\leq \Lambda$) equation $T_{\mathrm{low-k}} = V_{\mathrm{low-k}} + V_{\mathrm{low-k}}gT_{\mathrm{low-k}}$. Here V_{NN} represents the Bonn-B NN potential and Λ is the decimation momentum beyond which the high-momentum components of V_{NN} are integrated out. Since pion production starts around $E_{\mathrm{lab}} \simeq 300$ MeV, the concept of a real NN potential is not valid beyond that energy. Consequently, we choose $\Lambda \approx 2.0$ fm^{-1} thereby retaining only the information from a given potential that is constrained by experiment. In fact for this Λ, the $V_{\mathrm{low-k}}$ derived from various NN potentials are all nearly identical [155].

We use the folded diagram formalism to reduce the full-space nuclear many-body problem

$$H\Psi_n = E_n\Psi_n \tag{6.6}$$

to a model space problem

$$H_{\mathrm{eff}}\chi_m = E_m\chi_m \tag{6.7}$$

as detailed in [17]. Here

$$H = H_0 + V \quad \text{and} \quad H_{\text{eff}} = H_0 + V_{\text{eff}} \tag{6.8}$$

where $E_n = E_n(A = 14) - E_0(A = 16, \text{core})$, and V denotes the bare NN interaction. The effective interaction V_{eff} is derived following closely the folded-diagram method detailed in [123]. A main difference is that in the present work the irreducible vertex function ($\hat{Q}$-box) is calculated from the low-momentum interaction $V_{\text{low}-k}$, while in [123] from the Brueckner reaction matrix (G-matrix). In the $\hat{Q}$-box we include hole-hole irreducible diagrams of first- and second-order in $V_{\text{low}-k}$as shown in Fig. 6.3. Previous studies [65, 79, 156] have

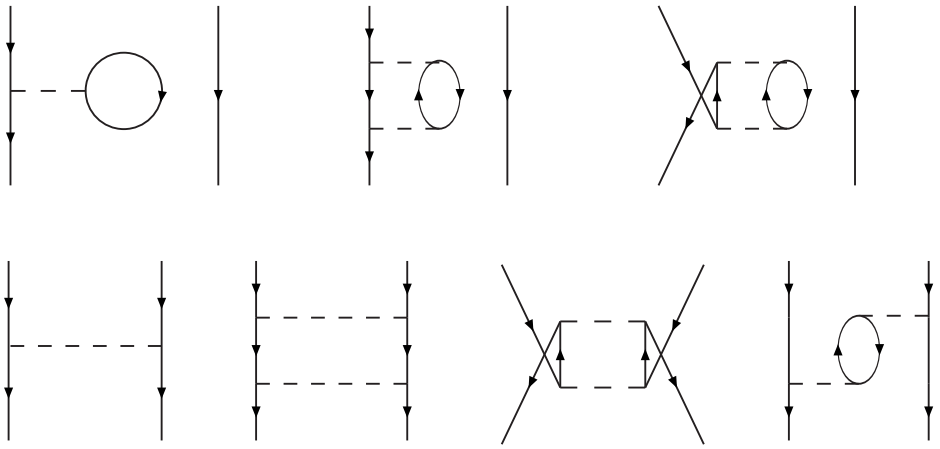

Figure 6.3: Diagrams contributing to the $\hat{Q}$-box in our calculation of the effective interaction V_{eff}.

found that $V_{\text{low}-k}$ is suitable for perturbative calculations; in all of these references satisfactory converged results were obtained including terms only up to second order in $V_{\text{low}-k}$.

Our calculation was carried out in jj-coupling where in the basis $\left\{p_{1/2}^{-2}, p_{1/2}^{-1}p_{3/2}^{-1}, p_{3/2}^{-2}\right\}$ one must diagonalize

$$\left[V_{\text{eff}}^{ij}\right] + \begin{bmatrix} 0 & 0 & 0 \\ 0 & \epsilon & 0 \\ 0 & 0 & 2\epsilon \end{bmatrix}, \tag{6.9}$$

to obtain the ground state of ^{14}N (and a similar 2×2 matrix for ^{14}C). We used $\epsilon = \epsilon(p_{1/2}^{-1}) - \epsilon(p_{3/2}^{-1}) = 6.3$ MeV, which is the experimental excitation energy of the first $\frac{3}{2}^-$ state in ^{15}N. One can transform the wavefunctions to

LS-coupling, where the ^{14}C and ^{14}N ground states are

$$\begin{aligned} \psi_i &= x\left|^1S_0\right\rangle + y\left|^3P_0\right\rangle \\ \psi_f &= a\left|^3S_1\right\rangle + b\left|^1P_1\right\rangle + c\left|^3D_1\right\rangle \end{aligned} \tag{6.10}$$

and the Gamow-Teller matrix element $M_{\rm GT}$ is given by

$$\sum_k \langle\psi_f||\sigma(k)\tau_+(k)||\psi_i\rangle = -\sqrt{6}\left(xa - yb/\sqrt{3}\right). \tag{6.11}$$

For central and spin orbit forces only, the matrix element is equal to [151, 157]

$$M_{\rm GT} = -\sqrt{6}\left(1 + \frac{\langle^3S_1|\,V\,|^3S_1\rangle - \epsilon_1}{\langle^3P_0|\,V\,|^3P_0\rangle - \epsilon_2}\right), \tag{6.12}$$

where ϵ_1 and ϵ_2 are the ground state energies of ^{14}N and ^{14}C respectively. Since $\langle^3S_1|\,V\,|^3S_1\rangle > \epsilon_1$ and $\langle^3P_0|\,V\,|^3P_0\rangle > \epsilon_2$, the matrix element cannot vanish since the two terms inside the parentheses have the same sign. Therefore, with central and spin-orbit forces only, it is not possible to achieve a zero matrix element in a p^{-2} configuration. Since x and y are expected to have the same sign [151], the GT matrix element can vanish only if a and b have the same sign, which requires that the $\langle^3S_1|\,V_{\rm eff}\,|^3D_1\rangle$ matrix element furnished by the tensor force be large enough [152].

6.4 Calculation and results

In Table 6.2 we show the ground state wavefunctions of ^{14}C and ^{14}N, as well as the GT matrix element, calculated with the MM Bonn-B interaction.

n/n_0	x	y	a	b	c	$M_{\rm GT}$
0	0.844	0.537	0.359	0.168	0.918	-0.615
0.25	0.825	0.564	0.286	0.196	0.938	-0.422
0.5	0.801	0.599	0.215	0.224	0.951	-0.233
0.75	0.771	0.637	0.154	0.250	0.956	-0.065
1.0	0.737	0.675	0.103	0.273	0.956	0.074

Table 6.2: The coefficients of the LS-coupled wavefunctions defined in Eq. (6.10) and the associated GT matrix element as a function of the nuclear density n.

In Fig. 6.4 we plot the resulting $B(GT) = \frac{1}{2J_i+1}|M_{\rm GT}|^2$ values for tran-

sitions between the low-lying states of ^{14}C and the ^{14}N ground state for the in-medium Bonn-B NN interaction taken at several different densities. Recent experiments [158] have determined the GT strengths from the ^{14}N ground state to excited states of ^{14}C and ^{14}O using the charge exchange reactions ^{14}N$(d, ^2$He$)^{14}$C and ^{14}N$(^3$He$, t)^{14}$O, and our theoretical calculations are in good overall agreement. The most prominent effect we find is a robust inhibition of the ground state to ground state transition for densities in the range of $0.75 - 1.0n_0$. In contrast, the other transition strengths are more mildly influenced by the density dependence in BRS. In Fig. 6.5 we show the resulting half-life of ^{14}C calculated from the MM Bonn-B potential.

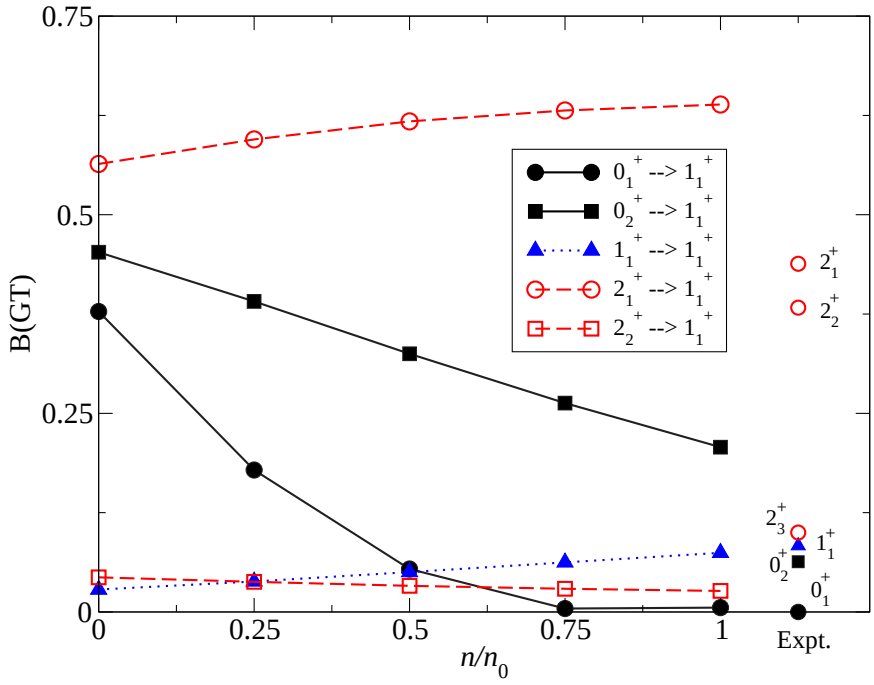

Figure 6.4: The $B(GT)$ values for transitions from the states of ^{14}C to the ^{14}N ground state as a function of the nuclear density and the experimental values from [158]. Note that there are three experimental low lying 2^+ states compared to two theoretical 2^+ states in the p^{-2} configuration.

The half-life goes as the inverse square of the Gamow-Teller matrix element

$$T_{1/2} = \frac{1}{f(Z, E_0)} \frac{2\pi^3\hbar^7}{m_e^5 c^4} \frac{\ln 2}{\left| \sum_{\mu M_f} < J_f M_f \xi | \boldsymbol{O}_{\lambda\mu}(\beta) | J_i M_i \zeta > \right|^2}, \tag{6.13}$$

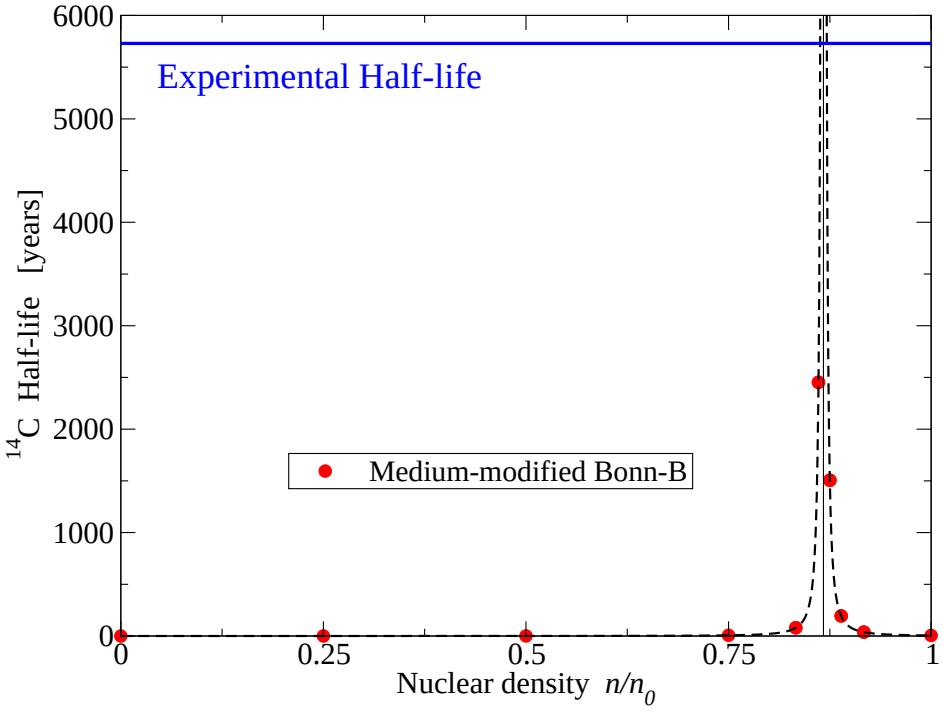

Figure 6.5: The half-life of ^{14}C calculated using the medium-modified Bonn-B potential.

where E_0 is the end-point energy (the maximum kinetic energy of the emitted electron) and $f(Z, E_0)$ is the Fermi integral defined by

$$f(Z, E_0) = \int F(Z, E_e) \left(\frac{p_e}{m_e c}\right)^2 \left(\frac{E_0 - E_e}{m_e c^2}\right)^2 \frac{dp_e}{m_e c}. \tag{6.14}$$

In (6.14) E_e is the kinetic energy of the emitted electron, and the Fermi function $F(Z, E_e)$ accounts for changes to the electron density of final states due to Coulomb effects from the nucleus. The Fermi integral $f(Z, E_0)$ must be evaluated numerically [159], and the dependence on Z and E_0 is plotted in Fig. 6.6 taken from [159]. For the β decay of ^{14}C, we find that $f(7, 0.156\text{MeV}) \simeq 0.006$. The small end-point energy of the decay (shown in Table 6.1) compared to other allowed transitions in p-shell nuclei helps to suppress the transition. However, this is not nearly sufficient to account for the observed lifetime. In order to obtain the anomalously long half-life of 5730 years, the GT matrix element must be $M_{GT} \simeq 2 \times 10^{-3}$.

The nuclear density experienced by a valence p-shell nucleon is close to

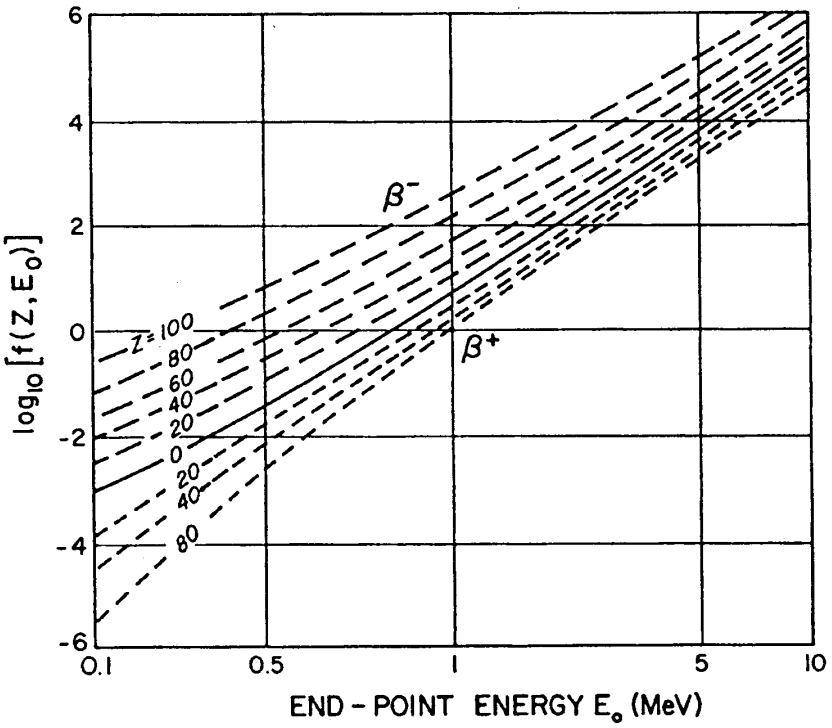

Figure 6.6: Plot of the Fermi integral as a function of the atomic mass Z and end-point energy E_0 for both β^- and β^+ decay. Figure reproduced from [159].

that of nuclear matter, as we show in Fig. 6.7. As an estimate of the nuclear density, we plot twice the charge distribution of ^{14}N obtained from electron scattering experiments (see [160, 161]) fit to the harmonic oscillator density distribution

$$n(r) \propto \left(1 + b\frac{r^2}{d^2}\right) e^{-r^2/d^2} \tag{6.15}$$

as well as the radial part of the $0p$ wavefunctions. The first excited 0^+ state of ^{14}N together with the ground states of ^{14}O and ^{14}C form an isospin triplet. The splitting in energy between this state and the ground state of ^{14}N is shown in Fig. 6.8, where the experimental value is 2.31 MeV.

In summary, we have shown that by incorporating hadronic medium modifications into the Bonn-B potential the decay of ^{14}C is strongly suppressed at densities close to that experienced by valence nucleons in ^{14}C. In a more traditional approach such medium modifications would be built in through phenomenological 3N forces, and we suggest that calculations with free-space

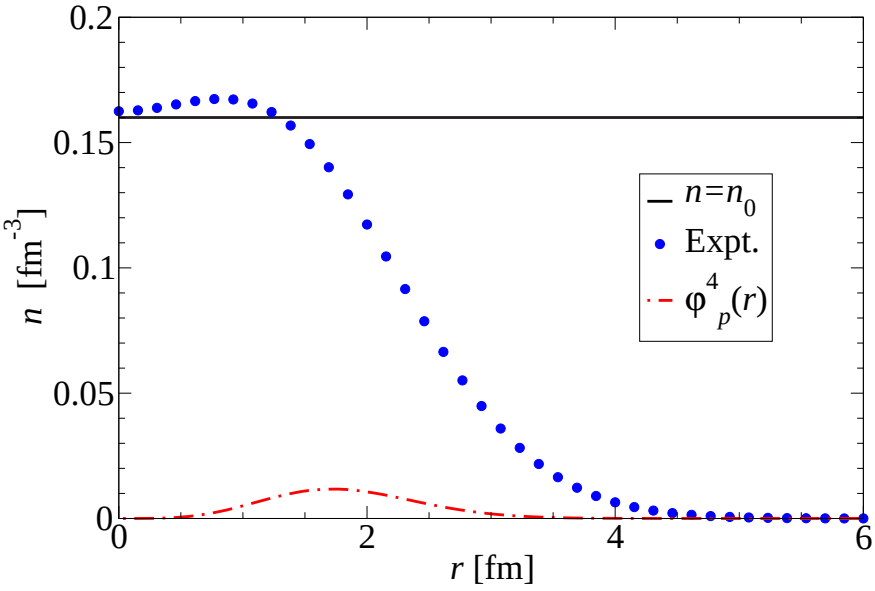

Figure 6.7: Twice the charge distribution of ^{14}N taken from [160,161] and the fourth power of the p-shell wavefunctions.

2N interactions supplemented with 3N forces should also inhibit the GT transition.

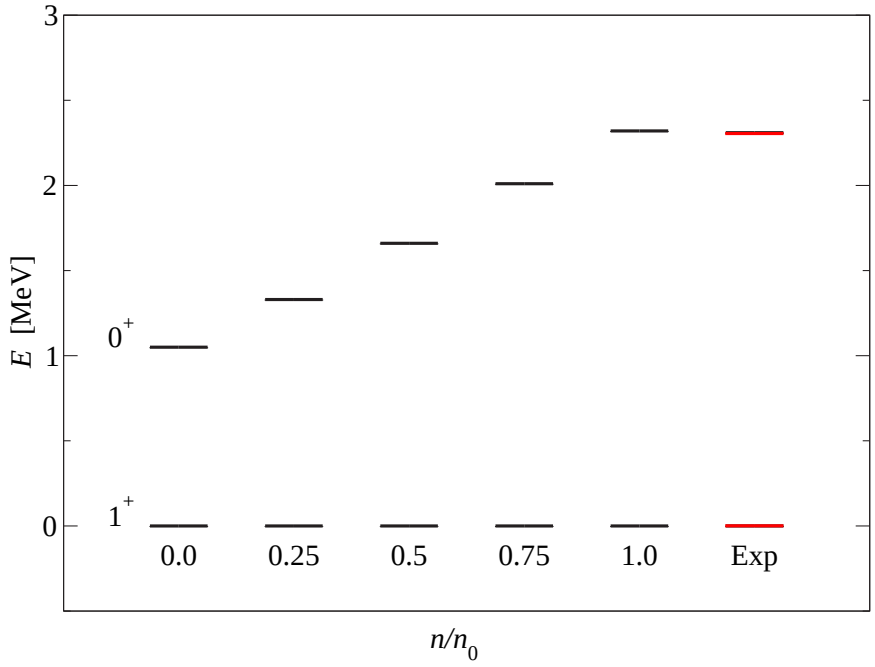

Figure 6.8: The splitting between the 1^+_1 and 0^+_1 levels in ^{14}N for different values of the nuclear density. Also included is the experimental value.

Chapter 7

Summary and Outlook

It is well known that the nuclear interaction in-medium is different than in free space. One of the primary deficiencies in applying free-space NN interaction models to problems in dense nuclear systems is that traditionally, once the interaction is defined in free space, all degrees of freedom responsible for the interaction are "frozen out". Such degrees of freedom include mesons, of course, but also excited states of the nucleon (such as Δ states that account for the intrinsic structure of nucleons). A complete theory of the nuclear force would of course treat these degrees of freedom explicitly in a dense nuclear system. However, this would represent a truly formidable task. Although the traditional means for incorporating such neglected degrees of freedom is to introduce three-nucleon forces, it has been our primary thesis that modifying the masses of the exchanged mesons in one-boson-exchange interactions can provide a promising alternative framework for incorporating density dependence into the nuclear interaction. Moreover, such an approach has the advantage that there is a more direct connection to chiral symmetry breaking and the dynamical generation of hadron mass.

We have demonstrated how medium-modified nuclear interactions inspired by Brown-Rho scaling can give us an understanding of nuclear properties close to nuclear matter density. The inability of two-body interactions alone to reproduce the saturation energy and density of symmetric nuclear matter has long been disappointing. However, we have found that the use of Brown-Rho-scaled NN interactions in an all-order ring diagram summation brings the saturation density well in line with experiment, and the binding energy at saturation is similar to that found with the introduction of three-nucleon forces. Extending this description to asymmetric nuclear matter, we extracted the nuclear symmetry energy and constructed the equation of state of cold, catalyzed neutron star matter. Some of these results were confirmed by studying symmetric nuclear matter within the framework of Landau Fermi liquid

theory. Here we found close agreement with the compression modulus and symmetry energy found in our ring diagram calculation.

Finite nuclei present a more difficult testing ground for medium-modified nuclear interactions. Not only do most properties of normal nuclei depend on the valence nucleons, whose wavefunctions are spread across a region with widely varying density, but those densities are generally too small to give rise to much of a medium effect. We suggest that an exception is the ^{14}C dating beta decay. Not only do the valence nucleons sample a large nuclear density, but this decay is particularly sensitive to the nuclear tensor force, which unambiguously decreases in Brown-Rho scaling. Our results are in very good agreement with the experimental lifetime, and thus in-medium nuclear interactions may be a significant part of the complete solution to this long-standing problem.

We look forward to continuing the study of medium-modified nuclear interactions and their applications to problems in nuclear structure. It is true that realistic NN potential models are finely tuned to free-space data and that variations in the implementation of BRS will have important consequences for the results of calculations. Therefore, we have chosen in these studies to focus on results which we believe are model-independent. That is, even if future theoretical and experimental work give us new information about the scaling of hadron mass in medium, as long as the findings are qualitatively similar to the models we have used, then we expect our main conclusions to be sound. It is our hope that this work stimulates additional interest in this promising new field.

Appendix A

Alternative Perspectives on Brown-Rho Scaling

Since 1991 when Brown-Rho scaling was originally introduced, new insights into the justification and implementation of the theory have been developed. In this appendix we first summarize the Hidden Local Symmetry theory that aims to describe hadronic physics up to the chiral phase transition. Dropping vector meson masses arise naturally within the framework of HLS, which is now considered to be the formal basis for Brown-Rho scaling. Following this discussion we consider different ways to implement BRS in studies of nuclear structure. We distinguish between the chiral Fermi liquid approach used by other authors and the microscopic approach we have developed in previous chapters.

A.1 Hidden local symmetry

In addressing how light-quark vector mesons behave in hot and/or dense matter using effective field theories, there are three essential requirements: (1) the vector mesons have to be explicit degrees of freedom, (2) although the vector mesons are much heavier than the π in free space, one should be able to treat systematically and consistently vector mesons whose masses decrease toward m_π at some temperature T and density n, and (3) the effective theory should be matched to QCD at some large scale in order to make the connection to the fundamental theory. The only effective theory that incorporates all of these three ingredients is the hidden local symmetry theory of Harada and Yamawaki (HLS) [39]. The first point is obvious and taken into account by everyone addressing the problem. Point (2) is made feasible by introducing the vector mesons as local gauge fields. Without exploiting local gauge invari-

ance, it is difficult to handle vanishing vector meson masses. The last point is required so that the gauged chiral Lagrangian flows to QCD as the scale is raised. Otherwise, the gauge theory can wind up giving results that have nothing to do with QCD when the temperature reaches the critical value. All of these points are clearly stated and demonstrated in the Harada-Yamawaki (HY) work. We note that most of the phenomenological chiral Lagrangians used by other workers lack the requirements (2) and (3).

The HLS is an effective field theory based on the gauge equivalence of the $SU(N_f)_L \otimes SU(N_f)_R/SU(N_f)_V$ nonlinear sigma model and the corresponding linear theory with $[SU(N_f)_L \otimes SU(N_f)_R]_{\rm global} \otimes [SU(N_f)_V]_{\rm local}$ symmetry. The gauge fields generated by the local $SU(N_f)_V$ symmetry are identified with the ρ meson and its flavor partners, which acquire a mass through the spontaneous breaking of the hidden local symmetry via the Higgs mechanism. Since the theory is based on the nonlinear chiral Lagrangian, which is known to be nonrenormalizable in more than two dimensions, the HLS theory breaks down and needs to be matched to the fundamental renormalizable theory QCD at the appropriate scale $\Lambda_\chi \sim 4\pi f_\pi \sim 1.1$ GeV. This is accomplished via Wilsonian matching of the two-point correlation functions in HLS to those given by the operator product expansion (OPE) in QCD. The important aspect of the Harada-Yamawaki approach is the inclusion of quadratic divergences (in addition to the usual logarithmic divergences) in the loop corrections to the two-point functions. When the HLS correlation functions are matched to the OPE, the bare parameters at the given scale in the HLS Lagrangian can be determined uniquely.

For definiteness, we consider 2-flavor HLS theory with the $U(2)$ gauge fields $V_\mu = (\rho_\mu, \omega_\mu)$. HY's HLS Lagrangian at the chiral order $\mathcal{O}(p^2)$ in the chiral limit has three parameters, the gauge coupling g and the two decay constants F_π and F_σ that figure in the chiral field U with coordinates in the coset space G/H (to which $G \times H_{local}$ is gauge equivalent)[1]

$$U = e^{\frac{2i\pi}{F_\pi}} = \xi_L^\dagger \xi_R \tag{A.1}$$

$$\xi_{\rm L,R} = e^{i\sigma/F_\sigma} e^{\mp i\pi/F_\pi} \ , \ [\, \pi = \pi^a \tau_a/2 \, , \, \sigma = \sigma^a \tau_a/2] \ , \tag{A.2}$$

where π denote the Nambu-Goldstone (NG) bosons associated with the spontaneous breaking of G chiral symmetry and σ denote the NG bosons associated with the spontaneous breaking of the local H_{local} symmetry. At the next chiral order, there are many terms that we don't need to write down here. They are

[1]The gauge symmetry defined in this way is a hidden symmetry but it can be more properly considered as an "emergent gauge symmetry" as described in [162].

taken into account in [39].

As shown in [39], HY's HLS Lagrangian is amenable to a systematic chiral perturbation theory with the vector meson mass considered *on the same footing* as the pion mass in the chiral counting. One-loop renormalization-group analysis reveals a variety of fixed points, including a fixed line in the parameters (g, F_π, F_σ). Matching to QCD at a given matching point Λ_M in terms of the vector and axial vector current correlators and requiring that the vector correlator equal the axial correlator when the quark condensate vanishes, i.e. $\langle\bar{q}q\rangle \to 0$, picks one particular fixed point called the "vector manifestation (VM)" fixed point[2]

$$(g^*, a^*) = (0, 1) \tag{A.3}$$

where $a = (F_\sigma/F_\pi)^2$. The important finding in this HLS theory is that a hadronic system in heat bath is *driven* to this fixed point when temperature approaches the chiral restoration temperature T_c (and also when density reaches its critical density n_c)[3]. Note that the parametric pion decay constant F_π does not figure in (A.3). This is because it does not possess anything special at any temperature. However at the pion on-shell, it is canceled at T_c by thermal loop corrections so that the physical pion decay constant f_π^* vanishes at the critical point as required by QCD. We now discuss these points in more detail.

The tree level contributions to the two-point functions of the background fields $\bar{\mathcal{A}}_\mu$ (axial vector field), $\bar{\mathcal{V}}_\mu$ (vector field), and $\bar{V}_\mu$ (HLS gauge boson field)

[2]This fixed point was established at one loop order but it is not difficult to convince oneself that this fixed point is unaffected by higher-order graphs. There are several ways to see this. The simplest is the following. Although higher-loop calculations are not available, it has been proven by Harada, Kugo and Yamawaki [163] that the tree-order low-energy theorems remain rigorously valid to all orders. In particular the dimension-2 operators in the effective action remain the same to all orders. This means that the crucial relation in HLS, i.e., $m_\rho^2 = a f_\pi^2 g^2$, holds to all orders. The mass, therefore, goes to zero as g goes to zero. Now the matching condition at the matching scale Λ says that $g = 0$ when $\langle\bar{q}q\rangle = 0$ and since $g = 0$ is a fixed point of the RGE for g at any order (higher loops bring in higher powers in g in the beta function), it will flow to zero at the point where the condensate vanishes. One can also see that $a = 1 + \mathcal{O}(g^{2n})$ near $\langle\bar{q}q\rangle = 0$ where n is the number of loops, so near T_c the correction to 1 is small and at T_c, $a = 1$. Therefore we have the VM fixed point intact.

[3]Here and in what follows, unless stated otherwise, statements made for temperature will apply equally to density.

are given by

$$\begin{aligned}
\Pi^{(\mathrm{tree})\mu\nu}_{\bar{\mathcal{A}}\bar{\mathcal{A}}}(p) &= F^2_{\pi,\mathrm{bare}} g^{\mu\nu} + 2 z_{2,\mathrm{bare}} (g^{\mu\nu} p^2 - p^\mu p^\nu) \\
\Pi^{(\mathrm{tree})\mu\nu}_{\bar{\mathcal{V}}\bar{\mathcal{V}}}(p) &= F^2_{\sigma,\mathrm{bare}} g^{\mu\nu} + 2 z_{1,\mathrm{bare}} (g^{\mu\nu} p^2 - p^\mu p^\nu) \\
\Pi^{(\mathrm{tree})\mu\nu}_{\bar{V}\bar{V}}(p) &= F^2_{\sigma,\mathrm{bare}} g^{\mu\nu} + \frac{1}{g^2_{\mathrm{bare}}} (g^{\mu\nu} p^2 - p^\mu p^\nu).
\end{aligned} \tag{A.4}$$

Loop contributions introduce divergences that are renormalized by the bare parameters in Eq. (A.4). In particular, one can show that the divergent parts of the one-loop corrections are given by

$$\begin{aligned}
\Pi^{\mu\nu}_{\bar{\mathcal{A}}\bar{\mathcal{A}}}(p)|_{\mathrm{div}} &= -g^{\mu\nu} \frac{N_f}{4(4\pi)^2} [2(2-a)\Lambda^2 + 3a^2 g^2 F^2_\pi \ln\Lambda^2] \\
&\quad -(g^{\mu\nu} p^2 - p^\mu p^\nu) \frac{N_f}{(4\pi)^2} \frac{a}{12} \ln\Lambda^2,
\end{aligned} \tag{A.5}$$

$$\begin{aligned}
\Pi^{\mu\nu}_{\bar{\mathcal{V}}\bar{\mathcal{V}}}(p)|_{\mathrm{div}} &= -g^{\mu\nu} \frac{N_f}{4(4\pi)^2} [(1+a^2)\Lambda^2 + 3a g^2 F^2_\pi \ln\Lambda^2] \\
&\quad -(g^{\mu\nu} p^2 - p^\mu p^\nu) \frac{N_f}{(4\pi)^2} \frac{a^2 - 4a + 5}{24} \ln\Lambda^2,
\end{aligned} \tag{A.6}$$

$$\begin{aligned}
\Pi^{\mu\nu}_{\bar{V}\bar{V}}(p)|_{\mathrm{div}} &= -g^{\mu\nu} \frac{N_f}{4(4\pi)^2} [(1+a^2)\Lambda^2 + 3a g^2 F^2_\pi \ln\Lambda^2] \\
&\quad -(g^{\mu\nu} p^2 - p^\mu p^\nu) \frac{N_f}{2(4\pi)^2} \frac{87 - a^2}{12} \ln\Lambda^2
\end{aligned} \tag{A.7}$$

where Λ is the cut-off. In the following discussion we will be interested in the renormalization of the three bare parameters $F_{\pi,\mathrm{bare}}$, $F_{\sigma,\mathrm{bare}}$, and g_{bare}, which is accomplished by requiring the following to be finite

$$F^2_{\pi,\mathrm{bare}} - \frac{N_f}{4(4\pi)^2} [2(2-a)\Lambda^2 + 3a^2 g^2 F^2_\pi \ln\Lambda^2] = (\mathrm{finite}) \tag{A.8}$$

$$F^2_{\sigma,\mathrm{bare}} - \frac{N_f}{4(4\pi)^2} [(1+a^2)\Lambda^2 + 3a g^2 F^2_\pi \ln\Lambda^2] = (\mathrm{finite}) \tag{A.9}$$

$$\frac{1}{g^2_{\mathrm{bare}}} \frac{N_f}{2(4\pi)^2} \frac{87 - a^2}{12} \ln\Lambda^2 = (\mathrm{finite}). \tag{A.10}$$

With μ traded for Λ in the manner described in [39], Eqs. (A.8)-(A.10) yield

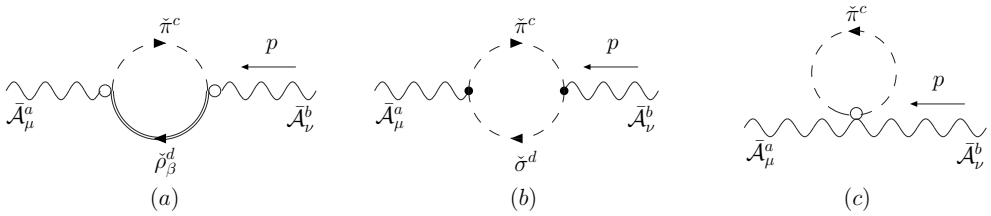

Figure A.1: One loop corrections to the axial vector-axial vector correlation function.

the renormalization group equations for F_π, F_σ, and g defined at the scale μ:

$$\mu\frac{dF_\pi^2}{d\mu} = \frac{N_f}{2(4\pi)^2}[3a^2g^2F_\pi^2 + 2(2-a)\mu^2] \tag{A.11}$$

$$\mu\frac{dF_\sigma^2}{d\mu} = \frac{N_f}{2(4\pi)^2}[3ag^2F_\pi^2 + (a^2+1)\mu^2] \tag{A.12}$$

$$\mu\frac{dg^2}{d\mu} = \frac{-N_f}{2(4\pi)^2}\frac{87-a^2}{6}g^4. \tag{A.13}$$

Defining $a = F_\sigma^2/F_\pi^2$, we obtain the RGE

$$\mu\frac{da}{d\mu} = \frac{-N_f}{2(4\pi)^2}(a-1)[3a(a+1)g^2 + (a^2+1)\mu^2]. \tag{A.14}$$

From eqs. (A.13) and (A.14) we see that the RG fixed points are $g = 0$ and $a = 1$. At these points, the longitudinal components of the ρ join the pions. This is why they are called the vector manifestation (VM) fixed points. Since $M_\rho^2(\Lambda) \equiv g^2(\Lambda)F_\pi^2(\Lambda)a(\Lambda)$, where F_π is the parametric parameter, substantially larger than the on-shell f_π, $M_\rho \to 0$ at the fixed point. Let us now consider the RG equation for F_π at the VM fixed point. There are three one-loop diagrams that contribute divergences to the axial vector two-point function shown in Fig. A.1. The divergent parts of these three diagrams are given by

$$
\begin{aligned}
\text{(a) } \Pi^{\mu\nu}_{\bar{\mathcal{A}}\bar{\mathcal{A}}}(p)|_{\rm div} &= -g^{\mu\nu} N_f \frac{a M_\rho^2}{(4\pi)^2} \ln \Lambda^2 \\
\text{(b) } \Pi^{\mu\nu}_{\bar{\mathcal{A}}\bar{\mathcal{A}}}(p)|_{\rm div} &= -g^{\mu\nu} N_f \frac{a}{4(4\pi)^2} [2\Lambda^2 - M_\rho^2 \ln \Lambda^2] \\
&\quad -(g^{\mu\nu} p^2 - p^\mu p^\nu) N_f \frac{a}{12(4\pi)^2} \ln \Lambda^2 \\
\text{(c) } \Pi^{\mu\nu}_{\bar{\mathcal{A}}\bar{\mathcal{A}}}(p)|_{\rm div} &= g^{\mu\nu} N_f \frac{a-1}{(4\pi)^2} \Lambda^2
\end{aligned}
\tag{A.15}
$$

The nonlinear sigma model has only the π loop in Fig. A.1(c). Then from (A.15) we see that

$$
\Pi^{(1-\text{loop})\,\mu\nu}_{\bar{\mathcal{A}}\bar{\mathcal{A}}}(p)|_{\rm div} = -g^{\mu\nu} \frac{N_f \Lambda^2}{(4\pi)^2} \tag{A.16}
$$

Renormalization is done by

$$
\left[F_\pi^{(\pi)}(\Lambda)\right]^2 - N_f \frac{\Lambda^2}{(4\pi)^2} = \text{ (finite)} \tag{A.17}
$$

which gives

$$
\mu \frac{d}{d\mu} \left[F_\pi^{(\pi)}\right]^2 = \frac{2N_f}{(4\pi)^2} \mu^2. \tag{A.18}
$$

Integrating from $\mu = 0$ one finds

$$
\left[F_\pi^{(\pi)}(\Lambda)\right]^2 - \left[F_\pi^{(\pi)}(0)\right]^2 = N_f \frac{\Lambda^2}{(4\pi)^2} \tag{A.19}
$$

so the maximum scale that can be reached is

$$
\Lambda = \frac{4\pi F_\pi^{(\pi)}(\Lambda)}{\sqrt{N_f}}. \tag{A.20}
$$

For $N_f = 2$, $\Lambda_{\rm max} = \frac{4\pi F_\pi(\Lambda)}{\sqrt{2}} \sim 700$ MeV after taking $F_\pi^{(\pi)} \sim 90$ MeV, which is needed to satisfy the KFSR relation

$$
M_\rho^2 = 2 g_V^2 F_\pi^2. \tag{A.21}
$$

But this $\Lambda_{\rm max}$ is only the magnitude of the cutoff typically used in Nambu-Jona-Lasinio models [164] and not large enough to accommodate the on-shell mass of the ρ-meson.

Now at M_ρ^2 going up in scale, $\Lambda^2 > M_\rho^2$, $F_\pi^2(0)$ begins to scale more slowly.

(Remember that F_π is the parametric pion decay constant, with a very different behavior with Λ than the physical decay constant f_π.) In order to understand this we go to the relevant parts of the loop corrections in Figs. A.1(b) and (c). (We need not consider Fig. A.1(a) or the logarithmically divergent part of (b) because they are both proportional to M_ρ^2 which goes to zero at the fixed point.)

$$\begin{aligned} \text{(b) } \Pi^{\mu\nu}_{\bar{A}\bar{A}}(p)|_{\rm div} &= -g^{\mu\nu} N_f \frac{a}{4(4\pi)^2} 2\Lambda^2 \\ \text{(c) } \Pi^{\mu\nu}_{\bar{A}\bar{A}}(p)|_{\rm div} &= g^{\mu\nu} N_f \frac{a-1}{(4\pi)^2}\Lambda^2 \end{aligned} \tag{A.22}$$

If we are in HLS, $a = 2$ at $\Lambda = m_\rho$ because KFSR $m_\rho^2 = a f_\pi^2 g_V^2$ and $f_\pi \simeq 90$ MeV. The relevant part of $\Pi^{(b)\mu\nu}_{\bar{A}\bar{A}}(p)|_{\rm div}$, $aN_f\Lambda^2/2(4\pi)^2$, takes over with increasing scale from the $(a-1)N_f\Lambda^2/2(4\pi)^2$ of $\Pi^{(c)\mu\nu}_{\bar{A}\bar{A}}(p)|_{\rm div}$ as a goes to its fixed point $a = 1$ with increasing Λ. This has the effect of increasing the maximum Λ of Eq. (A.20) to

$$\Lambda_{\rm max} = 4\pi\sqrt{\frac{2}{N_f}} F_\pi(\Lambda). \tag{A.23}$$

Thus, for $N_f = 2$ which we are interested in, we are back to $\Lambda_{\rm max} = 4\pi F_\pi(\Lambda)$. Now the usual chiral symmetry breaking scale is $4\pi f_\pi \simeq 1$ GeV, where f_π is the physical pion decay constant. From Table 13 in [39] we note that $F_\pi(\Lambda)$ for $\Lambda = 1-1.2$ GeV is about 50% larger than the physical $f_\pi \sim 90$ MeV. Thus, the Wilsonian matching is easily carried out at T_c where Λ will be $4\pi f_\pi$.

We thus see that the Nambu-Jona-Lasinio theory, which deals with constituent quarks, and where Λ can be brought up to $4\pi F_\pi^{(\pi)}(\Lambda)/\sqrt{N_f}$, can be extended by introducing the ρ-meson in the vector manifestation of Harada and Yamawaki to a matching scale of $4\pi F_\pi(\Lambda)$ for two flavors. In fact, the scaling of the chiral symmetry breaking near the maximum value is run by the Higgs-type Fig. A.1(b), where the scalar particle, the would-be Goldstone boson, is in fact "eaten" by the ρ-meson to give it its mass. The Harada-Yamawaki theory is, therefore, consistent, in that one needs to introduce the ρ-meson into it in order to accommodate the ρ-meson.

The HLS Lagrangian matched to QCD defines a bare Lagrangian defined at the scale $\mu = \Lambda_M$ with the bare parameters *intrinsically dependent* on the background, e.g. temperature, tagged to the QCD condensates $\langle\bar{q}q\rangle$, $\langle G^2_{\mu\nu}\rangle$ etc. which "slide" with temperature. We call this "IBD" for intrinsic background dependence. Given the bare Lagrangian with IBD, the theory is well

defined, so in principle, quantum calculations for physical quantities can be done systematically by RGE and thermal (or dense) loop corrections. Now because of the fixed point (A.3), the parametric vector mass which runs with the scale μ and the background as

$$M_v^2(\mu,T) = g^2(\mu,T)F_\sigma^2(\mu,T) = a(\mu,T)g^2(\mu,T)F_\pi^2(\mu,T) \tag{A.24}$$

goes to zero when $\langle\bar{q}q\rangle$ (or $T-T_c$) goes zero, i.e.,

$$M_v^2(\mu,T) \sim g^2(\mu,T) \propto \langle\bar{q}q\rangle^2 \to 0. \tag{A.25}$$

This means that in-medium "on-shell", not only the parametric mass M_v but also the physical (pole) mass m_v goes to zero as $T \to T_c$,

$$m_v^2 \propto g^2(m_v,T) \propto \langle\bar{q}q\rangle^2 \to 0. \tag{A.26}$$

This relation provides a justification for Brown-Rho scaling as we explain below.

A.2 Brown-Rho scaling updated

Presently available lattice and experimental data allow us to write a refined and more precise Brown-Rho scaling that should supersede the old version of 1991. The updated relation comes about since whereas HLS/VM makes an extremely simple description of hot/dense matter very near the VM fixed point, the situation is a lot more complex away from the fixed point as pointed out in [165, 166]. Near the VM fixed point, everything is controlled by the gauge coupling which is proportional to the quark condensate. Thus the mass of the vector meson goes like

$$\frac{m_v^*}{m_v} \approx \frac{M_v^*}{M_v} \approx \frac{g^*}{g} \approx \frac{\langle\bar{q}q\rangle^*}{\langle\bar{q}q\rangle} \tag{A.27}$$

where M_v and m_v are, respectively, the parametric and pole masses. In order to see where this scaling sets in, we resort to lattice information which is available in temperature. The useful information comes from the unquenched lattice data of Miller [167] on the gluon condensate in heat bath, which we show in Fig. A.2. As explained in [168] (where previous references are given), we can approximately separate the gluon condensate into two components

$$\langle G^2\rangle_T = \langle G^2\rangle_T^{soft} + \langle G^2\rangle_T^{hard} \tag{A.28}$$

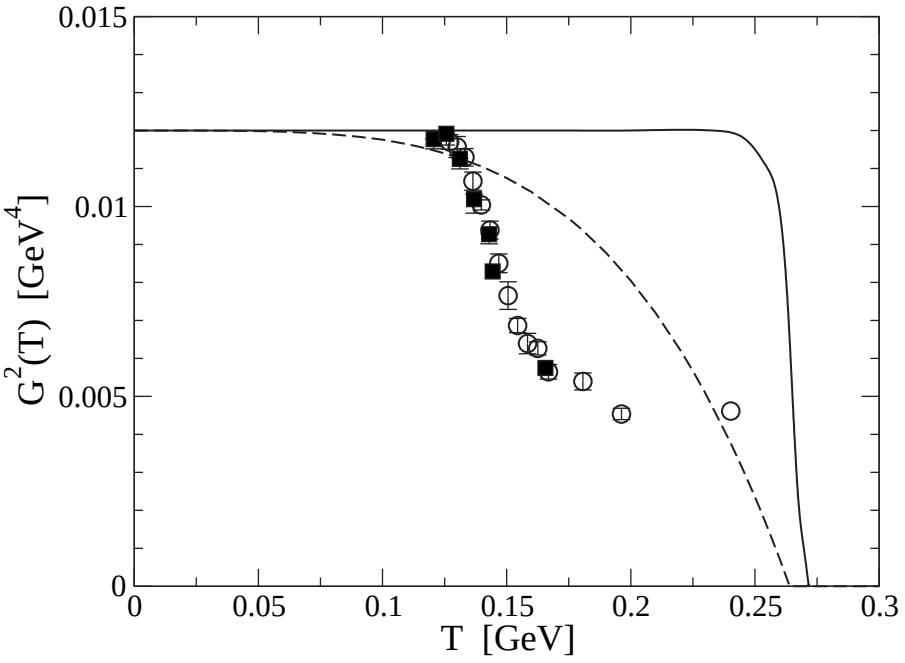

Figure A.2: The lines show the gluon condensates for SU(3) (solid) and the ideal gluon gas (broken) in comparison with that of the light dynamical quarks denoted by the open circles and the heavier ones with filled squares. The error bars are included when significant.

where the subscript "soft" and "hard" denote the scale of the condensate. It has been suggested [168] that the "hard" component that remains condensed as one goes up across the critical temperature T_c be associated with an *explicit* breaking of scale invariance caused by the trace anomaly of QCD and the "soft" component that starts melting at $T \sim 120$ MeV be linked to a *spontaneous* breaking of scale invariance. It has been postulated that the soft component is associated with what generates hadron masses and hence the spontaneous breaking of chiral symmetry. Now from this lattice result, we obtain the following simplified picture: The gauge coupling g remains constant from $T = 0$ to $T \sim 120$ MeV and then drops steeply, going to zero at $T_c \sim 200$ MeV. For the reason that will be clarified below, we call the temperature at which the soft glue starts melting "flash temperature" T_{flash}.

The situation with density is much less clear since there is neither lattice nor experiment to guide us. However we can make a parallel argument based on our understanding of nuclear physics. As in temperature, we assume that the soft glue is associated with the behavior of the dynamical mass as a function of density. Up to nuclear matter density n_0, the gauge coupling is known to stay more or less constant. It is possible that it stays constant to a larger density, so we assume the density above which the g starts dropping (proportionally to the quark condensate), to be the "flash density" $n_{flash} > n_0$. Where precisely this happens is not known, but a reasonable guess is that

$$n_{flash} \sim 2n_0. \tag{A.29}$$

Now in both temperature and density, the parameter a remains constant ($= 2$ in nature) up to the flash point and from then drops to 1 as the VM point is reached. As noted, it is suggestive from the consideration of skyrmion-half-skyrmion transition [169] that a drops to 1 much faster in dense matter than in hot matter. This observation was used in arriving at the strong suppression of dilepton production in dense/hot matter. As for the mass scaling, the prediction is

$$\frac{M_v^*}{M_v} \approx \frac{f_\pi^*}{f_\pi}, \ \aleph < \aleph_{flash}, \tag{A.30}$$

$$\frac{M_v^*}{M_v} \approx \frac{m_v^*}{m_v} \approx \frac{g^*}{g} \approx \frac{\langle \bar{q}q \rangle^*}{\langle \bar{q}q \rangle}, \ \aleph \geq \aleph_{flash} \tag{A.31}$$

where $\aleph = T$ or n. Below the flash point, particularly in the case of density, due to thermal/dense loop corrections, the pole mass scales in a complicated way as explained in [165, 166], so it cannot be simply related to the parameters of the Lagrangian. This is why (A.30) does not involve pole mass. Beyond

the flash point, the scaling becomes simpler and more predictive vis-à-vis with chiral symmetry property, as indicated in (A.31). Equations (A.30) and (A.31) are the modernized version of Brown-Rho scaling backed by HLS/VM theory. The strong-coupling lattice calculation at the leading order in $1/g^2$ gives for $n_c \geq n > 0$ in dense matter [170]

$$\frac{M_v^*}{M_v} \approx \frac{m_v^*}{m_v} \approx \frac{f_\pi^*}{f_\pi}. \tag{A.32}$$

It remains to be seen whether $1/g^2$ and $1/d$ (where d is the number of dimensions (= 2)) corrections lead this result to the form (A.31).

It should be stressed that while the scaling (A.31) gets a support from HLS/VM theory, (A.30) is yet to be established. Furthermore the numerical values for $\aleph_{flash}$ – in particular that in density – quoted above are no more than a guess and yet to be determined in the theory.

By *parametric scaling* we refer to the scaling of the parameters F_π, etc. which enter into the chiral Lagrangian. One must then take this Lagrangian and calculate thermal or dense loops, which will somewhat change the medium dependence. A point which is generally unappreciated in the heavy-ion theory community is that in a heat bath even at low temperatures the (second) loop corrections are mandatory for consistency with the symmetry of QCD. In fact, in the combination of parametric and loop terms, the pole mass of the vector meson increases proportional to T^4 near zero temperature with no T^2 term present as required by the low-energy theorem [171]. As the temperature of chiral restoration $T_{\chi SR}$ is approached, both the bare mass term and the loop corrections go to zero as $\langle \bar{q}q \rangle \to 0$. In this case the pole mass does directly reflect on chiral structure as does Brown-Rho scaling. *Only in the vicinity of T_c does BR scaling manifest itself transparently in the pole mass of the vector meson in a heat bath.*

Evaluation of $g_\pi^\star/f_\pi$ with Eqs. (1.25) & (1.26) gives a 20% drop in this quantity by nuclear matter density n_0. This agrees with the value extracted at tree order from pionic atoms [172]. The same decrease is implied by Brown-Rho scaling for $m_\rho^\star$. However, the dense loop enters also here and, although small, will increase the mass a few MeV. Thus, the decrease of $\sim 15\%$ in $m_\rho^\star$ by nuclear matter density seems reasonable.

Harada and Yamawaki find that $m_\rho^\star$ scales linearly with $\langle \bar{q}q \rangle$ as $m_\rho^\star \to 0$ at the fixed point of chiral symmetry restoration. In fact, although the comparison with lattice results on the entropy is relatively crude in Koch and Brown [46], it is seen that with temperature the scaling of the masses may begin less rapidly than the scaling with $\langle \bar{q}q \rangle^\star$, but that it quickly becomes as rapid. Brown and Rho [173] found that up to nuclear matter density n_0, g did

not scale, but slightly above n_0 the ratio $g^\star/m_\rho^\star$ was roughly constant. The ratio is constant going toward the fixed point of Harada and Yamawaki. Thus we believe that the decrease of $m_\rho^\star$ as $\sqrt{\langle\bar{q}q\rangle^\star}$ goes only up to $n \sim n_0$ and that it then scales linearly with $\langle\bar{q}q\rangle^\star$. If it decreases $\sim 20\%$ in going from $n = 0$ to n_0, it will then increase $\sim 2\sqrt{2}$ in going from n_0 to $2n_0$, and $m_\rho^\star$ will go to zero at $n \sim 4n_0$, the scalar density at chiral restoration. From this estimate we believe

$$n_{\chi SR} \sim 4n_0. \tag{A.33}$$

Given the Walecka mean field theory [174] and the study of the density and temperature dependence of a system of constituent quarks in the Nambu-Jona-Lasinio theory [175], Brown-Rho scaling appeared quite natural, at least the scaling with density, even a long time before its acceptance (it is not universally accepted even now, although it has come to life rather quickly after each of its many reported deaths).

The Walecka theory showed that the nucleon effective mass decreased with density. Perhaps most convincing of the arguments in its favor was that the spin-orbit term, which depends on $(m_N^\star)^{-2}$ was increased enough to fit experiment. The usual nonrelativistic theories were typically a factor of 2 too low in spin-orbit interaction at that time. What could be more natural than as a nucleon dissolves into its constituents, the masses $m_Q^\star$ of the constituent quarks decreases at the same rate as the nucleon mass $m_N^\star$ in Walecka theory? In fact, this is what happens in the Harada-Yamawaki theory, although it does not contain nucleons (the effect of fermions was studied in [176] by introducing constituent quarks). Once the density is high enough so that constituent quarks become the relevant variables, we should go over to a quark description, as described above and as Bernard *et al.* [175] did. Then the constituent quark mass will change with increasing density, going to zero the way the constituent quark went over to a current quark as the temperature increased from $T = 125$ MeV to 175 MeV (T_c(unquenched)). Since at zero density nucleons are the relevant variables, it will take some time in adding nucleons in positive energy states before these cancel enough of the condensate of nucleons in negative energy states so that they can go over into loosely bound constituent quarks. In fact, with a cutoff of $\Lambda = 700$ MeV, close to what we use, Bernard et al. [175] found that in the chiral limit the quark mass went to zero at $2n_0$.

A.2.1 Landau Fermi-liquid fixed point and Brown-Rho scaling

The meaning of Brown-Rho scaling has often been misinterpreted in the literature for processes probing densities in the vicinity of nuclear matter density,

most recently in connection with the NA60 dilepton data. We wish to clarify the situation by emphasizing the intricacy involved in what the scaling relation represents in the strong interactions that take place in many-nucleon systems. This aspect has been discussed in several previous publications by two of the authors (GEB and MR), but it is perhaps not superfluous to do so once more in view of certain recent developments. What we would like to discuss here is the connection between the Brown-Rho scaling factor $\Phi(n)$ (to be defined below) and the Landau parameter F_1 which figures in quasiparticle interactions in Fermi liquid theory of nuclear matter. This discussion illustrates clearly that Brown-Rho scaling cannot *simply* be taken to be *only* the mass scaling as a function of density and/or temperature as is often done in the field. What this illustrates is that the Φ, related in an intricate way to a quasiparticle interaction parameter in Landau Fermi-liquid theory of nuclear matter, incorporates not just the "intrinsic density dependence" (IDD in short) associated with Wilsonian matching to QCD, a crucial element of HLS/VM, but also some of what is conventionally considered as many-body interactions near the Fermi surface associated with the Fermi liquid fixed point. It clearly shows that it is dangerous to naively or blindly apply Brown-Rho scaling to such heavy-ion processes as low-mass dileptons where the density probed is not much higher than nuclear matter density, as was done by several workers in QM2005.

Chiral Fermi liquid field theory (CFLFT)

It was argued by Brown and Rho in [56] (where previous references are given) that addressing nuclear matter from the point of view of effective field theory involves "double decimation" in the renormalization-group sense. The first involves going from a chiral scale or the matching scale Λ_M with "bare Larangian" to the Fermi surface scale $\Lambda_{\rm FS}$ (which will be identified later with Λ_{low-k}). How this could be achieved was discussed in a general context by Lynn some years ago [177] who made the conjecture that the Fermi surface could arise from effective field theories as chiral liquid soliton. For the moment, we will simply assume that such a chiral liquid can be obtained. To proceed from there, we exploit three observations (or, perhaps more appropriately, conjectures). First we learn from the work of Shankar [178] that given an effective Lagrangian built around the Fermi surface, decimating fluctuations toward the Fermi surface leads to the "Fermi liquid fixed point" with the quasiparticle mass $m^\star$ and quasiparticle interactions F being the fixed point parameters. We next learn from Matsui's argument [179] that Walecka mean field theory is *equivalent* to Landau Fermi liquid theory. The third observation is that Walecka mean-field theory can be obtained in the mean field of an effective chiral Lagrangian in which (vector and scalar) massive degrees

of freedom are present, or equivalently, an effective chiral Lagrangian with higher-dimension operators (such as four-Fermi operators) [180–182]. Friman and Rho [117] combined the above three to write an effective chiral Lagrangian endowed with Brown-Rho scaling that in mean field gives *Landau Fermi-liquid theory at the fixed point that is consistent with chiral symmetry.* We call this "chiral Fermi liquid field theory (CFLFT)" to distinguish it from the microscopic theory we have been employing in previous chapters.

As reviewed in [56], there are two classes of effective Lagrangians that should in principle yield the same results in the mean field. One is closely related to a generalized HLS (GHLS) theory where a scalar and nucleons are added to vector mesons. Restricted to symmetric nuclear matter, it has the simple form

$$\begin{aligned}\mathcal{L}_{II} &= \bar{N}(i\gamma_\mu(\partial^\mu + ig_v^\star\omega^\mu) - M^\star + h^\star\sigma)N \\ &\quad -\frac{1}{4}F_{\mu\nu}^2 + \frac{1}{2}(\partial_\mu\sigma)^2 + \frac{m_\omega^{\star\,2}}{2}\omega^2 - \frac{m_\sigma^{\star\,2}}{2}\sigma^2 + \cdots \end{aligned} \tag{A.34}$$

where the ellipsis denotes higher-dimension operators and the star refers to "parametric density dependence" that emerges from a Wilsonian matching to QCD of the type described by Harada and Yamawaki [39]. We have left out (pseudo)Goldstone fields and isovector and strange vector meson fields which do not contribute at mean field level. Note that contrary to its appearance, (A.34) is actually consistent with chiral symmetry since here both the ω and σ fields are *chiral singlets*. In fact, the σ here has nothing to do with the chiral fourth-component scalar field of the linear sigma model except perhaps near the chiral phase transition density where "mended symmetry" may intervene; it is a "dilaton" connected with the trace anomaly of QCD.

An alternative Lagrangian which is in a standard chiral symmetric form involves only the pion and nucleon fields which may be considered as arising when the heavy mesons – both scalar and vector mesons – are integrated out:

$$\mathcal{L}_I = \bar{N}[i\gamma_\mu(\partial^\mu + iv^\mu + g_A^\star\gamma_5 a^\mu) - M^\star]N - \sum_i C_i^\star(\bar{N}\Gamma_i N)^2 + \cdots \tag{A.35}$$

where the ellipsis stands for higher dimension and/or higher derivative operators and the Γ_i's are Dirac and flavor matrices as well as derivatives consistent with chiral symmetry. Here we reinstated the pionic vector and axial vector fields v_μ and a_μ respectively, since the pion contributes (through exchange) to the Landau parameters. We will go back and forth between the two Lagrangians in our discussion.

Leaving out the details which can be found in [56, 119], we summarize the essential features in what is obtained for nuclear matter. In calculating nuclear matter properties with our effective action, the first thing to do is to determine how the nucleon and meson masses scale near nuclear matter saturation density. This cannot be gotten by theory, so we need empirical information. This can be done by looking at the response of nuclear matter to external fields, i.e., the photon. This was first done in [117, 183] using (A.35) in which the isovector anomalous nuclear orbital gyromagnetic ratio δg_l was expressed in terms of Brown-Rho scaling plus contributions from the pion to the Landau parameter ${F_1}^4$

$$\delta g_l = \frac{4}{9}[\Phi^{-1} - 1 - \frac{1}{2}\tilde{F}_1^\pi], \tag{A.36}$$

where $\tilde{F}_1^\pi$ is the pionic contribution to the Landau parameter F_1 – which is precisely calculable for any density thanks to chiral symmetry – and

$$\Phi(n) = \frac{m_M^\star(n)}{m_M}, \tag{A.37}$$

which is referred to as the "Brown-Rho scaling factor." Here the subscript M stands for the mesons $M = \sigma, \rho, \omega$. The isovector gyromagnetic ratio δg_l is measured experimentally. The most precise value comes from giant dipole resonances in heavy nuclei [114]: $\delta g_l = 0.23 \pm 0.03$. With $\frac{1}{3}\tilde{F}_1^\pi = -0.153$ at nuclear matter density n_0, we get from (A.36),

$$\Phi(n_0) = 0.78, \tag{A.38}$$

which is consistent with the value obtained in deeply bound pionic atoms [184]

$$\frac{f_\pi^\star(n_0)}{f_\pi} \simeq 0.80. \tag{A.39}$$

We should stress that this is a value appropriate for normal nuclear matter density which should be reliable near the Fermi liquid fixed point. For describing nuclear matter properties, we need to know how it varies near nuclear matter equilibrium density. A convenient parametrization is

$$\Phi(n) = \frac{1}{1 + yn/n_0} \tag{A.40}$$

[4]This relation is valid up to near nuclear matter density, that is, near the Fermi-liquid fixed point and may not be extended to much higher densities.

with $y = 0.28$.

The Landau effective mass of the quasiparticle at the fixed point is given by

$$m_N^\star(n)/m_N = \left(\Phi^{-1} - \frac{1}{3}\bar{F}_1^\pi\right)^{-1}, \tag{A.41}$$

which at the equilibrium density predicts

$$m_N^\star(n_0)/m_N = 0.67. \tag{A.42}$$

Note that the nucleon mass scales slightly faster than meson masses. This was noted in [45] in terms of the scaling of g_A in medium.

We now look at other properties of nuclear matter with (A.34). Our construction of chiral Fermi liquid theory instructs us to treat the Lagrangian in mean field with the mass and coupling parameters subject to the Brown-Rho scaling. With the standard free-space values for the ω and ρ mesons and the scalar meson mass $m_\sigma \approx 700$ MeV[5], the properties of nuclear matter come out to be [118, 119]

$$B = 16.1 \text{ MeV}, \quad k_F = 258 \text{ MeV}, \ K = 259 \text{ MeV}, m_N^\star/m_N = 0.67 \tag{A.43}$$

where B is the binding energy, k_F the equilibrium Fermi momentum and K the compression modulus. The values (A.43) should be compared with the standard "empirical values"[185]

$$\begin{aligned} B &= 16.0 \pm 0.1 \text{ MeV}, \quad k_F = 256 \pm 2 \text{ MeV}, \\ K &= 250 \pm 50 \text{ MeV}, \ m_N^\star/m_N = 0.61 \pm 0.03. \end{aligned} \tag{A.44}$$

The predicted results (A.43) are in a good agreement with empirical values. Given the extreme simplicity of the theory, it is rather surprising.

We should remark that what makes the theory particularly sensible is that it is thermodynamically consistent in the sense that both energy and momentum are conserved [119, 186]. This is a nontrivial feat. In fact, it has been a major difficulty for nuclear matter models based on Lagragians with density-dependent parameters to preserve the energy-momentum conservation. In the present theory, this is achieved by incorporating a chiral invariant form for the density operator.

[5]Not to be confused with the Goldstone boson σ in HLS theory. Here it is a chiral singlet effective field of scalar quantum number that figures in Walecka-type mean-field theory.

Brown-Rho scaling and microscopic calculation of the Landau parameters

In the CFLFT description given above, we relied on three observations – the validity of which are yet to be confirmed – on the connection between an effective chiral action (or an effective chiral Lagrangian in mean field) and Landau's Fermi liquid fixed point theory, in particular with one of the fixed point parameters mapped to Brown-Rho scaling at the corresponding density. In previous chapters we have used a microscopic approach that combines the two decimations subsumed in the CFLFT approach [118]. Our approach starts with phenomenological potentials fit to scattering data up to a momentum $\Lambda_{NN} \sim 2.1$ fm^{-1}. To understand this result, we can recast the argument in terms of the HLS theory. There is no such potential built from HLS Lagrangian in the literature. However we expect, based on the work of Bogner et al. [58], the resulting driving potential V_{low-k} to be qualitatively the same for the HLS and phenomenological models for low-energy processes. This, we suggest, is essentially the manifestation of the power of what is called "more effective effective theory" explained in [56].

Let us imagine that we have a generalized hidden local symmetry (GHLS) theory that contains a complete set of relevant degrees of freedom for nuclear matter, say, π, ρ, ω, a_1, σ, etc., matched to QCD at a matching scale Λ_M. There are no explicit baryon degrees of freedom in this theory. However baryons must emerge as skyrmions. Since no description of nuclear dynamics starting from a GHLS exists – and we see no reason why it cannot be done – one can alternatively introduce baryon fields as matter fields and couple them in a hidden local symmetric way. This is what one does in standard chiral perturbation theory with global chiral symmetry with pions and nucleons as the only explicit degrees of freedom. The "bare" Lagrangian obtained by Wilsonian matching will carry such parameters as masses and coupling constants endowed with an "intrinsic" background (temperature or density) dependence. These are the quantities that track the properties of the quark and gluon condensates in medium, and hence Brown-Rho scaling.

Given the "bare" Lagrangian so determined, one can then proceed in three steps:

1. First one constructs NN potentials in chiral perturbation theory with the vector mesons treated à la Harada and Yamawaki [39] – here hidden local symmetry plays a crucial role even at zero density as emphasized in [39]. The chiral perturbation procedure is as well formulated in HLS theory as in the standard approach without the vector degrees of freedom.

2. Next one performs a (Wilsonian) renormalization-group decimation to

the "low-k scale"[6] $\Lambda_{low-k} \approx 2$ fm$^{-1} \sim \Lambda_{NN}$ to obtain the V_{low-k}. As stated, we expect the result for V_{low-k} to be basically the same as that obtained in [58, 74, 99] for the T-matrix for NN scattering for which matter density is low. However it will differ in medium due to the intrinsic background dependence which is missing in [74, 99]. This step will correctly implement the *first decimation* of [56] not only in free-space but also in dense medium. The intrinsic dependence incorporated at this stage is missing in *all* works found in the literature.

3. Finally one feeds the V_{low-k} so determined into the Bäckman, Brown and Niskanen nonlinear equation (their equation (5.3)) [105], which resulted from the truncation of the Babu-Brown [66] equation in the sum over Fermi Liquid parameters to $l = 0$ and 1, and solves it by iteration. (For a Green's function formalism for Landau Fermi liquid theory, see [108].) The Babu-Brown equation introduces the induced interaction into dynamical calculations involving Fermi liquid theory and has its own renormalization group treatment [74, 99] which has very successfully been carried out for neutron matter.

These procedures will lead to the Landau parameters given as the sum of a "driving term" and an "induced term." Given the Landau quasiparticle interactions so determined, the standard Fermi liquid arguments are then applied to computing the energy density, Landau effective mass, compression modulus, etc. that describe nuclear matter. Now had the above three-step procedure been followed with HLS, the theory would have Brown-Rho scaling automatically incorporated. However since we take, for step 1, phenomenological potentials in which the intrinsic density dependence (IDD) required by matching to QCD is missing, they need to implement the IDD by hand. They find that without IDD, the known properties of nuclear matter compression modulus, etc. cannot be reproduced correctly. To incorporate Brown-Rho scaling into the potential we employ, e.g., the Bonn one-boson-exchange potential, we introduce σ-tadpole self-energy corrections to the masses of the nucleons and exchanged bosons. Although this procedure may lack the consistency achieved through Wilsonian matching, it should however be equivalent to Brown-Rho scaling in its simplest form. With the Brown-Rho scaling suitably implemented, our results come out to be quite satisfactory.

There are several observations one can make from this result. 1) One can think of this as a confirmation of the soundness of the double decimation procedure. 2) Both our microscopic approach and the effective theory approach [118] – which complement each other – indicate the importance of

[6] In this scheme, this "low-k scale" corresponds to Λ_{FS} introduced above.

Brown-Rho scaling in the structure of nuclear matter. 3) There must be a relation – most likely quite complicated – between Φ and the microscopic potential V_{low-k} valid at nuclear matter density. We believe this relation to result from the scale invariance in nuclear phenomena which results when pion exchange is unimportant in nuclear phenomena, as reviewed in Brown and Rho [56]. There are very few places in *nuclear spectra* where the pion plays the main role[7]. For instance, it does not play much of a role in the polarization phenomena reviewed by Brown and Rho [56], so they come out to be in some sense "scale invariant" for low densities. The pion is, of course, protected from mass change by chiral invariance, and, therefore, does not participate in this "scale invariance." However, in the second-order tensor interaction which is of primary importance for the saturation of nuclear matter, the π and ρ play counterpoint; they enter incoherently, their coupling having opposite sign. The dropping of the ρ-mass in Brown-Rho scaling therefore cuts down the tensor interaction greatly, running up the compression modulus substantially. In the usual calculations which do not employ the intrinsic (*in-medium*) dependence of the masses on density, this effect is included empirically as a three-body interaction. This seems to be the only place in nuclear spectra where Brown-Rho scaling seems to be really needed *explicitly* in the nuclear many-body problem. Nuclear physicists have, however, lived with a substantial spread in effective masses – which cannot be measured directly in nuclear physics – for years, so what we consider as an improvement in $m_N^\star$ is not universally accepted. This reflects again on an intricate interplay between Brown-Rho scaling and many-body interactions.

As a final remark in this subsection, let us return to the implications of the manifestation of chiral symmetry in dense (or hot) medium. It is clear that the connection between Brown-Rho scaling and many-body interactions is highly intricate, particularly near nuclear matter density, and needs to be carefully assessed case by case. As we learned from HLS with the vector manifestation fixed point, Brown-Rho scaling can serve as a clean-cut litmus for chiral restoration – a matter of intense current interest in heavy ion physics – only near the critical point. Only very close to the critical point is the scaling factor Φ directly locked to the chiral order parameter $\langle\bar{q}q\rangle^\star$. Far away from that point, particularly near normal nuclear matter density, the connection, strongly infested with many-body interactions, can be tenuous at best. To the extent that the dileptons in NA60 as well as in CERES, for instance, do not selectively sample the state of matter near the chiral transition point, infor-

[7]One should, however, note that this is not the case in nuclear response functions, namely in nuclear matrix elements of electroweak currents. It is known that in certain transition matrix elements, such as in M1 transitions and axial charge transitions, soft-pions play an extremely important role. This is referred to as "chiral filter mechanism [187]."

mation on the order parameter cannot be extracted cleanly from the measured spectral function.

Bibliography

[1] M. Creutz. *Quarks, Gluons, and Lattices*. Cambridge University Press, Cambridge, (1985).

[2] H. Rothe. *Lattice Gauge Theories: An Introduction*. World Scientific, Singapore, (2005).

[3] N. Ishii, S. Aoki, and T. Hatsuda. *Phys. Rev. Lett.*, **99**:022001, (2007).

[4] H. Yukawa. *Proc. Phys. Math. Jpn.*, **17**:48, (1935).

[5] H. Yukawa. *Proc. Phys. Math. Jpn.*, **19**:712, (1937).

[6] R. B. Wiringa, V. G. J. Stoks, and R. Schiavilla. *Phys. Rev. C*, **51**:38, (1995).

[7] V. G. J. Stoks, R. A. M. Kompl, M. C. M. Rentmeester, and J. J. de Swart. *Phys. Rev. C*, **48**:792, (1993).

[8] V. G. J. Stoks, R. A. M. Klomp, C. P. F. Terheggen, and J. J. de Swart. *Phys. Rev. C*, **49**:2950, (1994).

[9] R. Machleidt. *Phys. Rev. C*, **63**:024001, (2001).

[10] D. R. Entem, R. Machleidt, and H. Witala. *Phys. Rev. C*, **65**:064005, (2002).

[11] K. A. Brueckner and C. A. Levinson. *Phys. Rev.*, 97:1344, (1955).

[12] K. A. Brueckner and J. L. Gammel. *Phys. Rev.*, 109:1023, (1958).

[13] B. D. Day. *Rev. Mod. Phys.*, 39:719, (1967).

[14] S. K. Bogner, T. T. S. Kuo, and A. Schwenk. *Phys. Rept.*, 386:1, (2003).

[15] S. K. Bogner, T. T. S. Kuo, L. Coraggio, A. Covello, and N. Itaco. *Phys. Rev. C*, **65**:051301(R), (2002).

[16] T. T. S. Kuo, S. Y. Lee, and K. F. Ratcliff. *Nucl. Phys.*, **A176**:65, (1971).

[17] T. T. S. Kuo and E. Osnes. *Lecture Notes in Physics Vol. 364*. Springer-Verlag, New York, (1990).

[18] F. Andreozzi. *Phys. Rev. C*, **54**:684, (1996).

[19] E. M. Krenciglowa and T. T. S. Kuo. *Nucl. Phys.*, **A235**:171, (1974).

[20] S. A. Moszkowski and B. L. Scott. *Ann. Phys.*, **11**:65, (1960).

[21] B. D. Day. *Rev. Mod. Phys.*, 50:495, (1978).

[22] F. Coester, S. Cohen, B. Day, and C. M. Vincent. *Phys. Rev. C*, **1**:769, (1970).

[23] F. Coester, B. Day, and A. Goodman. *Phys. Rev. C*, **5**:1135, (1972).

[24] B. D. Day. *Phys. Rev. Lett.*, **47**:226, (1981).

[25] Z. H. Li *et al. Phys. Rev. C*, **74**:047304, (2006).

[26] H. Primakoff and T. Holstein. *Phys. Rev.*, **55**:1218, (1939).

[27] B. S. Pudliner, V. R. Pandharipande, J. Carlson, and R. B. Wiringa. *Phys. Rev. Lett*, **74**:4396, (1995).

[28] M. Baldo and L. S. Ferreira. *Phys. Rev. C*, **59**:682, (1999).

[29] S. A. Coon *et al. Nucl. Phys.*, **A317**:242, (1979).

[30] P. Grangé, A. Lejeune, M. Martzolff, and J.-F. Mathiot. *Phys. Rev. C*, **40**:1040, (1989).

[31] P. Navrátil and W. E. Ormand. *Phys. Rev. Lett.*, **88**:152502, (2002).

[32] J. J. Aubert *et al. Phys. Lett.*, **B123**:275, (1983).

[33] S. Strauch *et al. Phys. Rev. Lett.*, **91**:052301, (2003).

[34] C. B. Dover, J. Hüfner, and R. H. Lemmer. *Ann. Phys.*, **66**:248, (1971).

[35] F. Klingl, N. Kaiser, and W. Weise. *Nucl. Phys.*, **A624**:527, (1997).

[36] M. Post, S. Leupold, and U. Mosel. *Nucl. Phys.*, **A689**:753, (2001).

[37] P. Muehlich, V. Shklyar, S. Leupold, U. Mosel, and M. Post. *Nucl. Phys.*, **A780**:187, (2006).

[38] T. Hatsuda and S. H. Lee. *Phys. Rev. C*, **46**:R34, (1992).

[39] M. Harada and K. Yamawaki. *Phys. Rept.*, **381**:1, (2003).

[40] S. Klimt, M. Lutz, and W. Weise. *Phys. Lett.*, **B249**:386, (1990).

[41] M. Lutz, S. Klimt, and W. Weise. *Nucl. Phys.*, **A 542**:521, (1992).

[42] E. G. Drnkarev and E. M. Levin. *Nucl. Phys*, **A 511**:679, (1990).

[43] E. G. Drnkarev and E. M. Levin. *Nucl. Phys*, **A516**:715, (1990).

[44] T. D. Cohen, R. J. Furnstahl, and D. K. Griegel. *Phys. Rev. Lett.*, **67**: 961, (1991).

[45] G. E. Brown and M. Rho. *Phys. Rev. Lett.*, **66**:2720, (1991).

[46] V. Koch and G. E. Brown. *Nucl. Phys.*, **A560**:345, (1993).

[47] J. P. Wessels *et al. Nucl. Phys.*, **715**:262, (2003).

[48] R. Arnaldi *et al. Phys. Rev. Lett.*, **96**:162302, (2006).

[49] R. Rapp and J. Wambach. *Adv. Nucl. Phys.*, **25**:1, (2000).

[50] G. Q. Li, C. M. Ko, and G. E. Brown. *Phys. Rev. Lett.*, **75**:4007, (1995).

[51] H. Geissel *et al. Phys. Rev. Lett.*, **88**:122301, (2002).

[52] J. G. Messchendorp *et al. Phys. Rev. Lett.*, **89**:222302, (2002).

[53] D. Trnka *et al. Phys. Rev. Lett.*, **94**:192303, (2005).

[54] M. Naruki *et al. Phys. Rev. Lett.*, **96**:092301, (2006).

[55] R. Nasseripour *et al. Phys. Rev. Lett.*, 99:262302, (2007).

[56] G. E. Brown and M. Rho. *Phys. Rept.*, **396**:1, (2004).

[57] J. D. Holt, T. T. S. Kuo, G. E. Brown, and S. K. Bogner. *Nucl. Phys.*, **A733**:153, (2004).

[58] S. K. Bogner, T. T. S. Kuo, A. Schwenk, D. R. Entem, and R. Machleidt. *Phys. Lett.*, **B576**:265, (2003).

[59] A. Kallio and K. Kolltveit. *Nucl. Phys.*, **53**:87, (1964).

[60] A. Kallio. *Phys. Lett.*, **18**:51, (1965).

[61] H. A. Bethe. *Phys. Rev.*, **103**:1353, (1956).

[62] T. T. S. Kuo and G. E. Brown. *Nucl. Phys.*, **85**:40, (1966).

[63] H. A. Bethe, B. H. Brandow, and A. G. Petschek. *Phys. Rev.*, **129**:225, (1963).

[64] G. E. Brown. *Unified Theory of Nuclear Models and Forces*. North-Holland, Amsterdam, (1971).

[65] J. D. Holt, J. W. Holt, T. T. S. Kuo, and G. E. Brown. *Phys. Rev. C*, **72**:041304(R), (2005).

[66] S. Babu and G. E. Brown. *Ann. Phys.*, **78**:1, (1973).

[67] H. A. Bethe. *Ann. Rev. Nucl. Sci.*, **21**:93, (1971).

[68] R. Machleidt. *Adv. Nucl. Phys.*, **19**:189, (1989).

[69] J. W. Holt and G. E. Brown. *in Hans Bethe and His Physics*, chapter Hans Bethe and the nuclear many-body problem, page 201. World Scientific, Singapore, (2006).

[70] V. R. Pandharipande. *Nucl. Phys.*, **A174**:641, (1971).

[71] V. R. Pandharipande. *Nucl. Phys.*, **A178**:123, (1971).

[72] S. K. Bogner, T. T. S. Kuo, and L. Coraggio. *Nucl. Phys.*, **A684**:432, (2001).

[73] L. Coraggio, A. Covello, A. Gargano, N. Itako, T. T. S. Kuo, D.R. Entem, and R. Machleidt. *Phys. Rev. C*, **66**:021303(R), (2002).

[74] A. Schwenk, G. E. Brown, and B. Friman. *Nucl. Phys.*, **A703**:745, (2002).

[75] J. D. Holt, T. T. S. Kuo, and G. E. Brown. *Phys. Rev. C*, **69**:034329, (2004).

[76] H. Q. Song, S. D. Yang, and T. T. S. Kuo. *Nucl. Phys.*, **A462**:491, (1987).

[77] L. Coraggio, A. Covello, A. Gargano, N. Itako, and T. T. S. Kuo. *Prog. Part. Nucl. Phys.*, to be published, (2008).

[78] J. Kuckei, F. Montani, H. Muether, and A. Sedrakian. *Nucl. Phys.*, **A723**:32, (2003).

[79] S. K. Bogner, A. Schwenk, R. J. Furnstahl, and A. Nogga. *Nucl. Phys.*, **A763**:59, (2005).

[80] J. W. Holt, G. E. Brown, J. D. Holt, and T. T. S. Kuo. *Nucl. Phys.*, **A785**:322, (2007).

[81] L.-W. Siu, T. T. S. Kuo, and R. Machleidt. *Phys. Rev. C*, **77**:034001, (2008).

[82] L.-W. Siu, J. W. Holt, T. T. S. Kuo, and G. E. Brown. in preparation.

[83] K. Suzuki and S. Y. Lee. *Prog. Theor. Phys.*, **64**:2091, (1980).

[84] R. Rapp, R. Machleidt, J. W. Durso, and G. E. Brown. *Phys. Rev. Lett.*, **82**:1827, (1999).

[85] D. H. Youngblood, H. L. Clark, and Y.-W. Lui. *Phys. Rev. Lett.*, **82**: 691, (1999).

[86] A. W. Steiner, M. Prakash, J. M. Lattimer, and P. J. Ellis. *Phys. Rept.*, **411**:325, (2005).

[87] M. Prakash. *Lecture Notes of the workshop on the Nuclear Equation of State*. Puri, India, (1994).

[88] P. Danielewicz. *Nucl. Phys.*, **A727**:233, (2003).

[89] G. E. Brown, C.-H. Lee, and M. Rho. *Phys. Rept.*, 462:1, (2008).

[90] L. D. Landau. *Sov. Phys. JETP*, **3**:920, (1957).

[91] L. D. Landau. *Sov. Phys. JETP*, **5**:101, (1957).

[92] L. D. Landau. *Sov. Phys. JETP*, **8**:70, (1959).

[93] A. B. Migdal and A. I. Larkin. *Sov. Phys. JETP*, **18**:717, (1964).

[94] A. B. Migdal. *Theory of Finite Fermi Systems and Applications to Atomic Nuclei*. Interscience, New York, (1967).

[95] S. O. Bäckman. *Nucl. Phys.*, **A120**:593, (1968).

[96] S. O. Bäckman. *Nucl. Phys.*, **A130**:481, (1969).

[97] G. E. Brown. *Rev. Mod. Phys.*, **43**:1, (1971).

[98] R. S. Poggioli and A. D. Jackson. *Nucl. Phys.*, **A165**:582, (1971).

[99] A. Schwenk, B. Friman, and G. E. Brown. *Nucl. Phys.*, **A713**:191, (2003).

[100] A. Schwenk and B. Friman. *Phys. Rev. Lett.*, **92**:082501, (2004).

[101] J. Kuckei, F. Montani, H. Müther, and A. Sedrakian. *Nucl. Phys.*, **A723**: 32, (2003).

[102] O. Sjöberg. *Ann. Phys.*, **78**:39, (1973).

[103] O. Sjöberg. *Nucl. Phys.*, **A209**:363, (1973).

[104] W. H. Dickhoff, A. Faessler, H. Müther, and S. S. Wu. *Nucl. Phys.*, **A405**:534, (1983).

[105] S. O. Bäckman, G. E. Brown, and J. A. Niskanen. *Phys. Rept.*, **124**:1, (1985).

[106] K. S. Bedell and T. L. Ainsworth. *Phys. Lett.*, **A102**:49, (1984).

[107] I. Ya. Pomeranchuk. *Zh. Eksperim. Teor. Fiz.*, **35**:524, (1958).

[108] A. A. Abrikosov, L. P. Gorkov, and I. E. Dzyaloshinki. *Methods of Quantum Field Theory in Statistical Physics*. Dover, New York, (1963).

[109] F. Nozieres. *Theory of Interacting Fermi Systems*. Addison-Wesley, Reading, Massachusetts, (1964).

[110] B. L. Friman and A. K. Dar. *Phys. Lett. B*, **85**:1, (1979).

[111] G. E. Brown. *Many-Body Problems*. North-Holland, Amsterdam, (1972).

[112] V. Pandharipande, I. Sick, and P. de Witt Huberts. *Rev. Mod. Phys.*, **69**:981, (1997).

[113] P. Möller, J. R. Nix, W. D. Myers, and W. J. Swiatecki. *Atom. Data and Nucl. Data Tabl.*, **59**:185, (1995).

[114] R. Nolte, A. Baumann, K. W. Rose, and M. Schumacher. *Phys. Lett. B*, **173**:388, (1986).

[115] G. E. Brown and M. Rho. *Phys. Rept.*, **269**:333, (1996).

[116] M. Harada, Y. Kim, and M. Rho. *Phys. Rev. D*, **66**:016003, (2002).

[117] B. Friman and M. Rho. *Nucl. Phys.*, **A606**:303, (1996).

[118] C. Song, G. E. Brown, D.-P. Min, and M. Rho. *Phys. Rev. C*, **56**:2244, (1997).

[119] C. Song. *Phys. Rept.*, **347**:289, (2001).

[120] G. F. Bertsch. *Nucl. Phys.*, **74**:234, (1965).

[121] A. P. Zuker. *Phys. Rev. Lett.*, **90**:042502, (2003).

[122] B. R. Barrett and M. W. Kirson. *Nucl. Phys.*, **A148**:145, (1970).

[123] M. Hjorth-Jensen, T. T. S. Kuo, and E. Osnes. *Phys. Rep.*, **261**:126, (1995) and references therein.

[124] M. W. Kirson. *Ann. Phys.*, **66**:624, (1971).

[125] M. W. Kirson. *Ann. Phys.*, **68**:556, (1971).

[126] A. Jackson, A. Lande, and R. A. Smith. *Phys. Rep.*, **86**:55, (1982).

[127] A. Lande and R. A. Smith. *Phys. Rev. A*, **45**:913, (1992).

[128] D. J. Dean and M. Hjorth-Jensen. *Phys. Rev. C*, **69**:054320, (2004).

[129] D. W. L. Sprung and A. M. Jopko. *Can. J. Phys.*, **50**:2768, (1972).

[130] T. T. S. Kuo, S. K. Bogner, and L. Coraggio. *Nucl. Phys.*, **A704**:107c, (2002).

[131] L. Coraggio, A. Covello, A. Gargano, N. Itaco, and T. T. S. Kuo. *Phys. Rev. C*, **66**:064311, (2002).

[132] E. M. Krenciglowa, C. L. Kung, T. T. S. Kuo, and E. Osnes. *Ann. Phys.*, **101**:154, (1976).

[133] J. W. Holt and G. E. Brown. nucl-th/0408047.

[134] T. T. S. Kuo, J. Shurpin, K. C. Tam, E. Osnes, and P. J. Ellis. *Ann. Phys.*, **132**:237, (1981).

[135] P. J. Ellis and E. Osnes. *Rev. Mod. Phys.*, **49**:777, (1977).

[136] J. P. Vary, P. U. Sauer, and C. W. Wong. *Phys. Rev. C*, **7**:1776, (1973).

[137] B. Goulard, B. Lorazo, H. Primakoff, and J. D. Vergados. *Phys. Rev. C*, **16**:1999, (1977).

[138] R. L. Huffman, J. Dubach, R. S. Hicks, and M. A. Plum. *Phys. Rev. C*, **35**:1, (1987).

[139] Y. Jin, L. E. Wright, C. Bennhold, and D. S. Onley. *Phys. Rev. C*, **38**: 923, (1988).

[140] A. García and B. A. Brown. *Phys. Rev. C*, **52**:3416, (1995).

[141] I. S. Towner and J. C. Hardy. *Phys. Rev. C*, **72**:055501, (2005).

[142] F. Ajzenberg-Selove, J. H. Kelley, and C. D. Nesaraja. *Nucl. Phys.*, **A523**:1, (1991).

[143] R. Sherr, J. B. Gerharat, H. Horie, and W. F. Hornyak. *Phys. Rev.*, **100**:945, (1955).

[144] P. Navrátil, J. P. Vary, and B. R. Barret. *Phys. Rev. Lett.*, **84**:5728, (2000).

[145] S. C. Pieper and R. B. Wiringa. *Ann. Rev. Nucl. Part. Sci.*, **51**:53, (2001).

[146] G. E. Brown, W. Weise, G. Baym, and J. Speth. *Comm. Nucl. Part. Phys.*, **17**:527, (1997).

[147] V. Bernard, U.-G. Meissner, and I. Zahed. *Phys. Rev. Lett.*, **59**:966, (1987).

[148] S. Klimt, M. Lutz, and W. Weise. *Phys. Lett.*, **B249**:386, (1990).

[149] L. Zamick, D. C. Zheng, and M. S. Fayache. *Phys. Rev. C*, **51**:1253, (1995).

[150] M. S. Fayache, L. Zamick, and B. Castel. *Phys. Rept.*, **290**:201, (1997).

[151] D. R. Inglis. *Rev. Mod. Phys.*, **25**:390, (1953).

[152] B. Jancovici and I. Talmi. *Phys. Rev.*, **95**:289, (1954).

[153] M. S. Fayache, L. Zamick, and H. Müther. *Phys. Rev. C*, 60:067305, (1999).

[154] H.-C. Kim, J. W. Durso, and K. Holinde. *Phys. Rev. C*, **49**:2355, (1994).

[155] S. K. Bogner, T. T. S. Kuo, and A. Schwenk. *Phys. Rep.*, **386**:1, (2003).

[156] L. Coraggio *et al. Phys. Rev. C*, **75**:057303, (2007).

[157] L. Zamick. *Phys. Lett.*, **21**:194, (1966).

[158] A. Negret et al. *Phys. Rev. Lett.*, **97**:062502, (2006).

[159] S. S. M. Wong. *Introductory Nuclear Physics*. (Wiley, New York), 1998.

[160] L. A. Schaller, L. Schellenberg, A. Ruetschi, and H. Schneuwly. *Nucl. Phys.*, **A343**:333, (1980).

[161] W. Schütz. *Z. Phys.*, **A273**:69, (1975).

[162] M. Rho. *Prog. Theor. Phys. Suppl.*, **168**:519, (2007).

[163] M. Harada, T. Kugo, and K. Yamawaki. *Phys. Rev. Lett.*, **71**:1299, (1993).

[164] G. E. Brown, L. Grandchamp, C.-H. Lee, and M. Rho. *Phys. Rept.*, **391**: 353, (2004).

[165] G. E. Brown and M. Rho. nucl-th/0509001, .

[166] G. E. Brown and M. Rho. nucl-th/0509002, .

[167] D. E. Miller. *Phys. Rept.*, **443**:55, (2007).

[168] G. E. Brown, J. W. Holt, C-H. Lee, and M. Rho. *Phys. Rept.*, **439**:161, (2006).

[169] M. Rho. arXiv:0711.3895.

[170] A. Ohnishi, N. Kawamoto, and K. Miura. arXiv:0803.0255.

[171] M. Dey, V. L. Eletsky, and B. L. Ioffe. *Phys. Lett.*, **B252**:620, (1990).

[172] K. Suzuki *et al. Phys. Rev. Lett.*, **92**:072302, (2004).

[173] G. E. Brown and M. Rho. *Phys. Rept.*, **398**:301, (2004).

[174] J. D. Walecka. *Ann. Phys. (N.Y.)*, **83**:491, (1974).

[175] V. Bernard, U.-G. Meissner, and I. Zahed. *Phys. Rev. D*, **36**:819, (1987).

[176] M. Harada, Y. Kim, and M. Rho. *Phys. Rev. D*, **66**:016003, (2002).

[177] B. W. Lynn. *Nucl. Phys.*, **B402**:281, (1993).

[178] R. Shankar. *Rev. Mod. Phys.*, **66**:129, (1994).

[179] T. Matsui. *Nucl. Phys.*, **A370**:365, (1981).

[180] G. Gelmini and B. Ritzi. *Phys. Lett.*, **B357**:431, (1995).

[181] T.-S. Park, D.-P. Min, and M. Rho. *Nucl. Phys.*, **A596**:515, (1996).

[182] G. E. Brown and M. Rho. *Nucl. Phys.*, **A506**:503, (1996).

[183] M. Rho. *Yad. Fiz.*, **64**:696, (2001).

[184] P. Kienle and T. Yamazaki. *Prog. Part. Nucl. Phys.*, **52**:85, (2004).

[185] R. J. Furnstahl and B. Serot. *Nucl. Phys.*, **A671**:447, (2000).

[186] C. Song, D.-P. Min, and M. Rho. *Phys. Lett.*, **B424**:226, (1998).

[187] M. A. Nowak, M. Rho, and I. Zahed. *Chiral Nuclear Dynamics*. (World Scientific, Singapore), (1996).